

Photoelectronic effects in self-assembled vertically aligned nanocomposite oxide thin films

Dissertation

zur Erlangung des Doktorgrades der Naturwissenschaften (Dr. rer. nat.)

der

Naturwissenschaftlichen Fakultät II

Chemie, Physik und Mathematik

der Martin-Luther-Universität Halle-Wittenberg

vorgelegt von

Herrn Lutz Mühlenbein

Erstgutachter:

Prof. Dr. Jörg Schilling

Zweitgutachterin:

Prof. Dr. Kathrin Dörr

Drittgutachter:

Prof. Dr. Josep Fontcuberta Grifó

Datum der öffentlichen Verteidigung: 08.12.2023

Contents

1	Introduction	1
1.1	General introduction and motivation	1
1.2	Outline	3
2	Scientific background	4
2.1	Vertically aligned nanocomposite (VAN) oxide thin films	4
2.1.1	A short history of VANs	4
2.1.2	Functionality of VANs	6
2.1.3	Growth mechanisms and architectures of VANs	10
2.1.4	Current vectors of VAN research	14
2.2	Bulk photovoltaic effect in oxide ferroelectrics	15
2.3	Potentials of bulk photovoltaic effect in VANs	18
3	Experimental methods	19
3.1	Thin film growth	19
3.1.1	Substrate preparation	19
3.1.2	Pulsed laser deposition	20
3.2	X-ray diffraction	22
3.3	Atomic Force Microscopy	23
3.3.1	Conductive Atomic Force Microscopy	25
3.4	Photoelectrical measurements	25
3.4.1	Electrode fabrication	25
3.4.2	Illumination and electrical equipment	27
3.5	Additional characterization	27

4 Part A - BiFeO₃:Sm₂O₃ system	29
4.1 [LM1] Impact of Samarium on the Growth of Epitaxial Bismuth Ferrite Thin Films	29
5 Part B - (Pb, Bi)(Ti, Nb)O₃:NiO system	38
5.1 [LM2] Nanocomposites with Three-Dimensional Architecture and Impact on Photovoltaic Effect	39
5.2 [LM3] Control of Layering in Aurivillius Phase Nanocomposite Thin Films and Influence on Ferromagnetism and Optical Absorption	54
6 Summary and Outlook	65
Bibliography	66
Acknowledgements	74
Curriculum Vitae	77

Chapter 1

Introduction

1.1 General introduction and motivation

Composite materials are combinations of two or more materials or phases in which the constituents remain as separate entities, leading to a system with uniquely combined or emergent properties. They are found in nature as bone, teeth, and shell and are an integral part of human technology as concrete, aeronautic components, or armor [1]. In addition to ubiquitous structural applications, composites are exploited for specific thermal, dielectric, or conductive properties. In many cases, composites are the best possible contenders for a set of, at first glance, mutually opposing challenges: light-weight yet strong; ductile yet stiff; heat resistive yet thin.

Around the turn of the millennium, a similar set of challenges dawned on physics and materials science: ferroelectric yet ferromagnetic. Such a *multiferroic* material could be the foundation for next-generation, energy-efficient memories, actuators, or switches, as it allows one to manipulate magnetic order via electric signals and vice versa. The com-

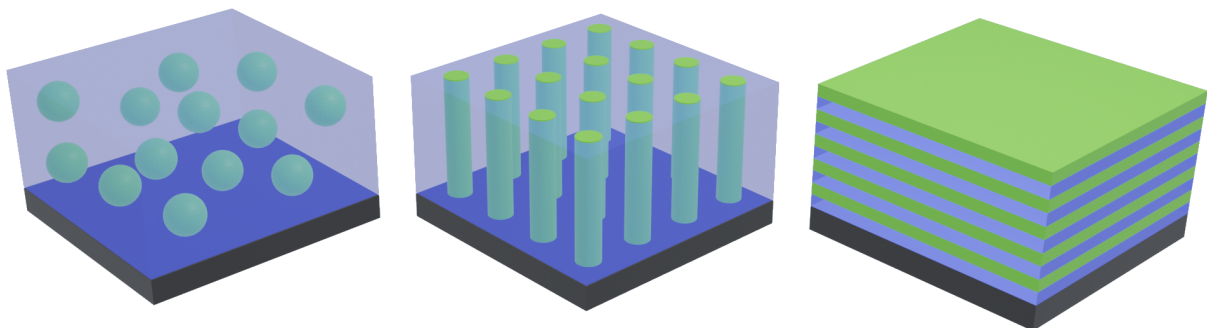


Figure 1.1: Three types of nanocomposite materials: (a) nanoparticle (b) vertically aligned and (c) lamellar horizontal nanocomposite thin film. They are also referred to as 0-3, 1-3, and 2-2 composites, respectively, within the Newnham notation [2]. The vertically aligned structure uniquely exhibits large, tunable heterointerfacial area, accessible from the surface, as well as the possibility of vertical strain control.

bination in a single material is so challenging, as in many compounds, partially filled d orbitals, that are vital for magnetic order, in turn inhibit ferroelectricity [3]. A nanocomposite approach seemed reasonable, thus creating an 'artificial' multiferroic. With this goal in mind, the first deliberately designed Vertically Aligned Nanocomposite (VAN) thin film was synthesized in 2004 *via* pulsed laser deposition (PLD), comprising of spinel ferrimagnetic CoFe_2O_4 nanocolumns, with a diameter of about 25 nm, embedded in a matrix of the ferroelectric perovskite BaTiO_3 [4]. As other material combinations followed, the much larger potential of VANs was soon recognized: Going beyond just combining two features into one material, the VAN structure attracted extensive interest due to the presence of *large heterointerfacial area* within the film, which is easily accessible from the surface, as well as the possibility of *vertical strain control*. Both of these characteristics clearly distinguish VAN from nanoparticle and laminar composites, as illustrated in Fig. 1.1. As of today, VAN model system have been demonstrated for applications for memristors [5], lithium-ion and solid-state batteries [6, 7], solid oxide fuel cells [8, 9], water splitting [10, 11], and thin film energy storage devices [12].

However, research works addressing the interaction of oxide VANs with light are scarce, although in particular the heterointerfacial areas of a VAN are a promising feature for photoelectronic processes and energy harvesting. Coincidentally, ferroelectric oxides, which are some of the building blocks of many known VAN systems, are also widely studied for exhibiting the bulk photovoltaic effect due to their noncentrosymmetric crystal structure. Although fundamental understanding of the bulk photovoltaic effect has greatly improved over the past few years, experimentally demonstrated energy conversion efficiencies remain low as a result of limitations in photocurrent density.

As a VAN structure may be conceived to be effective in overcoming these limitations, this thesis aims to link the two topics and study photoconduction and photovoltaic processes in VANs. After a short introduction, two systems shall be studied: The $\text{BiFeO}_3:\text{Sm}_2\text{O}_3$ system and the $(\text{Pb, Bi})(\text{Ti, Nb})\text{O}_3:\text{NiO}$ system.

A few words on the scope of the present work: First, this thesis focuses mostly on oxide-oxide nanocomposites, in contrast to oxide-metal, oxide-nitride, or other composites. Second, this thesis focuses on self-assembled nanocomposite oxide thin films in contrast to templated nanocomposite growth.¹ Third, this thesis focuses on single-crystalline thin film systems in contrast to polycrystalline or bulk systems.

¹In the context of nanocomposites, it is customary to use the term 'self-assembled', referring to the composite nature (phase separation) emerging spontaneously during thin film synthesis (via physical or chemical vapor deposition or other methods). It should not be confused with the synthesis method 'self-assembly', where a thin film spontaneously forms from a precursor solution.

1.2 Outline

The following chapter will provide an overview of the literature on the topic of self-assembled vertically aligned nanocomposite oxide thin films, as well as a concise introduction to the bulk photovoltaic effect. Chapter 3 presents the experimental methods applied by the author to reach the findings of the present thesis. In chapters 4 and 5, the experimental results of the present thesis will be presented and discussed. As this is a cumulative thesis, the chapters will provide a brief introduction before reprinting the work as published in the respective scientific journal.

Chapter 4 is dedicated to the $\text{BiFeO}_3:\text{Sm}_2\text{O}_3$ system. Here, a nanocomposite with phase-separated ionic species was reported. The present work presents another kind of structural nanocomposite, where the phases are not separated by ionic species but by crystal orientation.

Chapter 5 addresses the material $(\text{PbTiO}_3)_x(\text{BiNi}_{2/3}\text{Nb}_{1/3}\text{O}_3)_{1-x}$, previously only studied in bulk. Spontaneous formation of a novel three-dimensional, 'nanoscaffold' structure during thin film growth is observed. Photovoltaic efficiency is enhanced five times compared to a single-phase PbTiO_3 thin film.

Chapter 6 will summarize the present work and provide an outlook on future research goals.

Chapter 2

Scientific background

2.1 Vertically aligned nanocomposite (VAN) oxide thin films

This chapter aims to provide the reader with an overview of the published research on self-assembled vertically aligned nanocomposite oxide thin films. After a short chronological summary of VAN research since its inception around the turn of the millennium, the next two sections group the literature and identify repeating patterns with respect to, first, functional properties of VANs and, second, to their growth mechanisms and architectures. Finally, a short statement summarizes the current vectors in VAN research.

2.1.1 A short history of VANs

Self-assembled structures similar to VANs in oxide thin films were discovered two decades ago in searches for new materials with improved colossal magnetoresistance [13, 14]. Lebedev, Moshnyaga et al. studied films of the perovskite oxide $\text{La}_{0.7}\text{Ca}_{0.3}\text{MnO}_3$ grown by metalorganic aerosol deposition and found that, when adding MgO to the precursor solution, the Mg ions do not substitute Ca in the perovskite lattice, but rather segregate into a matrix that surrounds grains of $\text{La}_{0.7}\text{Ca}_{0.3}\text{MnO}_3$.

Inspired by this discovery, researchers around Zheng and Ramesh applied the finding to a specific problem: the lack of single-phase materials with large magnetoelectric coupling. They specifically chose a combination of classic perovskite ferroelectrics and magnetostrictive spinel ferrimagnets, $\text{BaTiO}_3\text{:CoFe}_2\text{O}_4$ [4, 15], $\text{PbTiO}_3\text{:CoFe}_2\text{O}_4$ [16, 17], $\text{BiFeO}_3\text{:CoFe}_2\text{O}_4$ [18, 19], $\text{BiFeO}_3\text{:NiFe}_2\text{O}_4$ [20]. In all cases, films were synthesized by pulsed laser deposition on SrTiO_3 substrates. The structure of the $\text{BaTiO}_3\text{:CoFe}_2\text{O}_4$ VAN is detailed in Fig. 2.1.

Beginning in 2008, the research in VANs was further led by MacManus-Driscoll at the

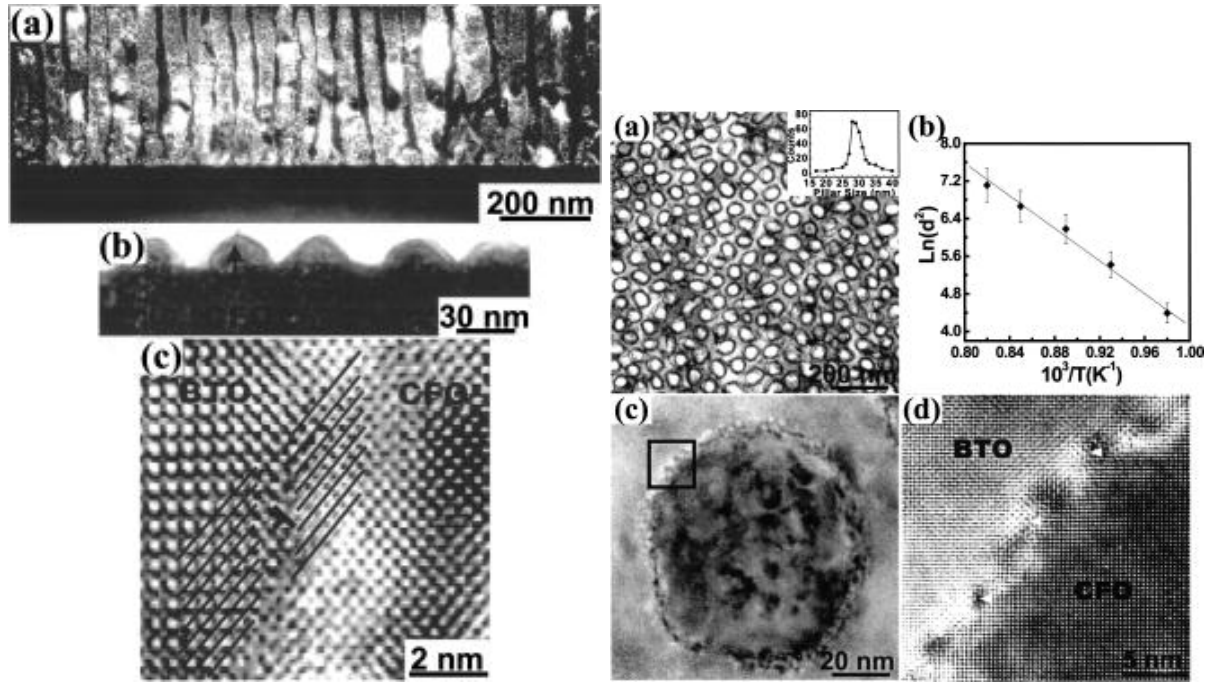


Figure 2.1: Zheng *et al.* present the first deliberately designed VAN thin film system between BaTiO₃ (BTO) and CoFe₂O₄ (CFO) grown on SrTiO₃. Reprinted with permission from [4]. ©2004 AIP Publishing.

Original caption left: (a) Cross-section dark field TEM image taken with [130] of CFO. (b) Cross-section bright field TEM image showing the outgrowth of the CFO nanopillars. (c) Cross-section high resolution TEM image showing dislocations formed at the interface between a CFO pillar and the BTO (BTO) matrix.

Original caption right: (a) Plan view TEM image of the film grown at 920°C with the inset of statistic size distribution of the pillars. (b) Lateral dimension of the CFO nanopillars vs temperature. (c) In-plane high resolution TEM image of one CFO pillar embedded in the BTO matrix grown at 950°C. (d) Magnified segment of the interface between the CFO pillar and the BTO matrix from (c).

University of Cambridge. A central study reported on VAN systems of BiFeO₃:Sm₂O₃ and La_{0.7}Sr_{0.3}MnO₃:ZnO grown by pulsed laser deposition on STO substrates [21]. The achievement of vertical strain control was claimed: Above a critical film thickness, the strain on the matrix induced by the nanocolumns can overpower epitaxial strain from the substrate and even change the strain state of a phase in the composite from compressive to tensile or vice versa. Another example of this was provided in the BaTiO₃:Sm₂O₃ system, where a BaTiO₃ matrix was highly strained by Sm₂O₃ columns [22]. Over the following decade, numerous VAN system were demonstrated, in particular by researchers around MacManus-Driscoll at Cambridge and Wang at Purdue University: La_{0.7}Sr_{0.3}MnO₃ matrices with columnar structures of Mn₃O₄ [23], CeO₂ [24], MgO [25], NiO [26, 27], and CuO [28] - moreover, BaTiO₃:YMnO₃ [29], La₂CoMnO₆:ZnO [30], BaSrTiO₃:Sm₂O₃ [31] and many more variations of the perovskite-spinel and perovskite-rocksalt archetypes [32].

Furthermore, the system La_{0.7}Sr_{0.3}MnO₃:NiO was recently studied in detail by Panchal *et al.* at Helmholtz Institute Berlin [33, 34]. Wang *et al.* [35] recently demonstrated a VAN consisting of isostructural perovskites BaTiO₃ and SrRuO₃.

2.1.2 Functionality of VANs

The initial motivation for the investigation of VANs was mainly driven by three different functional properties: magnetoresistance [13], magnetoelectrics/multiferroics [4, 36], and, to a lesser extent, superconductivity [37]. Since then, the range of proposed applications has expanded and today includes memristors [5], photoelectrochemical water splitting [10, 11], lithium ion batteries [6, 38], solid-state batteries [7], solid oxide fuel cells [8, 9] and superbroadband transparent conductors [39].

The reason for the ubiquity of possible applications lies mainly in two unique features of VANs: Vertical strain control and vertical heterointerfaces. These two features enable tunability of desirable functional properties such as ferromagnetism, ferroelectricity, magnetoelectric coupling, magnetotransport, superconductivity, and vertical interface conduction [12].

Vertical strain control

Vertical strain control enables stabilization of a wide variety of strain states for a given material-substrate combination. Strain in general can have a significant impact on various fundamental and functional properties, such as charge carrier mobility for a semiconductor, Curie temperature and magnitude of polarization for a ferroelectric, or transition temperature for a superconductor [40]. Especially thin films can accommodate extremely large strains and thus can exhibit lattice parameters and functional properties that vastly differ from those of their bulk counterparts. Here, in the past, typically the biaxial lateral strain exerted by the substrate on the thin film has been considered. The VAN structure now additionally introduces strain control along the third spatial dimension, thus allowing for enhanced stabilization of meta-stable states with desirable functional properties.

For instance, BaTiO_3 is a robust ferroelectric material that presents itself as an attractive lead-free (thus environmental-friendly and non-hazardous) alternative to the widely used $\text{Pb}(\text{Zr}, \text{Ti})\text{O}_3$, were it not for its low Curie temperature of 120°C , resulting in a narrow operation temperature range [41]. Choi et al. were successful in enhancing this value by nearly 500°C in thin BaTiO_3 on (110)-oriented DyScO_3 substrates, the relative lattice mismatch exerting a 1.7% lateral biaxial compressive strain on the thin film [42]. However, such a film under lateral strain from the substrate will not remain coherently strained for arbitrary film thicknesses, but will progressively undergo lattice relaxation by forming misfit dislocations at the substrate-film interface, since this is energetically favorable with increments in film thickness [43]. In their work, Choi et al. were able to experimentally verify coherently strained films on DyScO_3 substrates up to 50 nm film thickness. Although this may be thick enough for certain applications such as ferroelectric random access memories [42], it is not sufficient for energy harvesters or transducers [22].

Harrington et al. demonstrated vertical strain control with a VAN to solve this problem, realizing high tensile vertical strain on a BaTiO₃ matrix exerted by Sm₂O₃ nanocolumns, within a 1 μm thick film on SrTiO₃ substrates with a phase ratio of 1:1 between BaTiO₃ and Sm₂O₃. [22]. It was experimentally proven that the Curie temperature was increased to at least 330 °C.

Whereas in classical lateral epitaxial strain control, a substrate of macroscopic dimensions is assumed to remain structurally unchanged because its volume is practically infinite in comparison to the thin film, the individual volumes of constituent phases of a VAN are in some cases comparable in magnitude. Therefore, in addition to the vertical lattice constants and epitaxial relation, the elastic moduli of the two phases have to be considered to determine the respective vertical strain state. Broadly speaking, in the BaTiO₃:Sm₂O₃ VAN discussed above, predominantly the BaTiO₃ is strained by the Sm₂O₃ columns, whereas in the previously studied BaTiO₃:CoFe₂O₄ VAN, predominantly the CoFe₂O₄ nanocolumns are strained by the BaTiO₃. To be more precise, the phases exert strain on each other, resulting in a more pronounced lattice contraction or expansion in the less stiff phase ($Y_{\text{Sm}_2\text{O}_3} > Y_{\text{BaTiO}_3} > Y_{\text{CoFe}_2\text{O}_4}$ for the Young's moduli of the constituent phases for these examples). The energy of the elastic interaction E_e can be expressed as [4]:

$$E_e = \frac{\alpha(1-\alpha)Y_1Y_2\Delta\epsilon_{\perp}}{2((1-\alpha)Y_1 + \alpha Y_2)} \quad (2.1)$$

where $\Delta\epsilon_{\perp}$ is the relative vertical misfit strain and $(\alpha, 1-\alpha)$ the respective fractions of the two phases with Young's moduli Y_1 and Y_2 .

Another important aspect to consider is the competition and interplay between vertical strain control (at nanocolumns) and lateral strain control (at the substrate-film interface) in one and the same thin film system. Here, the dominance of either strain control mode is determined by the ratio of heterointerfacial area between phases 1 and 2 and the substrate-to-film interface. This ratio in turn depends on the thickness of the film, the phase fractions, and the average diameters of the embedded nanostructures. For example, MacManus-Driscoll et al. demonstrated how the out-of-plane strain state of Sm₂O₃ was transformed from a compressive -1.0% for a 50 nm thick pure Sm₂O₃ film to a tensile 0.6% for a 50 nm thick BiFeO₃:Sm₂O₃ VAN film on a substrate SrTiO₃ with a phase ratio of 1:1 (strain values calculated with respect to bulk Sm₂O₃) [21]. When the thickness of the film was reduced to 20 nm, the compressive strain was reduced to 0.1% , and when the thickness of the film increased to 150 nm, the compressive strain increased to 1.5% . While the pure film is completely under lateral strain control, for the 20 nm VAN, the lateral and vertical strains almost cancel each other out. With increasing thickness, vertical strain control increasingly dominates. In theory (assuming no misfit dislocations at vertical interfaces that would reduce vertical strain coupling), vertical strain control dominates if $t > a$, [21], where t is the film thickness and a the average width of a nanocolumn. In

relation to this, it was shown in the same system that, for a decrease in average column width, vertical deformation control increases [44]. In the $\text{BiFeO}_3\text{:Sm}_2\text{O}_3$ VAN, the smaller column width (higher vertical strain control) resulted in a reduction in dielectric loss [44].

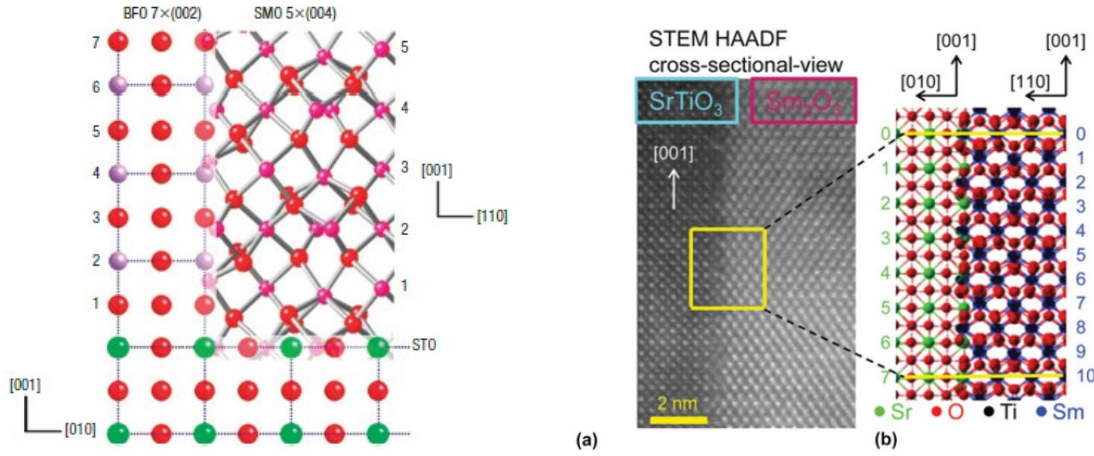


Figure 2.2: *Left*: Vertical epitaxy in the perovskite-spinel $\text{BiFeO}_3\text{:Sm}_2\text{O}_3$ system on SrTiO_3 substrate, demonstrating the 7:5 registry of horizontal lattice planes. Reprinted with permission from [21]. ©2008 Springer Nature. *Right*: The $\text{SrTiO}_3\text{:Sm}_2\text{O}_3$ vertical heterointerface as imaged by transmission electron microscopy (a) and schematic view (b). Reprinted from [5] under the Creative Commons license.

Lastly, note that, because most VANs consist of two phases with different crystal structures (e.g., perovskite-spinel in most of the examples mentioned so far), the vertical epitaxial relationship is often more complicated than in in-plane epitaxy, where typically a substrate of the same crystal structure or at least with effectively equivalent surface structure is selected. For example, Fig. 2.2 (left) shows the case of vertical epitaxy in the $\text{BiFeO}_3\text{:Sm}_2\text{O}_3$ VAN on SrTiO_3 , where a 7:5 ratio of horizontal lattice planes was determined, resulting in effective domain widths of 1.327 nm and 1.360 nm, respectively, from which the relative vertical misfit strain can be calculated.

Beyond just stabilizing a certain strain state throughout large thicknesses, vertical strain control has been used to continuously tune various functional properties such as ferroelectricity, magnetoresistance, magnetic anisotropy, and superconductivity. A recent review summarizes these efforts [45].

Vertical heterointerfaces

The discovery of a highly mobile two-dimensional electron gas (2DEG) at the interface of the two wide-gap insulating perovskite oxides LaAlO_3 and SrTiO_3 [46], has attracted a great deal of attention and sparked research into the emergent properties of oxide heterointerfaces [47, 48]. In addition to its high carrier mobility, the 2DEG was shown to exhibit a magnetic moment, although neither of the constituents is magnetic [49],

and to become superconducting at low temperatures [50]. As in the $\text{LaAlO}_3/\text{SrTiO}_3$ case, oftentimes the interfaces exhibit widely different properties than the bulk constituents due to two-dimensionality and quantum confinement [51]. Other examples include pronounced interfacial metal-insulator transition in LaNiO_3 on SrTiO_3 [52], interfacial ferromagnetism in $\text{LaNiO}_3/\text{CaMnO}_3$ [53], and built-in potential at the polar/non-polar $\text{LaCrO}_3/\text{SrTiO}_3$ interface [54]. Leaving aside the simple coupling of the order parameters of the two phases, the interface becomes a phase of its own with unique properties and can eventually dominate the overall behavior of the system; to paraphrase Herbert Kroemer, the interface becomes the device [55].

However, with regard to certain applications, an in-plane heterointerface between a film and its (virtual) substrate has two obvious drawbacks: First, the interface is not readily accessible from the top surface, as it is mostly buried; second, the interface-to-volume ratio is typically low (if not dealing with two ultrathin films, which poses other challenges). Both of these issues can be addressed by a VAN structure that introduces vertical heterointerfaces. By design, these interfaces are accessible from the surface and their density, and thus the heterointerfacial area, can be tuned. In cases where the behavior of the interface itself is not of interest and the focus is shifted to the coupling between the two phases, such as for purpose-designed VAN multiferroics such as $\text{BaTiO}_3:\text{CoFe}_2\text{O}_4$ and related compounds, the vertical composite can be considered superior to the horizontal laminar composite, as it is not as tightly clamped by the substrate and the heterointerfacial area is larger [56]. A recent review by Gao et al. summarizes the history and advances in magnetoelectric coupling in VANs [57].

Hsieh et al. first identified high local conductivity at the vertical interfaces of the $\text{BiFeO}_3:\text{CoFe}_2\text{O}_4$ VAN, which can be modulated by an external electric field [58, 59], resulting in memristive behavior (non-volatile switchable resistance). This result, as proven by conductive atomic force microscopy, can be seen in Figure 2.3. The conductive property of the interface and its modulation could be attributed to the accumulation and movement of oxygen vacancies at the interface [58, 60]. A similar memristive behavior originating from oxygen vacancies was found at the interfaces of VANs $\text{SrTiO}_3:\text{Sm}_2\text{O}_3$, $\text{BaTiO}_3:\text{Sm}_2\text{O}_3$ and $\text{Ba}_{0.6}\text{Sr}_{0.4}\text{TiO}_3:\text{Sm}_2\text{O}_3$, as shown in Fig. 2.2 (right) [5]. The high concentration of oxygen vacancies was attributed to the structural incompatibility of the VAN constituent phases at the vertical interfaces due to the different space groups [5, 60]. The memristive behavior can then be explained by migration of the vacancies [5, 61].

In both $\text{BiFeO}_3:\text{Sm}_2\text{O}_3$ and the $\text{BaTiO}_3:\text{Sm}_2\text{O}_3$, the VAN structure results in a lower overall leakage current [23, 62]. In the $\text{BaTiO}_3:\text{Sm}_2\text{O}_3$ system, the VAN structure was additionally proven to result in dielectric relaxation [63]. Both phenomena can again be attributed to heterointerfaces acting as sinks for oxygen vacancies that would otherwise be distributed throughout the ferroelectric phase, enhancing the dielectric loss.

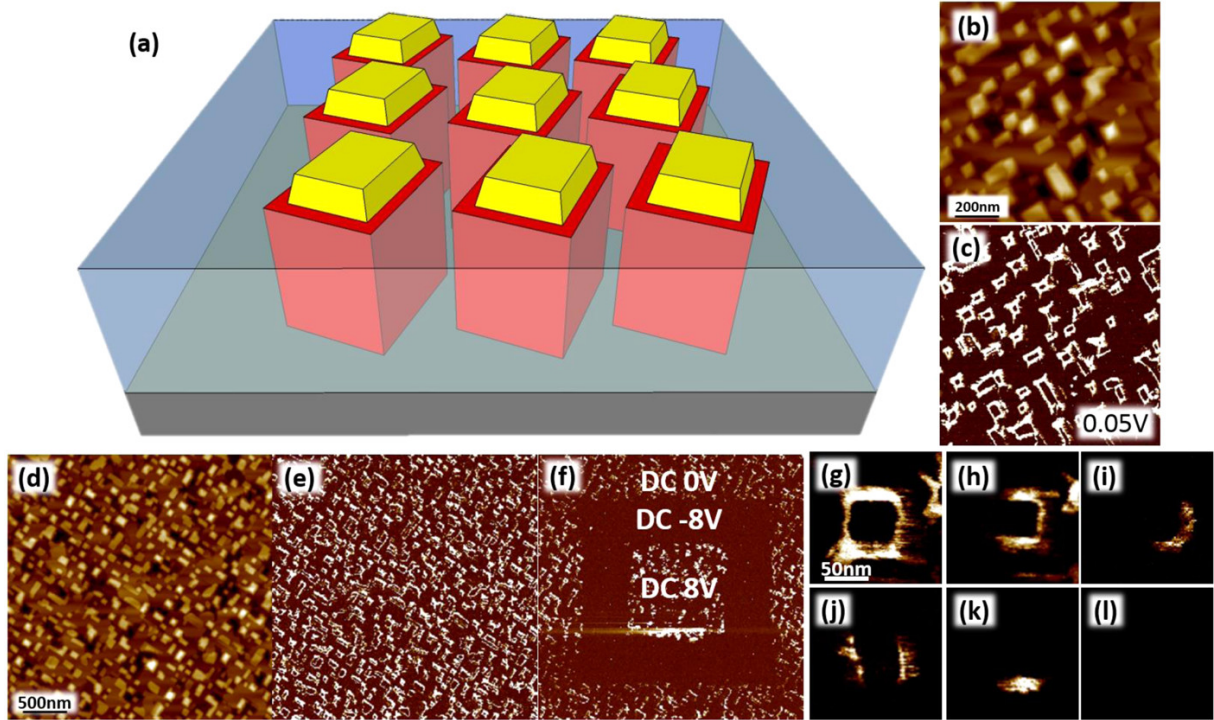


Figure 2.3: Hsieh *et. al.* here prove enhanced conductivity at the heterointerfaces of a BiFeO_3 (BFO)- CoFe_2O_4 (CFO) VAN by conductive atomic force microscopy (see section 3.3). Reprinted with permission from [58]. ©2013 American Chemical Society. *Original caption:* (a) Diagram of BFO–CFO nanostructures. CFO nanopillars (yellow) are embedded in the BFO matrix (blue), and hence tubular interfaces (red) form between these two materials. (b) Topography and (c) current image of BCFO are gained simultaneously under the C-AFM mode, where the current is read by applied -0.05 V tip bias. (d-f) Conduction currents at tubular interfaces can be turned on and off by applying a larger DC bias (8 V) of different polarity. (g-l) Currents at four sides of the tubular interface can be switched individually.

Other interface-induced phenomena are magnetic effects due to unmatched spins at the vertical heterointerfaces. For example, perpendicular exchange bias was detected in $\text{La}_{0.7}\text{Sr}_{0.3}\text{MnO}_3:\text{NiO}$ thin films, where the uncompensated surface moments of NiO, an antiferromagnet in bulk, are pinned at the heterointerfaces. The temperature dependence of the magnetic properties shows a spin-glass behavior with frozen-in and rotatable spins at the interface, as shown in Fig. 2.4.

2.1.3 Growth mechanisms and architectures of VANs

VANs can be grouped into different architectures with respect to the specific shape of vertically oriented nanostructures, as shown in Fig. 2.5: Circular nanocolumns [22], rectangular/square nanocolumns [20], nanocheckerboard structure [21], and nanomaze configurations [64].

The architecture is determined by minimizing the total free energy of the system, including both phases of the composite and the substrate. The free energy is composed of the elastic energy, as in Eq. 2.1, and the interfacial energy. [65]. Several of the experimentally

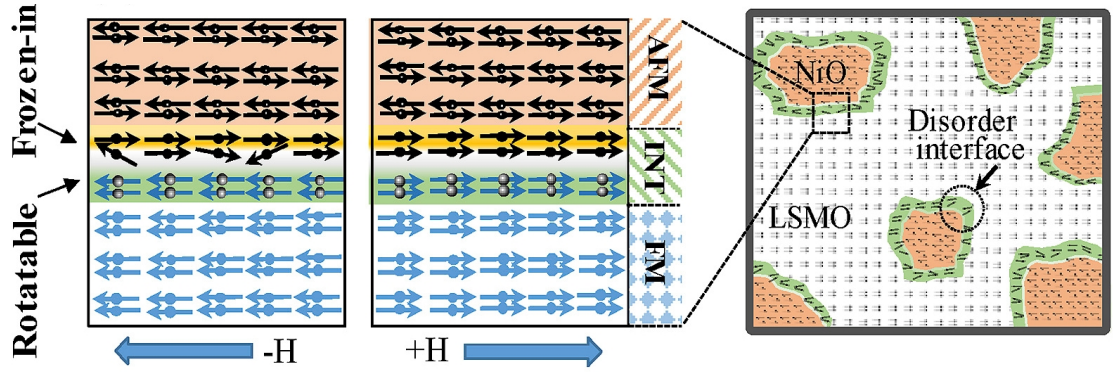


Figure 2.4: Spin glass-like behavior at the interface (INT) of ferromagnetic (FM) $\text{La}_{0.7}\text{Sr}_{0.3}\text{MnO}_3$ and antiferromagnetic (AFM) NiO. (Top view). Reprinted with permission from [33]. ©2019 Elsevier.

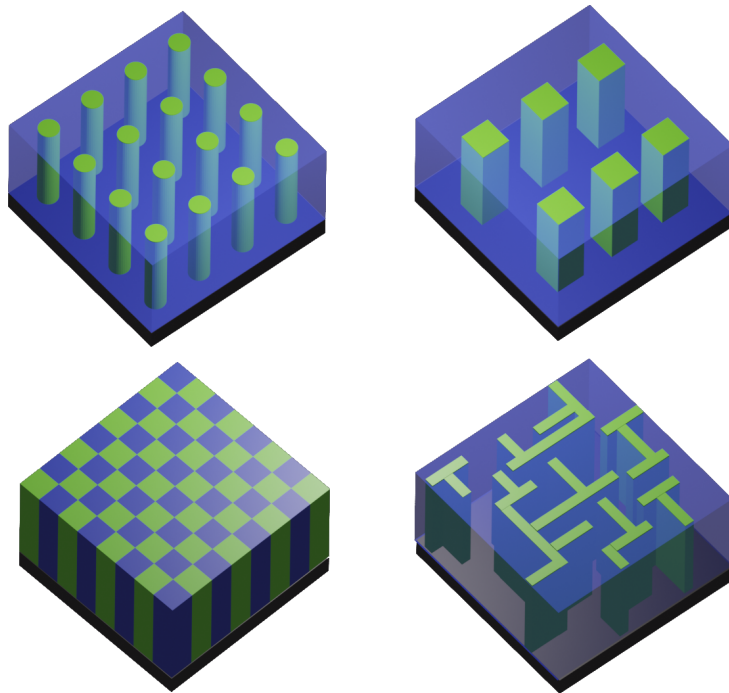


Figure 2.5: Schematic representation of different VAN architectures: (a) Circular nanocolumns, (b) rectangular/square nanocolumns, (c) nano-checkerboard and (d) nano-maze configurations

observed architectures can be predicted by a phase field model of this free energy approach [66].

Most VANs, such as the perovskite-spinel or perovskite-rocksalt systems, are comprised of constituents with no or very limited miscibility. In this case, spontaneous phase separation occurs by nucleation and growth [67]. As portrayed in Fig. 2.6, immediately within formation of the first few atomic layers that form at the substrate, the atomic species undergo segregation. Generally, the phase with higher wetting ability (lower interfacial energy with the substrate) assumes the role of the matrix, and the phase with lower wetting ability assumes the role of the epiphyte (e.g. nanocolumns). This has been demonstrated by analysis of reflective high-energy electron diffraction (RHEED) patterns

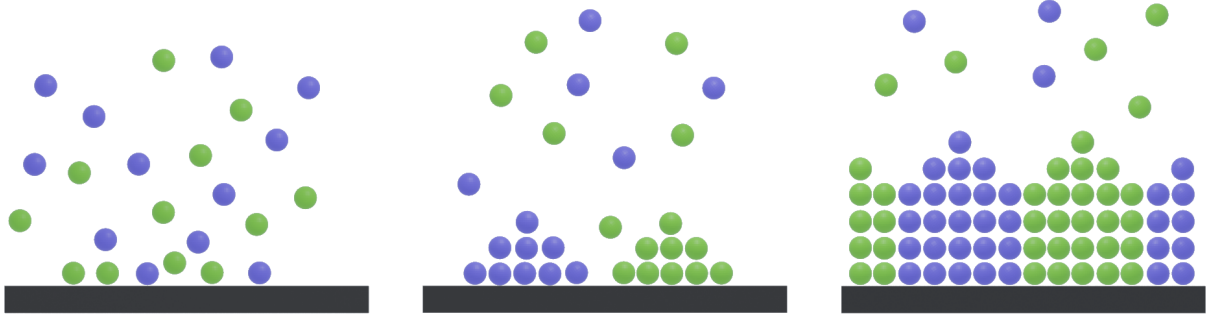


Figure 2.6: Schematic representation of a VAN formation by nucleation-and-growth during thin film deposition - The substrate is at the bottom and the to-be-deposited atomic species arrive from the top; from left to right, time increases.

during growth of $\text{BiFeO}_3:\text{CoFe}_2\text{O}_4$ VAN thin films on SrTiO_3 [68, 69]. In addition to the difference in the interaction with the substrate, the elastic interaction between the phases is also reported to be critical in determining the resulting nanostructure, with the softer phase tending to form the matrix and the stiffer phase forming the nanocolumns [70]. Within one architecture, external growth conditions can be used to fine-tune the nanos-

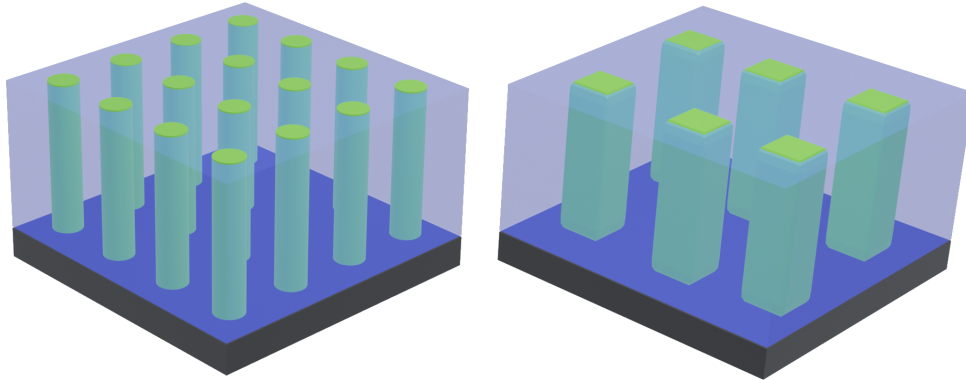


Figure 2.7: *Left*: A low substrate temperature tends to result in small, circular pillars. The resulting large interfacial area leads to a high level of vertical strain control. *Right*: A high substrate temperature tends to result in large, squarish pillars. The resulting small interfacial area leads to a low level of vertical strain control [65].

tructure of the VANs with respect to certain size parameters, such as the mean column diameter in nanocolumnar architectures. Especially the substrate temperature is reported to be decisive [65] (see Fig. 2.7). For the initial deposition stages, the nanocolumns can be modeled as nuclei of critical diameter [71]:

$$d_{\text{crit}} = \frac{4\gamma_{12}T_m}{\Delta H_{\text{het}}(T_m - T_s)} = \frac{4\gamma_{12}}{\Delta H_{\text{het}}} \left(1 + \frac{T_s}{T_m}\right) + \mathcal{O}\left(\left(\frac{T_s}{T_m}\right)^2\right) \quad (2.2)$$

with γ_{12} denoting the interfacial energy between the substrate and the epiphyte, ΔH_{het} the change in enthalpy per unit volume for heterogeneous nucleation, T_m the melting point of the epiphyte and T_s the substrate temperature. The approximately linear proportion-

ality of the size of the column to the substrate temperature is experimentally confirmed for ultra-thin (<8 nm) films of the $\text{BiFeO}_3\text{-CoFe}_2\text{O}_4$ VAN [69]. For thicker films, an exponential increase of column size with deposition temperature is found, as the nuclei start to grow beyond their critical size at a rate limited by 2D diffusion of the arriving ionic species [71] (see also Fig. 2.1 (right side, [b])):

$$d^2 = 4 \frac{D_0}{\nu} \exp - \frac{E_a}{kT} \quad (2.3)$$

where d is the average diameter of the column, D_0 the diffusion constant at infinite temperature, E_a the activation energy, k the Boltzmann constant, T the temperature and ν the growth rate. Similarly to the Arrhenius equation, this is equal to a linear decrease of $\ln d^2$ with the inverse of T , which was experimentally observed in the $\text{BiFeO}_3\text{-CoFe}_2\text{O}_4$ and $\text{BaTiO}_3\text{-CoFe}_2\text{O}_4$ systems (see also Fig. 2.1) [4, 69].

Other external control parameters to tailor the morphology of nanostructures are the choice of crystallographic orientation of the substrate or the magnitude of relative phase fractions [71]. Regarding the stoichiometry, it is challenging to provide a common model among several VAN systems, as this depends on the specific phase diagram and miscibility. VAN systems for fully, partly miscible, and non-miscible phases have been experimentally demonstrated. However, within a single VAN system, stoichiometry provides powerful coarse- and fine-tuning control for the resulting structure, as results of the present work will demonstrate (see Section 5.2).

It has been theorized that VANs, in which the two phases are miscible, are formed by spinodal or pseudospinodal decomposition [67], as shown in Fig. 2.8. Here, in contrast to the nucleation-and-growth mechanism, the films first form a solid solution at the elevated growth temperature and later the total free energy is minimized by compositional phase separation during cooling. Simulation and experiment show that spinodal decomposition favors spatially ordered configurations such as the nano-checkerboard architecture [32] and has been reported in $\text{Zn}(\text{Ga}, \text{Mn})_2\text{O}_4$, $\text{Mg}(\text{Fe}, \text{Mn})_2\text{O}_4$, $(\text{Nd}, \text{Li})\text{TiO}_3$ and Mn-doped CoFe_2O_4 [12]. However, in general, it is less widely reported and seems to be much less understood and analyzed than the nucleation-and-growth mechanism [32]. Today little is known about how the oxide VAN formation via spinodal decomposition can be externally controlled and whether a transition regime or combination between nucleation-and-growth mode and spinodal decomposition exists for a system with limited miscibility.

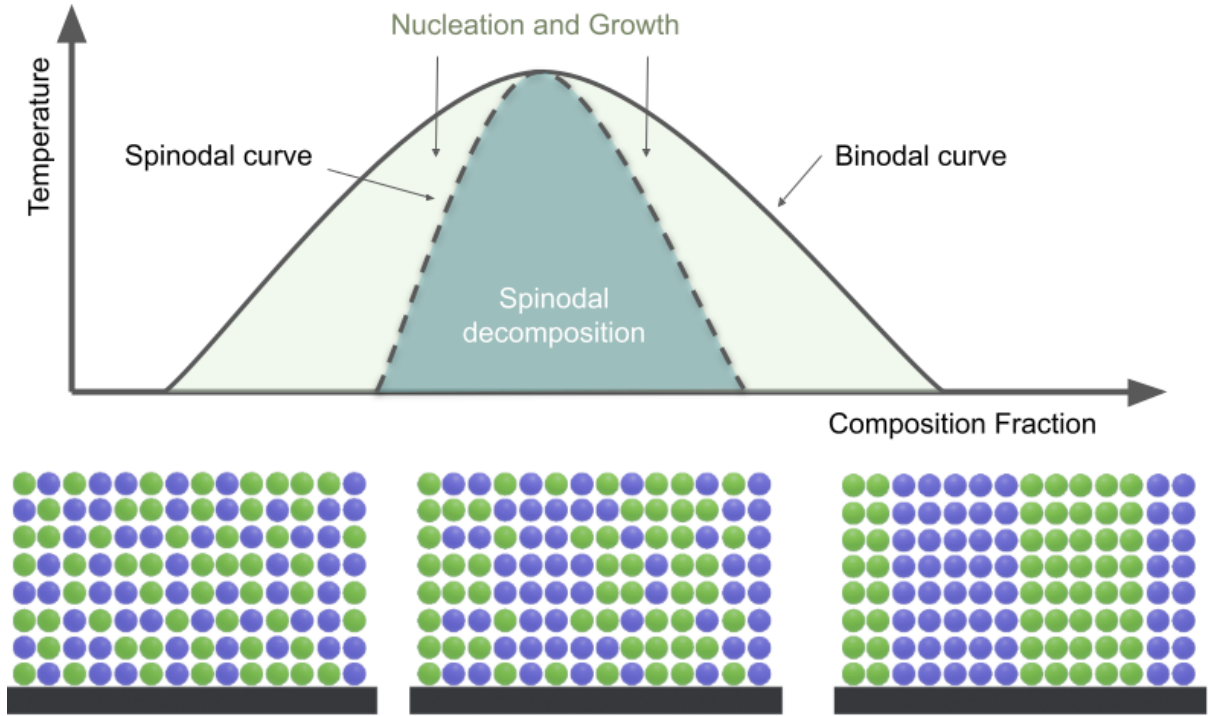


Figure 2.8: Top: Diagram depicting the regimes of nucleation-and-growth and spinodal decomposition for a two component system depending on composition fraction and temperature [67]. Bottom: Schematic representation of a spinodal decomposition process (From left to right, time increases).

2.1.4 Current vectors of VAN research

One of the next conceptual levels in nanocomposite thin film design could be envisioned as a combination of VANs with layered composites and superlattices to create three-dimensional composite structures with new anisotropic functionality [65]. Both controlled alternating deposition from single-phase and composite sources [72], as well as bottom-up self-assembly by choosing horizontally layered perovskites like Aurivillius phases as the matrix phase of the VAN, have recently been demonstrated to result in three-dimensional 'super-nanocomposites' [73, 74].

At first glance, simple, but indeed remarkable is the recent discovery of a VAN comprising isostructural, highly miscible perovskites SrRuO_3 and BaTiO_3 [35]. This possibility opens up a whole new subgroup of VANs, those with *isostructural* phases, that so far has not been studied at all.

With regard to the wide-spread technological application of VANs, expensive deposition methods and substrates eventually should be substituted by cheaper alternatives. Several studies have recently replaced pulsed laser deposition for VAN synthesis with simpler methods such as sputtering, electron-beam evaporation, or metal organic chemical vapor deposition [45, 75]. In addition, considerable efforts have been made to integrate VANs on silicon substrates, which were summarized in a recent review by Zhang et al. [76].

Beyond oxide-oxide VANs, metal-oxide VANs have received growing attention recently as a result of possible applications such as hyperbolic metamaterials and tunable waveguides. Relevant studies have recently been evaluated in a review by Misra and Wang [77].

2.2 Bulk photovoltaic effect in oxide ferroelectrics

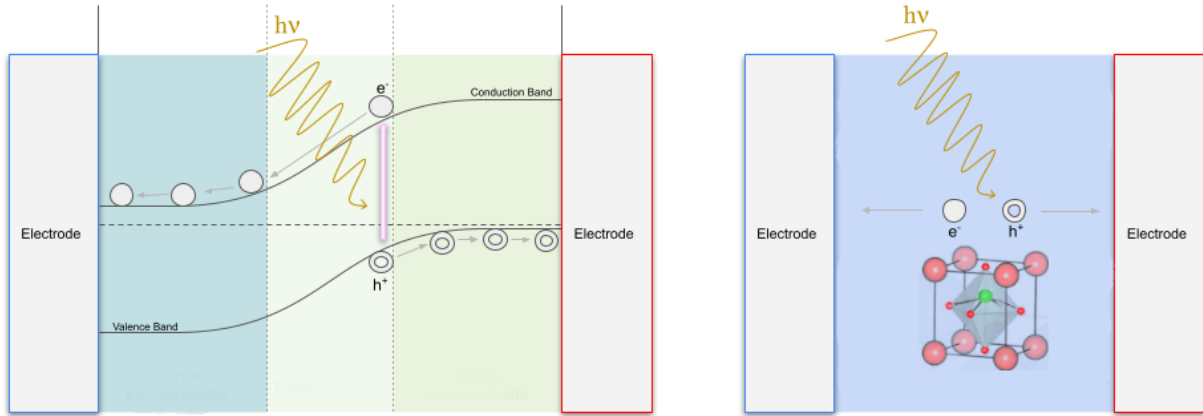


Figure 2.9: Schematics of charge separation mechanisms in a junction-based (left) versus BPVE-based (right) solar cell layout.

The photovoltaic effect is defined as the occurrence of an electric current and voltage under illumination. Microscopically, it is best described as a two-step process: First, the excitation of charge carriers across the band gap by photon absorption and second, the spatial separation of the electron-hole pair before recombination can occur.

A solar cell is a device that takes advantage of the photovoltaic effect to generate electrical power under illumination. The vast majority of proposed and realized solar cell devices introduce a spatial charge separation bias by introducing a junction (most often a p-n-junction). However, crystalline matter with a non-centrosymmetric unit cell exhibits a photovoltaic effect in the homogeneous bulk material, called the bulk photovoltaic effect (BPVE), or sometimes anomalous photovoltaic effect or photogalvanic effect. Here, the absence of inversion symmetry in the crystal structure itself provides a bias direction for a photocurrent. Fig. 2.9 shows the basic schematics of both mechanisms.

As no interface is involved in the bulk photovoltaic effect, the photogenerated voltage scales with the volume of illuminated material, with the sum of dark conductivity σ_d and photoconductivity σ_{ph} of the material determining the inverse proportionality between photogenerated voltage V_{ph} and current density J_{ph} :

$$V_{ph} = \frac{J_{ph}}{(\sigma_d + \sigma_{ph})}d \quad (2.4)$$

where d is the distance between the electrodes. [78]

Examples of such a current-voltage dependence are shown in Fig. 2.10 for material $\text{KNbO}_3:\text{Fe}$. Historically, the BPVE has been first and foremost observed and studied in bulk ceramic samples of similar oxide ferroelectrics, such as LiNbO_3 or BaTiO_3 [79, 80]. Since progress in thin film deposition has facilitated the synthesis of high-quality ferroelectric BiFeO_3 films, this material, due to its high polarization and low optical band-gap, has been responsible for much of the renewed interest in ferroelectric oxide BPVE [81–85].

It was further experimentally observed that the photogenerated current depends in magnitude and direction on the incident light polarization angle with oscillatory behavior, as presented in Fig. 2.11. Phenomenologically, this can be described by

$$J_i^{ph} = \beta_{ijk}^L e_j e_k^* I_0 + i \beta_{ik}^C [e e^*]_k I_0 \quad (2.5)$$

where e and e^* represent the electric polarization components of the incident light with amplitude I_0 , and β_{ijk}^L and β_{ik}^C the real and imaginary part of the complex bulk photovoltaic tensor β_{ijk} , associated with coupling to linearly and circularly polarized light, respectively. The shape of β_{ijk} is determined by the crystal symmetry.

In ferroelectric materials, the electric polarization arising from the crystal asymmetry can be reversed by applying an external electric field. In turn, the direction of the photocurrent and photogenerated field under illumination is switchable, as it is coupled to the polarization state of the material via the tensorial relation. As such, the BPVE has been proposed for the non-destructive readout of ferroelectric memory devices [87].

Although still a topic of active research, as of today, the fundamental origin of BPVE is understood to be a combination of coexisting ballistic current and shift current mechanisms [78]. Ballistic current is generated during illumination because of asymmetric momentum distributions of both non-equilibrium and non-thermalized charge carriers. In a noncentrosymmetric crystal, nonequilibrium carriers are subject to asymmetric scattering and recombination processes, while nonthermalized carriers pick up a shift in momentum when eventually thermalizing; both effects contribute to a net current flow. The shift current,

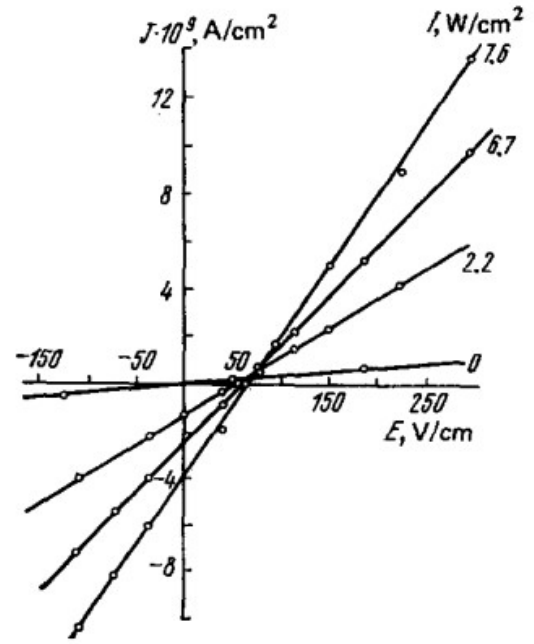


Figure 2.10: Current-voltage characteristics of the bulk photovoltaic effect in $\text{KNbO}_3:\text{Fe}$. Reprinted with permission from [79]. ©1978 Uspekhi Fizicheskikh Nauk.

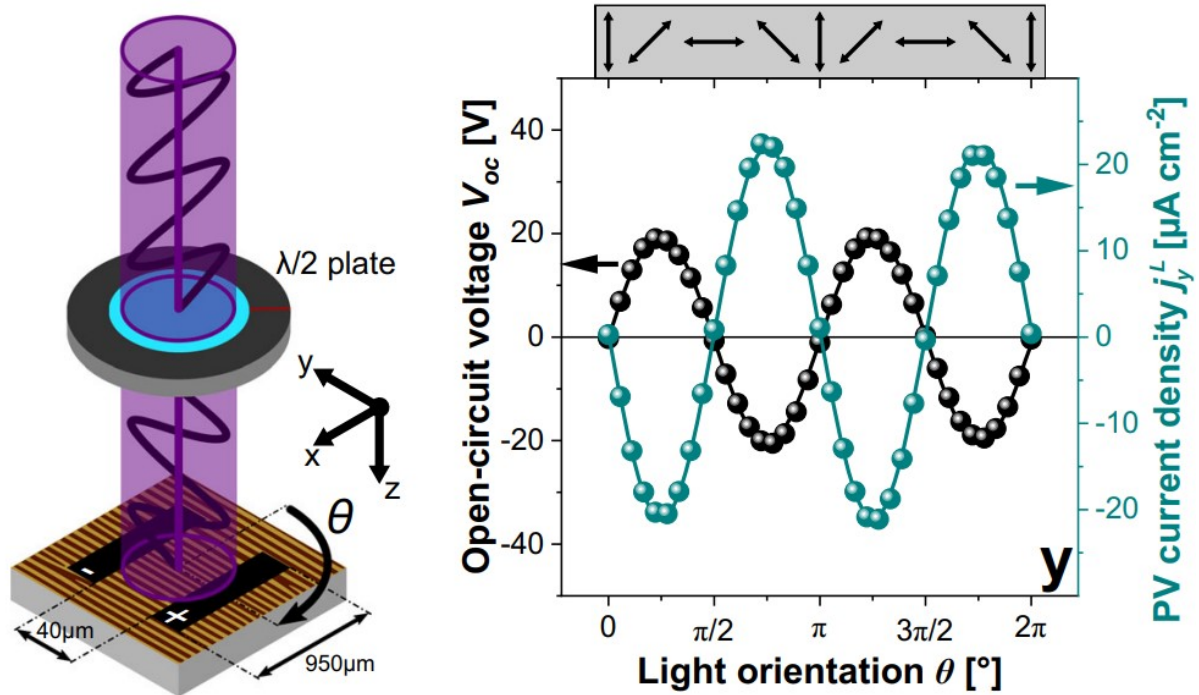


Figure 2.11: Oscillatory behaviour of photogenerated voltage and current in a BiFeO_3 thin film with stripe-pattern of ferroelectric domains (electrodes oriented perpendicular to the domain walls). Reprinted from [86] under the Creative Commons Attribution 4.0 International License.

on the other hand, originates at a nonlinear optical response from the interaction with second-order monochromatic light, resulting in a shift of a charge carrier in *real space* during band-to-band excitation. Interestingly, the magnitude of the shift current itself does not depend on the magnitude of the electric polarization of the material nor on the carrier lifetime or mobility [78], in contrast to the magnitude of the ballistic current. However, a prerequisite for the shift mechanism, just as for the ballistic mechanism, is the absence of inversion symmetry in the material.

In a real photovoltaic device made of a ferroelectric material, in addition to the BPVE, several extrinsic effects that can contribute to a photoresponse have to be considered, such as domain wall, depolarization field, and Schottky barrier contributions. Recent reviews by Pal et al. [78] and Han et al. [88] summarize the past and current understanding of these effects.

While the BPVE in oxide ferroelectrics can easily generate very high voltages up to thousands of volts, photocurrent densities are usually too low for practical energy conversion applications. This is mainly due to, first, low optical absorption and carrier excitation because of large optical band gaps, and second, poor charge separation because of high resistivity of the materials. Although the first issue has been successfully approached in part by doping with suitable elements [89, 90], it remains largely an open question how charge carrier separation can be improved without losing efficiency by simultaneously reducing the photogenerated field.

2.3 Potentials of bulk photovoltaic effect in VANs

The VAN architecture can be proposed to solve the problem of poor charge separation during BPVE in oxide thin films. Here, one or either of the phases or the interfaces acting as conductive channels could be utilized as 'highways' for charge separation to the top and bottom of the film. Although cohesive studies on this concept are still missing, indications for the plausibility of this approach have been reported in a limited number of studies, focusing on photoelectrochemical water splitting applications. In a $\text{SrTiO}_3:\text{ZnFe}_2\text{O}_4$ VAN, the photocurrent density was enhanced several times over what was achieved with single-phase SrTiO_3 or ZnFe_2O_4 films [91]. In both $\text{BiFeO}_3:\epsilon\text{-Fe}_2\text{O}_3$ and $\text{NiWO}_4\text{-WO}_3$ VAN, suppression of electron-hole recombination and improved charge carrier separation was explicitly proven by ultra-fast time-resolved and electrochemical impedance spectroscopy [10, 11].

In addition, vertical strain control could be utilized to induce high-polarization strain states over large thicknesses, improving both the overall light absorption and the generation of photocurrent via the bulk photovoltaic effect. With the vertical heterointerfaces acting as conductive channels, larger thicknesses are not necessarily bound to diminish the extraction of separated charge carriers.

In addition to vertical interface conduction, it has been argued that interface-induced polarization in composite architectures can promote charge separation via a built-in electric field between phases [54, 92].

In spite of these potentials, no studies have been performed addressing the potential of VANs for the exploitation of the bulk photovoltaic effect. In preparation for this thesis, both the $\text{BiFeO}_3:\text{Sm}_2\text{O}_3$ and the $(\text{Pb}, \text{Bi})(\text{Ti}, \text{Nb})\text{O}_3:\text{NiO}$ systems were studied from the perspective of photoelectronic effects. The results will be presented in Chapters 4 and 5, after the experimental methods used to reach the findings of the present work have been laid out in the following chapter.

Chapter 3

Experimental methods

3.1 Thin film growth

3.1.1 Substrate preparation

SrTiO₃ (STO), 0.5% wt. Nb-doped SrTiO₃ (Nb:STO), LaAlO₃ (LAO) and TbScO₃ (TSO) substrates were purchased from commercial suppliers listed in Table 3.1. The received substrates were of 10 x 5 x 0.5 mm dimensions with a polished surface on one side. Further specifications are found in Table 3.1. The received substrates were mechanically cut to pieces of 3 or 5 mm length and their surfaces were wet-chemically cleaned by a five-step protocol:

1. Ultrasonic soaking in acetone for 10 min
2. Ultrasonic soaking in fresh acetone for 3 min
3. Ultrasonic soaking in propan-2-ol for 3 min
4. Ultrasonic soaking in ethanol for 3 min
5. Ultrasonic soaking in deionized water for 3 min

Between each step, the substrate surfaces were rinsed carefully with the type of solvent already present on the surface, to prevent the transfer of dissolved contaminants to the next cleaning step. After the fifth step, the surfaces were rinsed with deionized water and dried in a stream of nitrogen gas. LAO and TSO substrates were subsequently annealed at 1000 °C for 2 h under ambient conditions. The STO and Nb:STO substrates were subjected to a hydrofluoric acid-based etching technique first reported by Kawasaki *et al.*[93] and later refined by Koster *et al.* [94] to achieve atomically flat surfaces and single TiO₂ surface termination. After the cleaning process, the substrates were again ultrasonically soaked for 10 min in fresh deionized water to form a Sr-hydroxide complex on the SrO-terminated parts of the surfaces. These complexes were dissolved from the

Material	SrTiO ₃	Nb:SrTiO ₃	LaAlO ₃	TbScO ₃
Supplier	CrysTec GmbH Berlin	CrysTec GmbH Berlin	Crystal GmbH Berlin	Crystal GmbH Berlin
Surface Orientation	001	001	001	110
Offcut Angle	0.1° - 0.15°	0.1 - 0.15°	< 0.1°	<0.5°
Comments		0.5 % wt. Nb		

Table 3.1: Specifications of substrates purchased from commercial suppliers.

surface by etching the substrates for 5 s in a 10:1 solution of deionized water and buffered HF etchant consisting of 74.5 % HF and 25.5 % NH₄F. After rinsing and drying, the substrates were annealed at 1000 °C for 2 h under ambient conditions. The effect of HF-based treatment is demonstrated in Fig. 3.1.

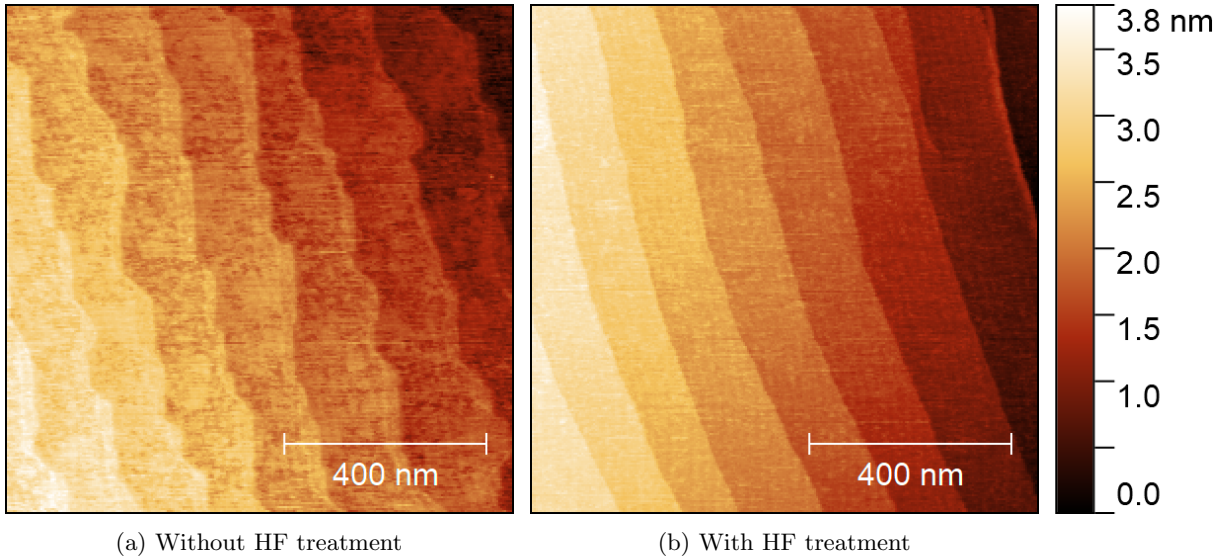


Figure 3.1: Effect of HF treatment on STO substrate surface. Topographies measured with AFM, see section 3.3.

3.1.2 Pulsed laser deposition

Thin films were deposited on the prepared substrates by Pulsed Laser Deposition (PLD). PLD became a popular technique during the search for high temperature superconductors and is nowadays a widely used technique in exploratory research on thin film growth because of its high degree of versatility and precise control of stoichiometry. In PLD, the heated substrate is placed at a certain distance facing a ceramic target from which the material is incrementally ablated by a series of high-energy laser pulses. The ablated material directionally propagates toward the substrate in the form of a plasma plume, subsequently encountering the substrate surface and forming a layer. A sizeable number of deposition parameters influence the growth process, either directly, like the substrate temperature or the background gas (availability of reactive ions, e.g. oxygen), or indirectly, like the laser fluence or frequency, influencing the shape and kinetic properties of the plasma plume, which in turn affects amount and kinetic energy of ions arriving at the

Parameter	Unit	Range
Substrate Temperature	$^{\circ}\text{C}$	$25 < T < 700$
Laser Fluence	J cm^{-2}	$0.6 < J < 2.0$
Pulse Frequency	f	$1 < f < 10$
Atmosphere (O_2, Ar)	mbar	$0.001 < p < 0.5$
Substrate-to-target distance	mm	$45 \leq d \leq 80$
Target rotation	rpm	15
Cooling rate	K min^{-1}	-20

Table 3.2: Variable process parameters of the PLD system *SURFACE systems+technology GmbH & Co. KG* used for thin film growth.

substrate surface. In this study, a commercial system by *SURFACE systems+technology GmbH & Co. KG* with a KrF excimer laser with a wavelength of 248 nm was used for sample synthesis. All variable parameters of this system can be found in Table 3.2. Details on the growth parameters for specific samples can be found in chapters 4 and 5.

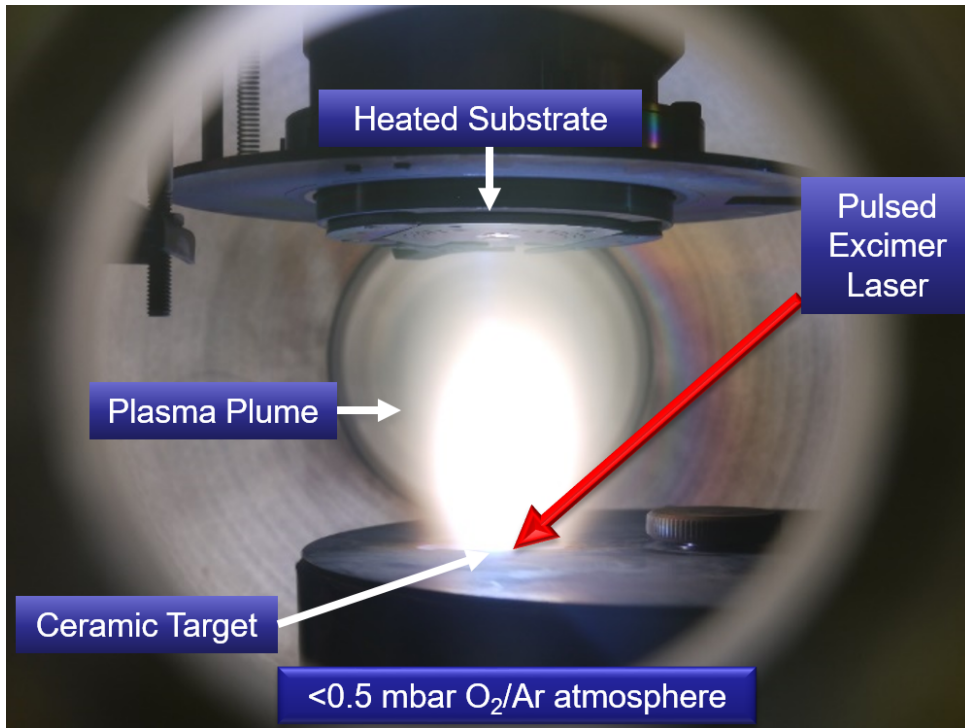


Figure 3.2: Annotated photograph of the PLD chamber during thin film deposition.

All doped ceramic targets used for PLD in this work were prepared by Dr. Chandra Bhal Singh from Indian Institute of Technology, Varanasi. For several paragraphs detailing the procedure of fabricating these targets, the reader is referred to Ch. 5, page 52. Pure targets of PbTiO_3 and BiFeO_3 were purchased from the commercial supplier *PI-KEM Ltd.*

3.2 X-ray diffraction

X-ray diffraction (XRD) analysis relies on the detection of constructive interference of x-rays from a periodic arrangement of scatterers, typically a crystal lattice, at characteristic incident angles. The Bragg condition for maximum diffracted intensity is fulfilled if the path difference between waves scattered from adjacent crystal planes is equal to n times the X-ray wavelength λ ,

$$n\lambda = 2d \sin \theta \quad (3.1)$$

where n is an integer (the diffraction order) and θ the angle between the surface normal and incident x-ray beam. Technically, in a high-resolution X-ray diffractometer, suitable for resolving the structure of epitaxial thin films, a highly collimated and monochromatic x-ray beam is directed onto the sample surface mounted onto an Euler cradle with full freedom of translation and rotation. An X-ray detector can be moved to a position with variable angles.

In the present work, 2θ - ω scans on a *Bruker D8 DISCOVER* diffractometer were utilized to resolve the crystal structure of the nanocomposite thin films. To this effect, the sample is mounted in a Bragg-Brentano geometry as shown in Fig. 3.3. It is then precisely aligned to the incident beam by applying offsets to all rotational and translational degrees of freedom so that the intensity of the diffracted beam for a known scattering condition - here, specifically the reflection from the (002) planes of the cubic (for the 001-oriented STO, LAO) or pseudo-cubic (for the 110 oriented TSO substrates) unit cell of the substrate - was maximized. Then, the sample is continuously rotated at a defined angular velocity within a defined range. At the same time, the detector is rotated at twice the angular velocity, so that the measured scattered intensity corresponds to interferences from the same crystallographic plane as used for alignment.

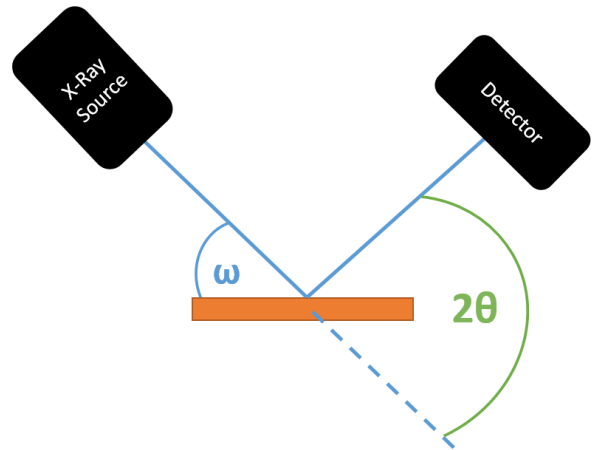


Figure 3.3: Bragg-Brentano geometry as used for XRD 2θ - ω scans. The sample and the detector rotate so that 2θ and ω continuously vary in unison.

Thus, the 2θ - ω scan enables evaluating periodicities perpendicular to the sample surface within the epitaxially grown thin film. Typically, this relates to the dimensions of the unit cell of the film, enabling extraction of its out-of-plane lattice parameter. Additionally, depending on the dimension and internal structure of the film, parts of the observed interference patterns may allow for extraction of the thickness of the film (from the Laue

oscillations, originating from incomplete destructive interference due to finite dimensions of the film [95]) or for resolution of periodic superstructures in the film, as illustrated in Fig. 3.4.

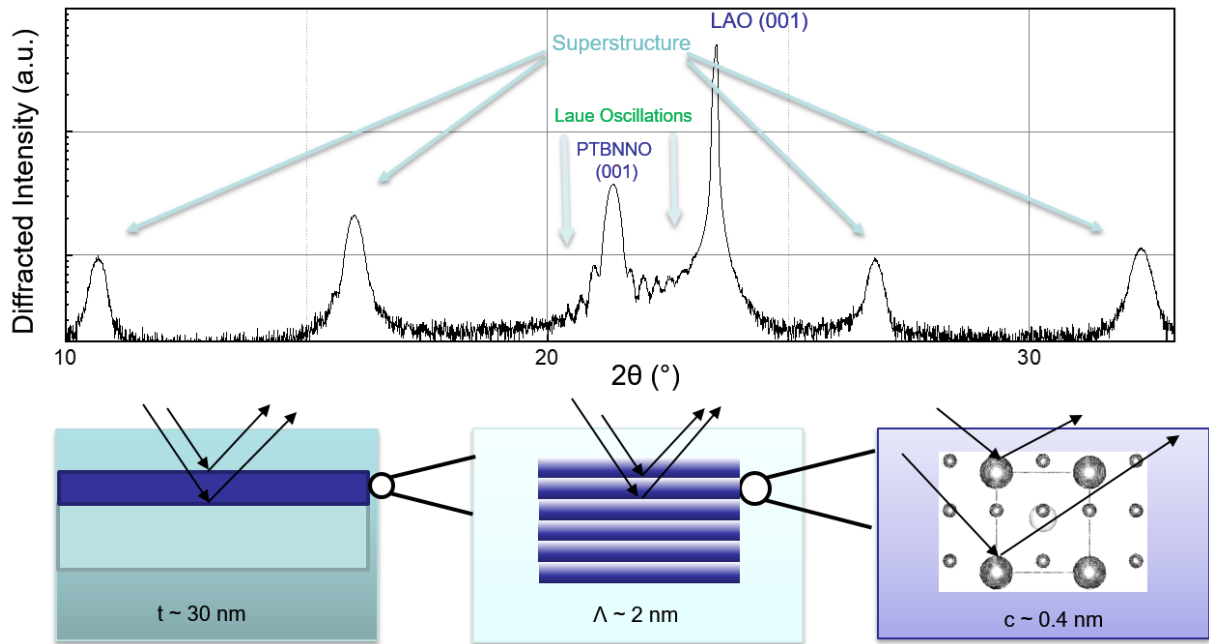


Figure 3.4: Example of diffraction pattern acquired by a 2θ - ω -scan on a $(\text{PbTiO}_3)_x(\text{BiNi}_{2/3}\text{Nb}_{1/3}\text{O}_3)_{1-x}$ film grown on an (001)-oriented LAO substrate. The two major diffraction peaks can be interpreted as the Bragg reflections from the (001) planes of the LAO and PTBNNO unit cells. While the Laue oscillations in the immediate vicinity of the PTBNNO Bragg reflection are due to the finite film thickness, the symmetrically distributed peaks further away can be attributed to the formation of a layered superstructure with a period length of about 2 nm. For further details on the quantitative analysis of the superstructure layer periodicity, the reader is referred to the discussion of these thin film systems in Chapter 5.2.

3.3 Atomic Force Microscopy

Atomic force microscopy (AFM) is a variant of scanning probe microscopy that allows topographic mapping of surfaces with resolution down to the atomic level. A thin, flexible cantilever with a sharp tip at its end is scanned across a surface at such close proximity that the interatomic forces between the tip apex and the surface become significantly large to displace or bend the cantilever. For all practical purposes, the dependence of the magnitude of these forces on the tip-to-surface distance can be modeled by combining the short-range Pauli repulsion with the medium-range attractive London dispersion force within the Lennard-Jones potential as depicted in Fig. 3.5. As such, the AFM can be operated in contact mode, with the tip being in physical contact with the sample surface, relying on the effect of repulsive forces, or in non-contact mode, where the tip remains vertically separated from the surface and the effect of the attractive force is measured. A variation of the non-contact mode is the tapping mode, in which the cantilever is me-

chanically oscillated at its resonance frequency, bringing the tip into and out of contact with the surface, or, in certain realizations of the tapping mode, back and forth from the non-interacting regime to the attractive regime of the Lennard-Jones potential. In both cases, the magnitude of the forces acting on the tip induces a proportional shift in the effective resonance frequency of the cantilever, which decreases the amplitude of its oscillation compared to the freely oscillating cantilever under constant drive frequency. The detection of this decrease leads to high-resolution images, while preserving the structural integrity of the tip over prolonged use, in contrast to the contact mode, which is prone to damage the tip.

During AFM, the backside of the cantilever is illuminated with the output of a laser diode, which it reflects onto a photodetector that converts any displacement of the cantilever into an electrical signal. This signal is fed into a controller that supplies a corresponding control signal to a piezoelectric actuator that moves the cantilever vertically (Z-Scanner). Thus, a feedback loop is created that is typically set up so that the height of the cantilever above the surface remains constant. At the same time, the amplitude of the feedback control signal is recorded as the cantilever is scanned across a defined sample region, which results in a map of the local topography.

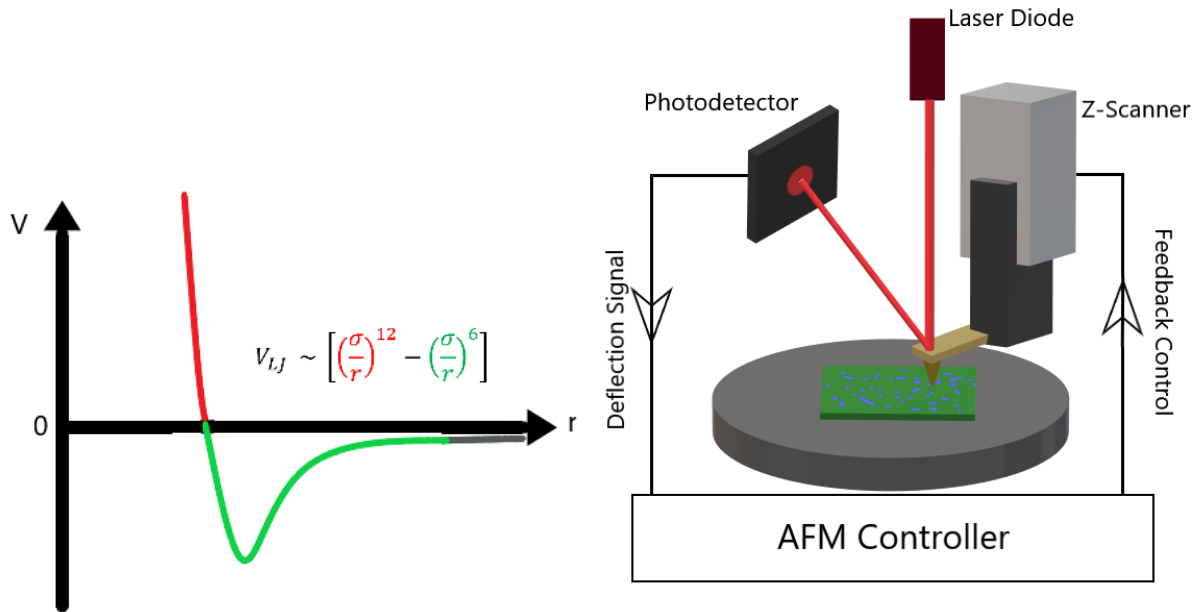


Figure 3.5: *Left*: Qualitative dependence of the Lennard-Jones potential V on the interatomic distance r , with the repulsive and attractive regimes highlighted in red and green, respectively. *Right*: Schematic of an AFM measurement setup.

Topography images throughout this work were acquired with an NX-10 AFM from *Park Systems*, operating in tapping mode and equipped with NSC14 cantilevers from *Mikro-Masch* with a thin wear-resistant diamond-like carbon coating on the tip and an aluminum reflective coating on the backside.

3.3.1 Conductive Atomic Force Microscopy

Conductive Atomic Force Microscopy (C-AFM) refers to an AFM measurement setup in which, in addition to topography, the electrical conduction properties of the sample are simultaneously measured and thus spatially resolved. To this effect, a cantilever with a conductive coating is used, and the sample is electrically grounded. During the C-AFM scan, a constant voltage is applied between the cantilever and the sample while the resulting current is fed into a current amplifier and recorded.

In contrast to the topography measurements mentioned in the section above, for C-AFM measurements the NX-10 AFM was operated in contact mode and equipped with NSC15 cantilevers from *MikroMasch* with an electrically conductive platinum coating. The tip radius of these cantilevers is below 30 nm, which allows for spatial resolution of the conductive properties of the nanostructures investigated in this work. A low noise current amplifier from *FEMTO Messtechnik GmbH* was used to amplify the signal before supplying it to the AFM controller to create a spatially resolved map of conductance, in addition to the surface topography.

Additionally, C-AFM was performed under illumination to quantify and spatially resolve the photoconductance. A custom setup supplied by *Park Systems* was used in which a small laser diode with an output power of around 9 mW and a wavelength of 405 nm was installed next to the sample mount and focused onto the area of the point of contact of the tip with the sample.

In all cases, the thin film samples for these measurements were deposited on conductive Nb:STO substrates, which were electrically contacted from all sides to the grounded sample holder with silver paste, so that no bottom electrode layer had to be inserted before epitaxial deposition of the thin film.

3.4 Photoelectrical measurements

3.4.1 Electrode fabrication

Patterning

For photoelectric measurements on a macroscopic scale, the bottom contact was again achieved via the conductive Nb:STO substrate. For the realization of a suitably sized top electrode, a conventional photolithography procedure was used to enable fabrication of structured contacts. A circular electrode shape with a diameter of 100 μm was selected, keeping its dimension well below the area of approximately constant intensity for all light

sources used for photoelectric measurements. To this effect, the samples were first spin-coated with a conventional p-type photoresist. A direct write photolithography machine¹ was used to expose an area of the resist-covered surface to a predefined dose of UV light. The pattern was then developed by dissolving the light-exposed parts of the photoresist in a developer solution, while the unexposed parts of the samples continued to be covered by resist. Subsequently, the transparent conductor Indium tin oxide (ITO) was deposited by PLD as detailed in the next section. Finally, the remaining photoresist was stripped by carefully rinsing the sample with acetone, removing with it any superfluous ITO, resulting in a sharply defined top electrode.

Indium Tin Oxide

Subsequent to electrode patterning, ITO was deposited as electrode material by pulsed laser deposition from a ceramic target² containing In_2O_3 and SnO_2 at a weight percentage of 95 and 5 pounds, respectively. As the previously deposited photoresist is prone to evaporate at elevated temperatures, a method was developed to carry out the ITO deposition process at room temperature. The deposition was carried out at a target-to-film distance of 60 mm with a laser fluence of 0.85 J cm^{-2} and a laser repetition rate of 10 Hz. For these parameters, the growth rate was experimentally determined by thickness measurements *via* atomic force microscopy on resultant samples to $7.0(3) \text{ \AA s}^{-1}$. Kim et al. have reported high quality ITO films by PLD grown at room temperature, yet at the same time demonstrated a very high quality sensitivity on the amount of O_2 pressure during deposition [96]. While excessive O_2 pressure prevents the formation of oxygen vacancies that are needed for conduction in ITO, too low O_2 pressure leads to poor crystallinity and resulting low mobility for charge carriers [97], again lowering conductivity. In addition, a higher concentration of oxygen vacancies leads to a higher free carrier absorption, reducing the transmittance [96]. To optimize this critical parameter and ensure the required transparency and conductivity of the resultant ITO, films of 70 nm thickness were deposited onto 2x2 cm wide and 1 mm thick glass substrates at different values of background O_2 pressure. The transmission of the film-glass system was measured by illuminating from the film side with the monochromated output of a xenon light source³ and detecting the transmitted light with a biased Si photodetector⁴ connected to a multimeter⁵. To calculate the transmittance of the film-glass system, the measured current at each wavelength was divided by the current measured without a sample in the way of illumination. The resistivity of the ITO films was determined by the van der Pauw method, contacting the square film at the four corners and detecting the resistance with an Ohmmeter⁶. The

¹Durham Magneto Optics MicroWriter ML®3

²Purchased from commercial supplier PI-KEM Ltd.

³TLS120Xe High Power Tunable Light Source by Bentham Instruments

⁴DET100A2 by Thorlabs

⁵Multimeter 2000 by Keithley Instruments

⁶SourceMeter 2450 by Keithley Instruments in 4-point-probe Ohmmeter mode

results are presented in Figure 3.6.

The measured values for resistivity and transmittance agree well with the values previously reported on ITO films deposited by PLD at room temperature [96]. The lowest resistivity of $8.5 \times 10^{-2} \Omega \text{ cm}$, corresponding to a sheet resistance of 120Ω , is achieved at 0.02 mbar O_2 pressure with an average transmission of the film-glass system of 83%. Only slightly improved performance can be achieved by elevating the deposition temperature to 300°C , as Kim et al. reported [96]. The reduction of O_2 pressure leads to loss in both conduction and transmittance, while for an increase in pressure the drastic negative effect on conductivity outweighs the slight gain in transmittance, rendering room-temperature deposition in 0.02 mbar O_2 atmosphere optimal for the given purpose.

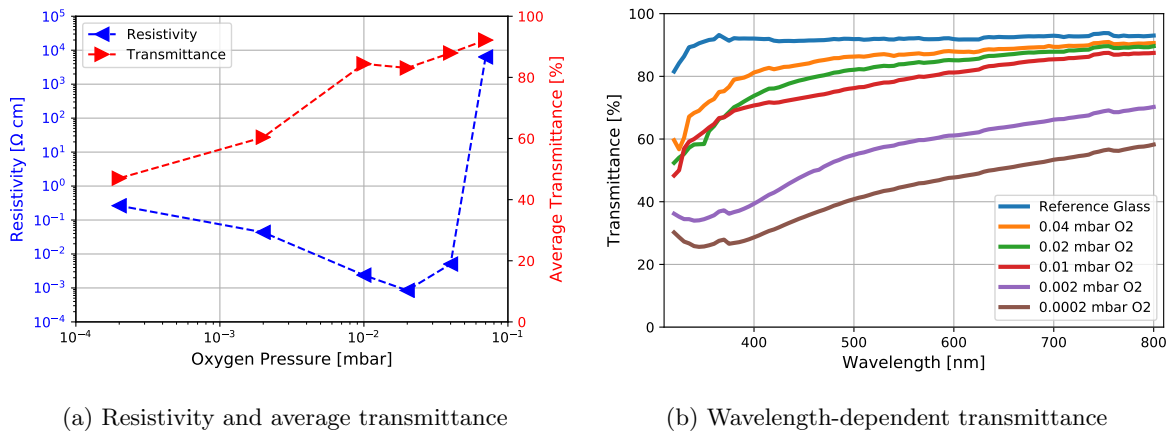


Figure 3.6: Dependence of resistivity and transmittance of the 70 nm thin ITO films on top of 1 mm thick glass slides on the O_2 background pressure during room-temperature PLD. The transmittance in (a) was calculated by averaging the results presented in (b) over the wavelength.

3.4.2 Illumination and electrical equipment

For illumination with 405 nm laser light of varying intensity, a fixed wavelength diode laser from *Cobolt AB* with a beam diameter of $700 \mu\text{m}$ was used. Measurements under solar spectrum conditions were performed with a xenon arc lamp solar simulator of from *Abet Technologies*, the temporary use of which was kindly facilitated by the Fraunhofer Center for Silicon Photovoltaics, Halle (Saale). The voltage application and current measurement were performed with a 6517B Electrometer from *Keithley Instruments*.

3.5 Additional characterization

In addition to the experimental methods carried out by the author at the facilities of Martin-Luther-University Halle-Wittenberg and ZIK SiLi-nano, as detailed in the above sections of this chapter, vital contributions to the present work were made by third parties.

Imaging of the nanocolumnar structures with atomic or near-atomic resolution was achieved by Transmission Electron Microscopy (TEM), in which a focused beam of electrons is transmitted through a thin slice of the sample and the resulting diffraction pattern is detected and analyzed. In conjunction with TEM, Energy-Dispersive X-ray Spectroscopy (EDS) was applied in order to resolve the segregation of elements into nanocolumns and surrounding matrix. In EDS, the X-rays that are emitted by atoms after excitation by incoming high-energy electrons are detected, which allows the identification of atomic species by comparing the wavelengths detected with known characteristic emission patterns of the elements. Spectroscopic Ellipsometry (SE) was used to determine the optical absorption spectra of the VAN structures. In SE, a polarized light beam is directed onto the sample at an angle and the change in polarization of the reflected light is measured as a function of wavelength, allowing simultaneous deduction of the refractive index, thickness, and absorption coefficient of the sample material. Ferromagnetic hysteresis and magnetic field-cool/zero-field-cool measurements were carried out with a SQUID (Superconducting Quantum Interference Device) magnetometer. While different versions of SQUIDs exist, in the present case the magnetization of the samples was determined by measuring the change in magnetic flux when mechanically moving the sample within a superconducting coil.

While these definitions were intentionally kept short and limited to explaining the respective basic measurement principle, in-depth information on the specific types of instruments and analysis methods used in each case are found in the following chapters next to the corresponding results and are indicated along with the original contributors in the following list:

- High-resolution TEM with EDS analysis and nanobeam-electron diffraction on the BFO-SmO system was performed by Dr. Angelika Hähnel from the Fraunhofer Institute for Microstructure of Materials and Systems IMWS, Halle (Saale). Details on the instruments and analysis method used can be found in Ch. 4, on page 37.
- High-resolution TEM with EDS analysis for the PTO-BNNO system was performed by Dr. Andriy Lotnyk from the Leibniz Institute of Surface Engineering, Leipzig. Details on the instruments and analysis method used can be found in Ch. 5, on pages 54 and 62.
- Optical characterization via SE was performed by Dr. Cameliu Himcinschi from the Institute of Theoretical Physics, TU Bergakademie Freiberg. Details on the instruments and analysis method used can be found in Ch. 5, on page 62.
- Magnetic characterization via SQUID magnetometry was performed by Dr. Ignasi Fina of the Institut de Ciència de Materials de Barcelona-CSIC, Barcelona. Details on the instruments and analysis method used can be found in Ch. 5, on page 62.

Chapter 4

Part A - BiFeO₃:Sm₂O₃ system

This chapter presents the results of the research conducted on the BiFeO₃:Sm₂O₃ nanocomposite thin film system, as published in the following peer-reviewed article:

[LM1] Mühlenbein, L., Bhal Singh, C., Hähnel, A., Campbell, S., Hagendorf, C., & Bhatnagar, A. (2020). Impact of Samarium on the Growth of Epitaxial Bismuth Ferrite Thin Films. *Physica Status Solidi (B)*, 257(7), 1900625. Reprinted under the Creative Commons license.

The publication revisits a string of articles published by researchers around Driscoll [21, 44, 98] on a self-assembled nanocomposite when ablating from a mixed 50:50 BFO:SmO target, and for the first time discusses them in context with another set of articles released a short time later by researchers around Nagarajan [99, 100], that report on substitutional doping of BFO with Sm (providing data up to 20% Sm doping level). New experimental data recreating both Nagarajan's and Driscoll's synthesis experiments (at 20% and 50% Sm) was collected at the facilities of ZIK SiLi-nano, MLU Halle-Wittenberg, and Fraunhofer IWMS. It unveils a novel kind of nanocomposite at 50% doping level, different from the one previously reported by Driscoll, while certain structural and electrical properties show similarities with their work. In addition, the leakage and photoconduction properties of films are evaluated at three different doping levels (0%, 20%, 50%).

4.1 [LM1] Impact of Samarium on the Growth of Epitaxial Bismuth Ferrite Thin Films

Impact of Samarium on the Growth of Epitaxial Bismuth Ferrite Thin Films

Lutz Mühlenbein, Chandra Bhal Singh, Angelika Hähnel, Sade Campbell, Christian Hagendorf, and Akash Bhatnagar*

Doping of rhombohedral bismuth ferrite (BFO) with rare earth elements has been widely investigated as a pathway to extract ferromagnetic response from an otherwise antiferromagnetic material. However, increased level of such doping, in conjunction with the ability of BFO to accommodate large strain, has also resulted in nontrivial changes in the structure, i.e., transition to orthorhombic structure and phase separation to form vertically aligned columns. Herein, epitaxially grown and single crystalline samarium oxide (Sm_2O_3) and doped BFO films are used to investigate the structural evolution. Thin films are grown from undoped (BFO and Sm_2O_3) and doped targets, $(0.2,0.5)\text{Sm}_2\text{O}_3-(0.8,0.5)\text{BFO}$. In addition, the in-plane strain, imposed by the lattice mismatch between film and substrates, is used to demonstrate the stability of the structures formed in the doped films. Interestingly, the resultant orthorhombic structures are found to be largely independent of the underlying substrates. In-depth structural and nanoscopic measurements are conducted to investigate the structures. Ordered columnar structures, reminiscent of phase separation, are successfully obtained albeit driven by spontaneous ordering of differently oriented crystals.

1. Introduction

Thin films of bismuth ferrite (BiFeO_3 , BFO) have been intensively studied since the mid-2000s due to the intriguing ferroelectric, magnetic, and optical properties of this material.^[1] In addition, being one of the few room-temperature multiferroics, BFO is also regarded as a lead-free alternative to the widely used Pb-based piezoelectrics, but the industrial application is hindered by high leakage currents and large coercive fields.^[2] To counter this problem, and simultaneously enhance the multiferroic properties, several studies have been conducted in which the A-site of the perovskite unit cell of BFO has been partly substituted with rare earths such as samarium, with inspiration drawn from the positive impact of substitutional doping in Pb-containing ferroelectrics such as $\text{Pb}(\text{Zr,Ti})\text{O}_3$.^[3–5]

While Yuan and Or pioneered the field of Sm-doped BFO ceramics,^[6] the first synthesis of thin films of BFO-containing samarium was conducted by Driscoll et al.^[7–9] Motivated by the work on vertically aligned nanocomposites comprising of BFO and CoFe_2O_4 ,^[10] a sintered target containing BFO and Sm_2O_3 (SmO) in 1:1 molar ratio was used to grow epitaxial thin films on single-crystal SrTiO_3 substrate by pulsed laser deposition (PLD). A spontaneous phase separation into an ordered array of BFO and SmO columns was observed. It was further proven that with increasing film thickness, the strain state of the film switches from lateral strain control, originating at the substrate–film interface, to vertical strain control arising from the columnar interfaces between BFO and SmO. As a consequence, the out-of-plane lattice parameter of BFO reduced from 4.000 Å in a pure BFO film to about 3.905 Å in the BFO:SmO composite film of around 50 nm film thickness. Upon comparison with the bulk value of 3.962 Å, this was interpreted as a change from in-plane compressive strain induced by the STO to out-of-plane compressive strain induced by the SmO. Although intermixing of the phases was initially not reported, it was later theorized that, although intermixing might take place during growth, the phases subsequently separate by spinodal decomposition.^[11]


However, studies conducted by Cheng et al. demonstrated that Sm^{3+} with an ionic radius of 1.24 Å, at 12-fold coordination, can substitute Bi^{3+} (1.365 Å ionic radius) at the A-site of the

L. Mühlenbein, S. Campbell, Dr. A. Bhatnagar
Zentrum für Innovationskompetenz SiLi-Nano
Martin-Luther-Universität Halle-Wittenberg
06120 Halle (Saale), Germany
E-mail: akash.bhatnagar@physik.uni-halle.de

L. Mühlenbein, Dr. A. Bhatnagar
Institute of Physics
Martin Luther Universität Halle-Wittenberg
06120 Halle (Saale), Germany

C. Bhal Singh
School of Materials Science and Technology
Indian Institute of Technology (Banaras Hindu University)
221005 Varanasi, India

Dr. A. Hähnel, Dr. C. Hagendorf
Diagnostik und Metrologie
Fraunhofer Center für Silizium-Photovoltaik
06120 Halle (Saale), Germany

 The ORCID identification number(s) for the author(s) of this article can be found under <https://doi.org/10.1002/pssb.201900625>.

© 2020 The Authors. Published by WILEY-VCH Verlag GmbH & Co. KGaA, Weinheim. This is an open access article under the terms of the Creative Commons Attribution-NonCommercial License, which permits use, distribution and reproduction in any medium, provided the original work is properly cited and is not used for commercial purposes.

DOI: 10.1002/pssb.201900625

perovskite unit cell in $\text{Bi}_{1-x}\text{Sm}_x\text{FeO}_3$ thin films synthesized by PLD^[12,13] at least up to $x = 0.3$. In addition, a phase transition from the ferroelectric rhombohedral phase with polar R3c symmetry to an paraelectric orthorhombic Pnma phase at $x = 0.14$ was observed, with a narrow transition region exhibiting antiferroelectric behavior at the phase boundary. The occurrence of such a phase transition was confirmed in another independent study^[14] and in experiments conducted on ceramic samples.^[15] Interestingly, here as well a massive reduction of the out-of-plane lattice parameter was reported with $c = 3.915 \text{ \AA}$ in a film with $x = 0.2$.

Similar observations were made in 200 nm thick films of $\text{Bi}_{0.85}\text{Sm}_{0.15}\text{MnO}_3$, where c was reduced from 3.98 \AA in a pure BiMnO_3 film to $c = 3.87 \text{ \AA}$ in the composite film, which was attributed to a reduction in Mn–O bond length and an increment in octahedral rotations.^[16,17]

Considering the diversity of results reported so far, the system of Sm-incorporated BFO can be considered as an exciting system to investigate the different realms of thin-film growth spread across conventional doping, phase separation, and change in symmetry.

In this work, we used PLD to synthesize single crystalline and epitaxial films of $x\%$ Sm-doped BiFeO_3 films with different content of Sm ($x = 0\%$, 20% , and 50%) on single-crystalline cubic STO (001) and orthorhombic TbScO_3 (TSO) (110) substrates. Well-ordered columnar structures were successfully obtained with increased levels of doping. The samples were analyzed with X-ray diffraction (XRD), transmission electron microscopy (TEM), and surface probe methods to unravel the underlying origin of the structures.

2. Results

2.1. Structural Analysis by XRD

We first focus to confirm the suitability of deposition parameters used in the current study for the ablation of BFO and SmO. This is essential since the elements involved have evidently different atomic numbers which can result in drastically different kinetic energies of the ablated species, and thus the growth rate. Time- and space-resolved optical emission spectroscopy studies in the case of LaAlO_3 and LaGaO_3 have confirmed the validity of such a scenario wherein the difference between the kinetic energies of La and Ga ions was found to be around 1.8 times.^[18] In **Figure 1**, the XRD scans acquired from pure BFO and SmO films deposited with identical deposition conditions on STO substrates are presented. The peak arising from BFO is apparently shifted to the left of the STO (002) peak, indicating an elongated out-plane lattice parameter c . The c_{BFO} was extracted to be around 4.06 \AA , which can be attributed to $\approx 1.5\%$ compressive strain imposed by the substrate. In the case of SmO, a sharp (004) reflection of the cubic phase is apparent. From the exact positions of the (004) peak of the cubic phase, the out-of-plane lattice parameter can be estimated to $c_{\text{SmO}} = 10.815 \text{ \AA}$. This value is slightly lower than the reported lattice parameters from the bulk cubic phase which are around 10.93 \AA .^[19] A unit cell of SmO which is rotated in-plane by 45° and positioned along [110] direction can be accommodated on STO (001), albeit under tensile strain of 1.2% .^[7,19] The reduced value of c_{SmO} supports the validity of

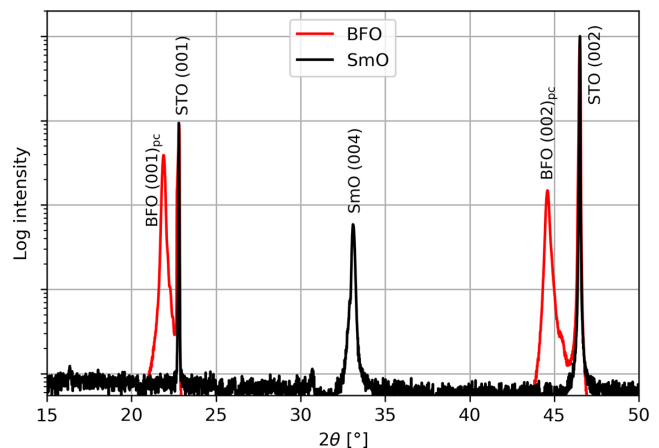


Figure 1. X-ray $\omega - 2\theta$ diffraction pattern of pure BFO and SmO thin films on STO.

such a scenario in the growth of SmO and this result is in good agreement with reports on SmO thin films on STO by Yang et al.^[19] Hence, the deposition parameters can be considered appropriate for the ablation of composite targets.

In **Figure 2a**, the X-ray $\omega - 2\theta$ diffraction pattern from thin films deposited on STO from $\text{Bi}_{1-x}\text{Sm}_x\text{FeO}_3$ targets with $x = 0$ (BFO), $x = 0.2$ (80BFSmO), and $x = 0.5$ (50BFSmO) are presented. Interestingly, separate peaks from SmO are not observed, with only the (001) and (002) reflections arising from a BFO-like perovskite phase being visible, which indicates that phase separation has not occurred. The inset presents a magnified image for the (002) reflection, where a gradual shift of the (002) reflection with increasing Sm content is evident. The extracted out-of-plane lattice parameters are plotted **Figure 3**. In particular, in the sample with the highest Sm content, 50BFSmO, the reflections from BFO and STO are almost indistinguishable, with only the presence of a slight shoulder-like feature. Identical films were also grown on TSO to observe the role of in-plane strain, if any, in the growth of the composites. In **Figure 3**, the resultant c_{BFO} have been coplotted. The in-plane strain clearly has a striking impact on the growth of pure BFO with the c_{BFO} on TSO similar to the bulk value of 3.96 \AA , and around 4.06 \AA on STO. Interestingly, the c values of the composites are largely independent of the in-plane strain as roughly identical values are extracted from the films grown on STO and TSO. A scenario wherein such independence from horizontal or in-plane strain can manifest is via the formation of vertical columns. Similar observations were made in the work from Driscoll et al. wherein the films grown from the composite target with 1:1 molar ratio of BFO and SmO resulted in BFO with highly compressed c_{BFO} nearly equaling c_{STO} , albeit with a peak arising from pure SmO also visible.^[7] Together with TEM and a thickness variation study, the existence of phase-separated columns was proven and it was claimed that the vertical strain imposed by the SmO columns prompts the massive reduction in the BFO out-of-plane lattice parameter.

Having no indication of phase separation in the XRD pattern, we cannot assume this to be the case here. On the contrary, our

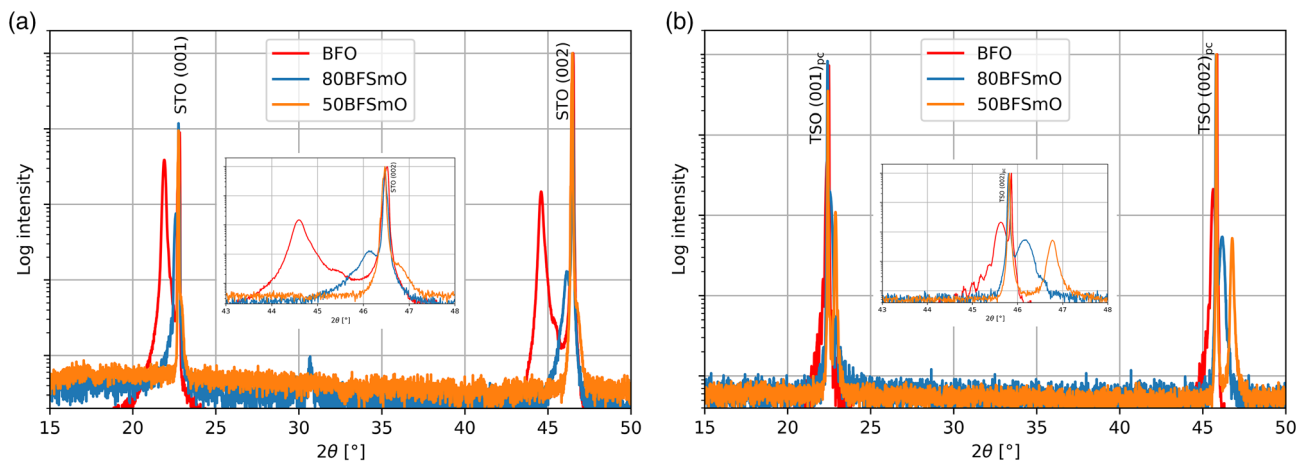


Figure 2. X-ray $\omega - 2\theta$ diffraction pattern of BF(Sm)O thin films on a) STO and b) TSO.

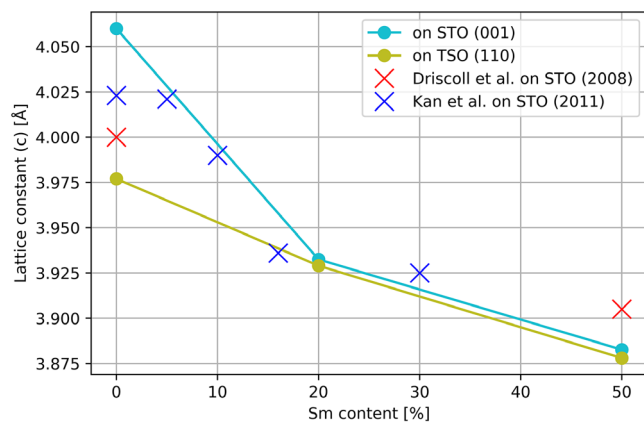


Figure 3. Out-of-plane lattice parameters of BF(Sm)O films on STO and TSO extracted from XRD. For comparison, values reported in refs. [7] and [20] from growth on STO (001) are also indicated.

results indicate that substitutional doping on the A-site as first reported by Cheng et al.^[12] can extend up to $x = 0.5$ with no phase separation taking place. Increasing Sm substitution leads to a decrease in the average ionic radius on the A-site of the perovskite unit cell, and in turn, a structural phase transition from the rhombohedral BFO-like phase to an orthorhombic phase occurs around $x = 0.14$.^[13] This seems all the more reasonable as even thin films of pure SmFeO_3 (SFO) have been grown in the orthorhombic phase on STO by PLD.^[21]

Apart from the samples grown at the parameters specified in the Experimental Section and presented here, we have also explored a broad range of the parameters available to a standard PLD system in search for phase separation, between 580 and 700 °C, 0.667 and 0.2 mbar O_2 atmosphere, and 2 and 10 Hz of laser pulse frequency, without a reliable indication of a SmO (004) peak. Also noteworthy to mention is the position of Bi_2O_3 peak, a common secondary phase in BFO,^[22] which usually appears around same value of 2θ as SmO (004). Therefore, extra caution must be exercised in the interpretation of any peak that appears within this range of 2θ .

2.2. Atomic Force Microscopy

In **Figure 4**, the surface topography of the thin films on Nb:STO as measured by atomic force microscopy (AFM) is presented. As the surface is free of precipitates and simple oxides, the respective surface roughness is governed by the grain boundaries. In agreement with existing reports,^[23] the pure BFO film on STO shows uniform grains with a lateral size parameter of about 300 nm each and root mean square (RMS) roughness of 1.687 nm. As is evident, the grain size and RMS roughness (0.441 nm) reduces significantly with increasing dopant concentration in the film with $x = 0.5$, which is also in good agreement with studies on the grain sizes in ceramic samples of Sm-doped BFO.^[15] Also, the topography and grain size in the film with $x = 0.5$ resembles very much the topography of the reported films with columnar architecture as is shown in the previous studies of Yang et al.,^[23] where the grains, however, were assumed to be nanocolumns consisting of separate BFO and SmO phases.

The resulting rectangular faceted grains in our Sm-containing samples furthermore bear striking resemblance with the surface morphology of $\text{Bi}_{0.85}\text{Sm}_{0.15}\text{MnO}_3$ thin films reported by Choi et al. where domain twinning was observed.^[16] Cheng et al. had earlier observed peak splitting in zone-axis selected-area diffraction patterns during TEM of single-phase $\text{Bi}_{0.8}\text{Sm}_{0.2}\text{FeO}_3$ thin films on STO, which they attributed to twin domains.^[12]

2.3. Transmission Electron Microscopy

To decisively determine whether a columnar nanostructure is present in our samples, we investigated cross-section focused ion beam (FIB)-lamellae of the BFSmO/STO stacks using TEM. **Figure 5a** shows TEM overviews of 80BFSmO and 50BFSmO thin films on STO substrates. The 80BFSmO film (upper pane of **Figure 5a**) seems rather homogeneously structured, whereas a clear presence of nanocolumns can be observed in the 50BFSmO film (lower pane of **Figure 5a**). In particular, the nanocolumns are perpendicular to the interface between film and substrate with diameters of 10–50 nm.

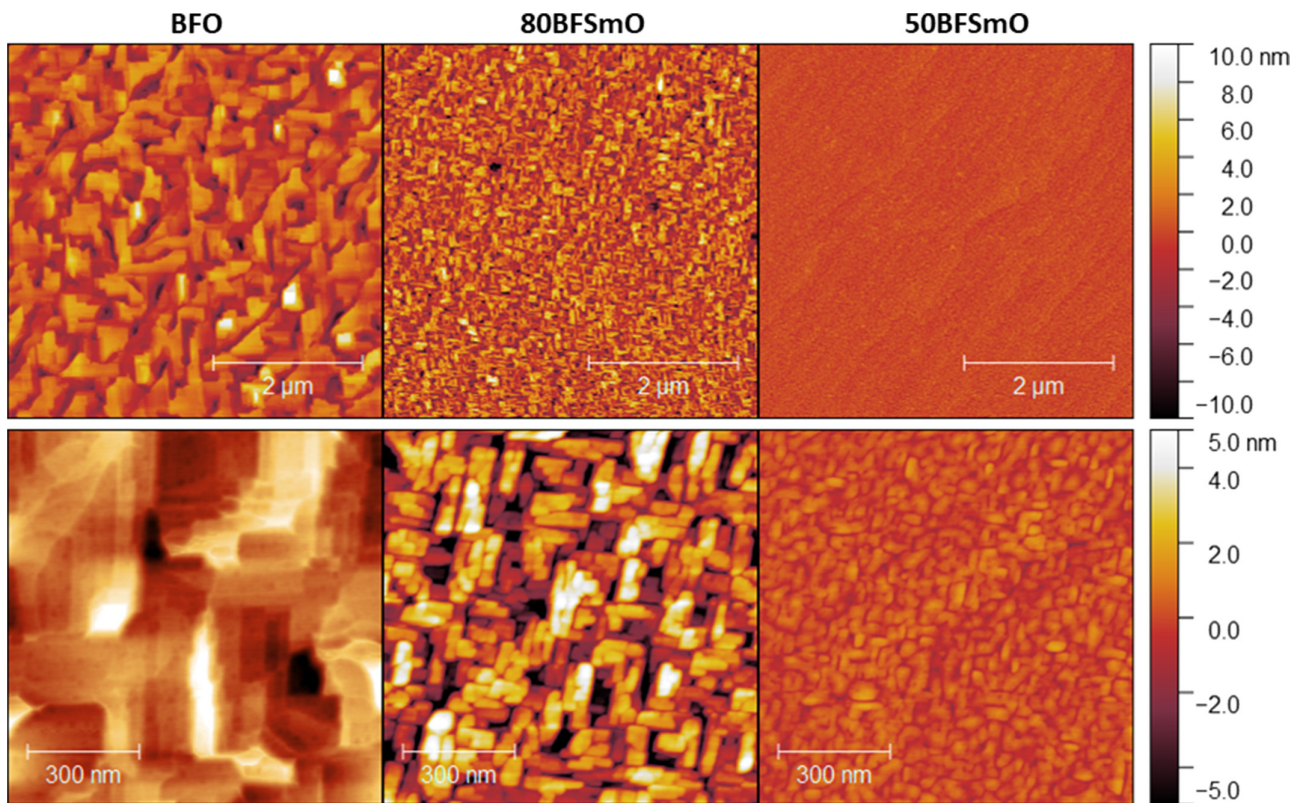


Figure 4. AFM images of BF(Sm)O thin films on STO substrate. Top row images are $5 \times 5 \mu\text{m}$, bottom row images $1 \times 1 \mu\text{m}$.

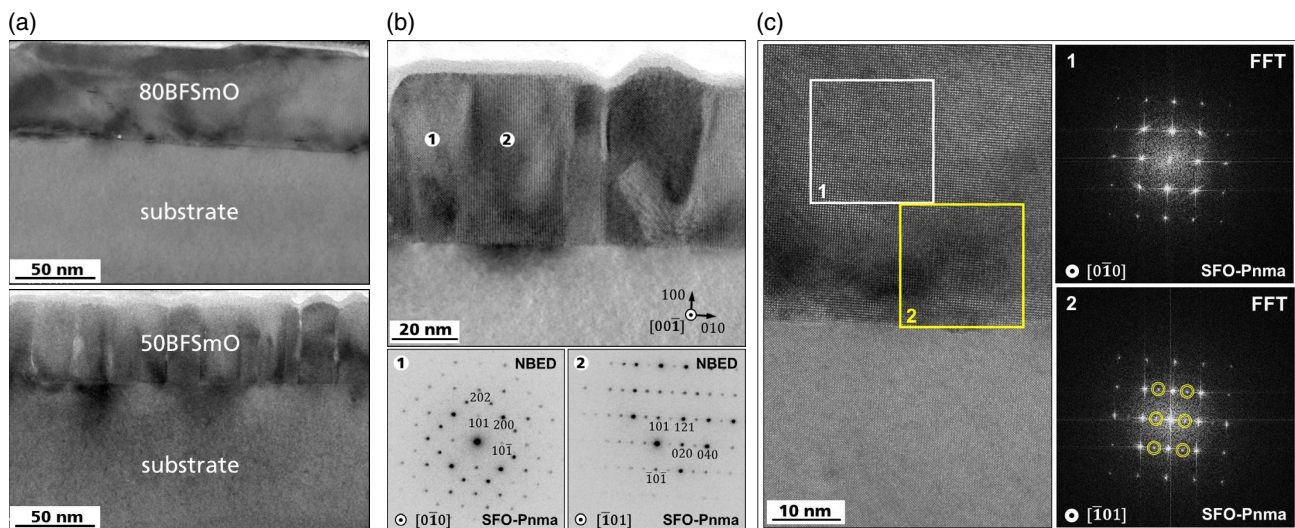


Figure 5. a) TEM results for 80BFSmO and 50BFSmO thin films on STO substrate. b) Nanobeam electron diffraction patterns from neighboring columnar regions in 50BFSmO thin film. c) HRTEM image of 80BFSmO thin film with FFT of regions 1 and 2.

To elucidate the nanochemistry of the films, energy dispersive X-ray (EDX) spectroscopy was used (not shown). However, EDX results did not show any relation between the nanocolumns and probable segregation of Bi or Sm, which implies a homogenous distribution of the two elements across the thickness of the film. Thereafter, the columns in the 50BFSmO sample were analyzed

for their respective crystallographic orientation by nanobeam electron diffraction (NBED) (Figure 5b), keeping in perspective the published data regarding the growth directions in BFSmO and SFO films on STO substrates.^[20,21] For NBED, diffraction patterns were detected by illuminating nanoregions of the sample with a nearly parallel electron-beam having a diameter of

about 3 nm. As the beam size is smaller than the diameter of the columns in the 50BFSmO film, the diffraction pattern acquired at a column includes column-specific crystallographic information. By controlled tilting in two directions, the columns were aligned in a specific relationship with the (100) plane of the substrate. The resultant NBED patterns are shown in Figure 5b. Pattern 1 and 2 were recorded from two neighboring columns (indicated in the the upper TEM image) and they clearly depict different crystallographic orientations within the columns. In particular, the diffraction patterns can be related to slightly stretched $[0\bar{1}0]$, and $[\bar{1}01]$ which are reminiscent of the observations reported in the study of SFO (space group: Pnma, $a = 0.560$ nm, $b = 0.771$ nm, $c = 0.54$ nm^[24]). Furthermore, the planes within all the investigated columns belong to (101), parallel to (100) planes of the substrate. By processing the high-resolution transmission electron microscopy (HRTEM) image in Figure 5b, the out-of-plane as well as in-plane lattice distances in both 50BFSmO-columns (indicated by 1 and 2) have been estimated to be 0.39 and 0.41 nm, respectively.

Similar values have been measured in HRTEM images of the 80BFSmO film: specifically, the lattice distances were determined to be 0.39 nm in-plane, and 0.40 nm out-of-plane. However, columnar grains do not occur in the 80BFSmO film, and rather appears to consist of a homogeneous film being locally substructured. The substructure is demonstrated in Figure 5c, which shows a HRTEM image of the film together with Fast-Fourier-Transforms (FFTs) of the film regions 1 and 2 (indicated in the TEM image). The FFT of region 2 clearly shows additional maximum peaks which indicate the local growth of $[\bar{1}01]$ -orientation similar to the one reported in SFO.

2.4. Leakage Currents

2.4.1. Capacitor Geometry

Figure 6 shows the current density (J) versus applied electric field (E) for the pure BFO and Sm-containing BFO thin films on Nb:STO. A massive reduction in leakage current, corresponding to the doping level, is evident.

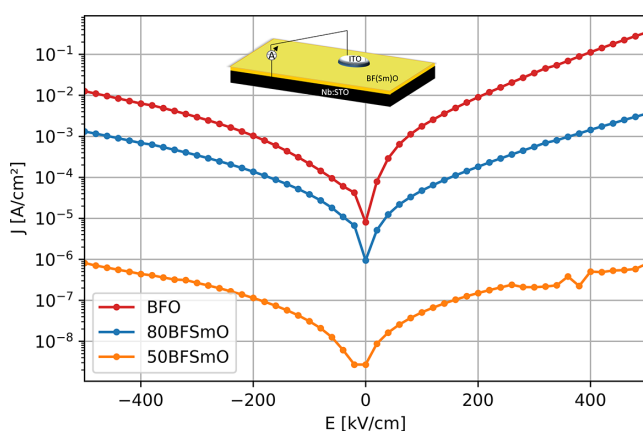


Figure 6. Leakage current density versus electric field characteristics for pure BFO and Sm-substituted BFO thin films on Nb:STO.

Interestingly, contrary results were obtained in case of ceramics, wherein much higher J have been reported in Sm-doped BFO than in pure BFO. The smaller grain size in doped-ceramics evidently translates into much large grain boundary area which was proposed to be the underlying origin for high J .^[25] However, in the case of BFSmO films with nanocolumnar architecture, results similar to the ones shown in Figure 6 were obtained,^[19] with the composite film showing J several order of magnitude lower than a pure BFO film. Similar to the morphologies presented in this work, smaller grains were also observed in the composite thin-film samples. Therefore, it was simply postulated that lowering of J , despite higher grain boundary area, can be only realized upon large reduction in oxygen vacancies. The nanocolumns apparently assist in reducing the oxygen vacancies within the BFO phase.

Although, a drastically conflicting role of largely comparable nanocolumns was demonstrated in the case of SmO–SrTiO₃ composites thin films.^[26] The interface between SmO and SrTiO₃ were measured to be much more conductive compared with the bulk of the sample and segregation of oxygen vacancies at the interface was suggested as a possible reason. The tip of conductive atomic force microscopy (CFM) was used to measure the local electrical characteristics around the interfaces. As these columns extend across the thickness of the film, the resulting macroscopic electrical measurements should result in higher values of J than previously observed,^[19] and similar to ceramics.^[25] To further investigate the origin of lower current densities in Sm-doped BFO thin films, we chose to measure the conduction properties of the samples on the nanometer scale by CFM.

2.4.2. Conductive Atomic Force Microscopy

Samples utilized for macroscopic electrical measurements were subsequently analyzed with CFM. The tip of the CFM setup was grounded during all the measurements and a bias of +4 V was applied as the tip was scanned over the surface. The samples were measured in dark conditions and under illumination. For illumination, laser of wavelength 405 nm (3.06 eV) was used which has been reported to result in a photoresponse in BFO in certain domain configurations.^[27,28] In **Figure 7a–f**, the topography and current scans recorded from pure BFO and x -BFSmO thin films under illumination are presented. The line profiles extracted from the scans are plotted in Figure 7g,h. Surprisingly, as evident from current scans, 50BFSmO exhibits much higher response than BFO and 80BFSmO, with grainy structure clearly visible. A rather low response is recorded from both BFO and 80BFSmO samples which does not increase above 3 pA. The difference in the respective conductivities is also apparent from the line profiles, with 50BFSmO more conductive in dark and illuminated conditions. In particular, the significant increase in the conductivity under illumination might be attributed to the lowering of bandgap that been reported in Sm-doped BFO ceramics.^[29] These results are completely contrary to the macroscopic measurements wherein BFO was found to be much more conductive and 50BFSmO the least.

A possible reason behind the discrepancy can be proposed upon analysis of the associated topographies. Although the

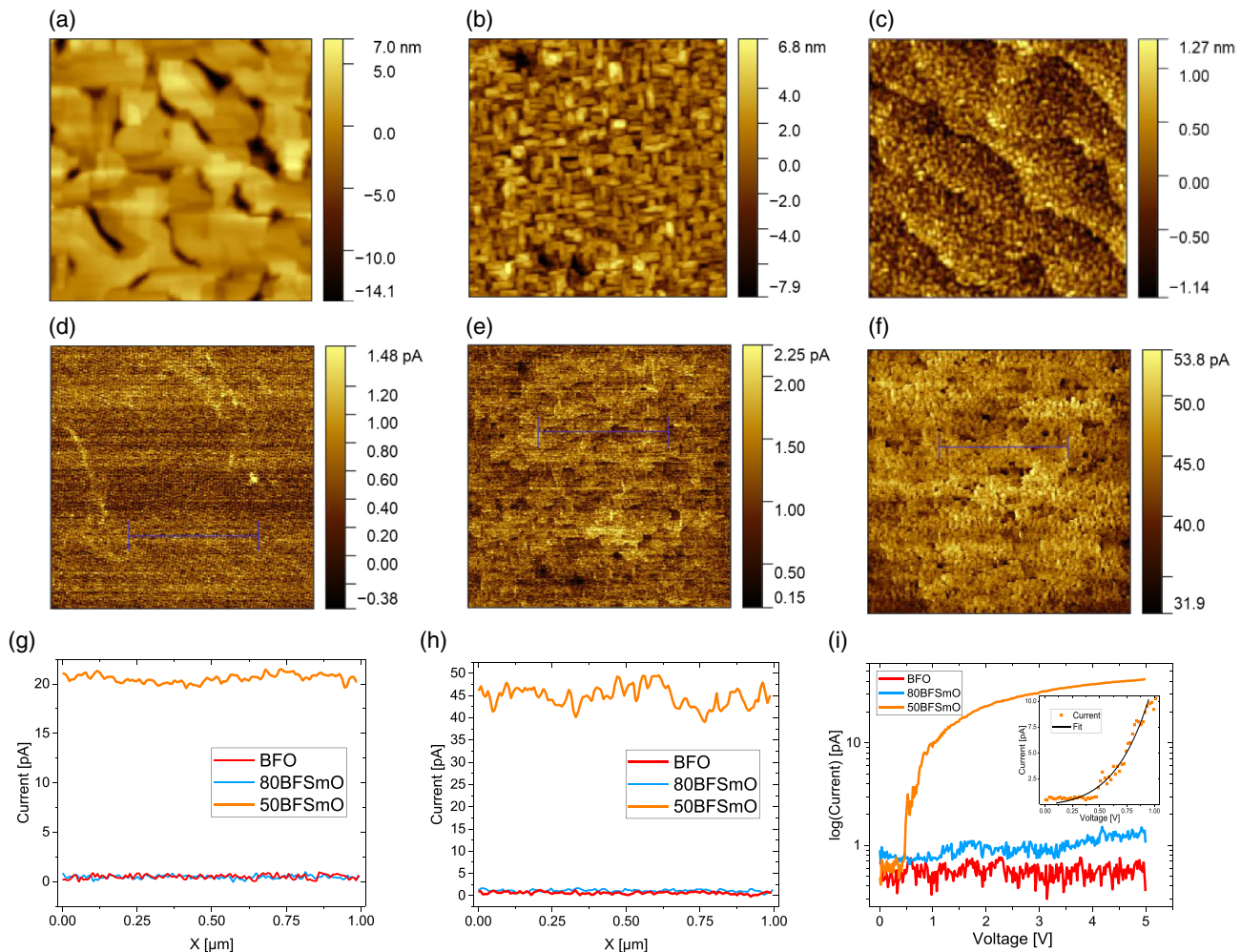


Figure 7. Conductive AFM images with $2 \times 2 \mu\text{m}$ size of BF(Sm)O thin films on Nb:STO. a,d) Present topography and current map for BFO, b,e) for 80BFSmO, c,f) for 50BFSmO thin film. Furthermore, extracted line profiles of the currents obtained in g) dark and h) illuminated conditions and local i) current–voltage characteristics are shown.

BFO surface is plagued with defects which appear as pinholes (RMS roughness of around 2.834 nm), the surface of 50BFSmO is much more smooth (RMS roughness of 0.407 nm) and homogeneous with terraces from the etched surface of the substrate still visible. Line profile across a pinhole reveals a depth of around 10 nm. However, this value is largely limited by the tip-diameter. Therefore, it can be assumed that if such defects run across the thickness of the film or partially, they will largely influence the macroscopic current response. On the contrary, a uniform current response was acquired from 50BFSmO with no drastic variations around the grain boundaries.

In conjunction, local current–voltage characteristics were measured in all the three samples and are presented in Figure 7i. In the case of pure and 80BFSmO, rather low currents were measured within the range of applied voltages. Substantial current response was recorded from 50BFSmO, which in low-voltage regimes (upto 1 V) is mostly Schottky-interface limited (inset of Figure 7i).^[30] At higher voltages, the current appears to saturate, which can be attributed to space-charge limited conduction.^[31]

3. Discussions and Conclusion

The objective of our study was to analyze the impact of samarium on the growth of BFO films. Although some results are in complete agreement with the current state of knowledge, others are distinctly contrary. The X-ray analysis clearly demonstrates a drastic reduction in the value of c_{BFO} as the content of Sm is increased, to the level it reaches 3.90 Å and matches c_{STO} . Growth on TSO substrates results in identical values of c_{BFO} as obtained in the case of STO, implying minimalistic role of in-plane strain. TEM investigations allowed us to unravel this mystery and suggest that the BF(Sm)O films comprise of orthorhombic crystals that are aligned along [100] and [110], which apparently results in lowering of macroscopic c_{BFO} value. This assessment is in full agreement with other reports wherein Sm content of upto 30% has been studied and in the case of pure SmFeO₃ films.^[12,21] However, in our study, such an assessment is valid even upto 50% Sm, wherein the crystals were observed to be ordered in a dense columnar arrangement with a rather sharp interface in-between.

Curiously, a phase separation has been often reported in 50% Sm-BFO^[7–9] which coincidentally also proceeds via the formation of alternating nanocolumns, resembling the ordering observed in this work. Another point of resemblance is the c_{BFO} which was found to be largely reduced due to the vertical strain imposed by the lattice-mismatched SmO phase. The resemblance further continues to macroscopic electrical characteristics, which qualitatively were found to be alike.^[9] But, with our nanoscopic measurements, we were able to conclude that although the pure BFO exhibit larger crystal size (implying lower grain boundary area) than 50BFSmO, the densely packed crystals in 50BFSmO ensure that bulk of the sample determines the electrical response, unlike BFO wherein the pinhole-like feature can massively dominate the electrical response. Therefore, it can be proposed that electrical response in widely reported phase-separated SmO-BFO is not determined by the in-between nanocolumns, as previously perceived, but by the orthorhombic BFSmO itself. An in-depth analysis to rule out the scenario of substitutional doping is a prerequisite, which has been inadvertently not sufficiently addressed in the work pertaining to phase separation. In addition, the 50BFSmO was found to be around two orders of magnitude more conductive than pure BFO, in contrast to previous reports.^[9]

Nevertheless, the question about the absence of the phase-separated columns in our study still remains. Considering we chose very similar deposition and cooling parameters as in the literature cited earlier and also explored a wide range of parameters available to a standard PLD system, it remains unclear what exactly triggers phase separation during PLD growth in a combination of compounds that—according to multiple preceding work and the results presented here—exhibit intermiscibility. Attention here could be brought to the ablation process and characteristics of the target. One could imagine a situation in which differences in the preparation of the target concerning the density and present phases influence the individual kinetic energies of ionic species in the plasma plume in a way that phase separation can take place in one case but not in the other. This however is only relevant if the columnar growth takes place during the actual deposition itself, with the columns originating at the film–substrate interface due to different interfacial energies of the separate phases—such as, for example, in the BFO-CoFe₂O₄ system.^[32] If, as has been retroactively theorized,^[33] the separation is due to spinodal decomposition, more attention should in turn be brought to the cooling process. The observation of phase-separated columns only in the top half of an BiMnO₃-SmO film^[34] might support this scenario. However, a cohesive study regarding the influence of cooling parameters is still missing.

The earlier discussion clearly highlights the intricacies involved in the system of rare-earth-doped BFO system. In our systematic investigation, we have explicitly unraveled a new scenario wherein 50%-doped BFO results in columnar structures, that is not driven by phase separation but by spontaneous ordering of crystals which are differently oriented, and uniformly doped. The results are also of relevance to the study of magnetic response in rare-earth-element-doped BFO wherein high concentration and uniform distribution of dopant is desired rather than phase separation.

4. Experimental Section

Single-crystals of STO (001), Nb-doped STO (001) (Nb:STO), and TSO (110) from CrysTec GmbH were used as substrates. The STO and Nb:STO substrates were prepared with an HF-based etching process and subsequent annealing step to ensure TiO₂-termination and atomically flat surface,^[35] whereas the TbScO₃ substrates were annealed at 1000° for 2 h without etch treatment.

PLD with an KrF excimer laser was used to synthesize the thin films by ablating from stoichiometric targets of Bi_{1–x}Sm_xFeO₃ with $x = 0$, $x = 0.2$ and $x = 0.5$, as well as a pure Sm₂O₃. If not specified otherwise, samples were deposited at a substrate temperature of 625° in 0.133 mbar O₂ atmosphere with a laser fluence and repetition rate of about 1 J cm^{–2} and 2 Hz, respectively. Thereafter, the samples were cooled at a controlled rate of 20 K min^{–1} in 200 mbar of oxygen environment. Thickness of around 50 nm was obtained in all the samples.

The topographies of the samples were analyzed with Park NX10 AFM. The crystal structure of the samples was analyzed with a Bruker D8 Discover X-ray diffractometer. TEM was used for an in-depth investigation on a nanometer scale. Electron-transparent lamellae were prepared in cross-section orientation by FIB using a dual-FIB/SEM FEI Versa3D (FEI Thermo Fisher Scientific Inc.). The lamellae were subjected to structural and chemical analyses using both TEM/STEM FEI TecnaiG2 F20 and TEM/STEM FEI Titan3G2 60-300 being dedicated to EDX spectroscopy by a SuperX Si-drift EDX-detector system (FEI Thermo Fisher Scientific Inc.).

Macroscopic current–voltage characteristics were measured with transparent top electrodes of indium tin oxide (ITO) that were deposited on the thin films, with Nb:STO serving as the bottom electrode. Circular electrodes of diameter 100 μm were patterned with photolithography. ITO was deposited with PLD at room temperature in 0.08 mbar O₂ atmosphere from a stoichiometric target.

For conductive AFM measurements, NSC15 platinum-coated tips from Mikromasch were used. The current acquired from the tip was fed into a low-noise current amplifier from Femto. The output from the amplifier was directed into the AFM controller to record the images of current scans.

Acknowledgements

The authors thank Prof. Kathrin Dörr and Dr. Diana Rata for the X-ray measurements, Marian Lisca for the technical support, Dr. Bodo Fuhrmann, and Dipl.-Phys. Sven Schlenker for their support with the facilities at the Interdisziplinäre Zentrum für Materialwissenschaften (IZM). Financial support from Deutsche Forschungsgemeinschaft (DFG) via Sonderforschungsbereiche (SFB) 762 (project A12), Bundesministerium für Bildung und Forschung (BMBF) Project No. 03Z22HN12, and Europäischer Fonds für regionale Entwicklung (EFRE) Sachsen-Anhalt is gratefully acknowledged.

Conflict of Interest

The authors declare no conflict of interest.

Keywords

bismuth ferrite, composite thin films, pulsed laser deposition, samarium oxide, vertically aligned nanocomposites

Received: September 30, 2019
Revised: February 13, 2020
Published online: February 28, 2020

[1] D. Sando, A. Barthélémy, M. Bibes, *J. Phys.: Condens. Matter* **2014**, *26*, 473201.

- [2] C. H. Yang, D. Kan, I. Takeuchi, V. Nagarajan, J. Seidel, *Phys. Chem. Chem. Phys.* **2012**, *14*, 15953.
- [3] R. E. Eitel, C. A. Randall, T. R. Shrout, P. W. Rehrig, W. Hackenberger, S. E. Park, *Jpn. J. Appl. Phys.* **2001**, *40*, 5999.
- [4] B. Jaffe, *Piezoelectric Ceramics*, 1st ed., Elsevier Academic Press, London **1971**.
- [5] B. Jaffe, R. S. Roth, S. Marzullo, *J. Res. Natl. Bur. Stand.* **1955**, *55*, 239.
- [6] G. L. Yuan, S. W. Or, *J. Appl. Phys.* **2006**, *100*, 024109.
- [7] J. L. MacManus-Driscoll, P. Zerrer, P. Zerrer, H. Wang, H. Wang, H. Yang, H. Yang, J. Yoon, J. Yoon, A. Fouchet, A. Fouchet, R. Yu, R. Yu, M. G. Blamire, M. G. Blamire, Q. Jia, Q. Jia, *Nat. Mater.* **2008**, *7*, 314.
- [8] Z. Bi, J. H. Lee, H. Yang, Q. Jia, J. L. MacManus-Driscoll, H. Wang, *J. Appl. Phys.* **2009**, *106*, 094309.
- [9] H. Yang, H. Wang, J. Yoon, Y. Wang, M. Jain, D. M. Feldmann, P. C. Dowden, J. L. MacManus-Driscoll, Q. Jia, *Adv. Mater.* **2009**, *21*, 3794.
- [10] H. Zheng, F. Straub, Q. Zhan, P. L. Yang, W. K. Hsieh, F. Zavaliche, Y. H. Chu, U. Dahmen, R. Ramesh, *Adv. Mater.* **2006**, *18*, 2747.
- [11] W. Zhang, R. Ramesh, J. L. MacManus-Driscoll, H. Wang, *MRS Bull.* **2015**, *40*, 736.
- [12] C. J. Cheng, D. Kan, S. H. Lim, W. R. McKenzie, P. R. Munroe, L. G. Salamanca-Riba, R. L. Withers, I. Takeuchi, V. Nagarajan, *Phys. Rev. B* **2009**, *80*, 014109.
- [13] D. Kan, L. Pálová, V. Anbusathaiah, C. J. Cheng, S. Fujino, V. Nagarajan, K. M. Rabe, I. Takeuchi, *Adv. Funct. Mater.* **2010**, *20*, 1108.
- [14] N. H. Hong, N. Thu Huong, T. Y. Kim, S. Goumri-Said, M. B. Kanoun, *J. Phys. Chem. C* **2015**, *119*, 14351.
- [15] E. Gil-gonzález, A. Perejón, P. E. Sánchez-Jiménez, M. A. Hayward, J. M. Criado, M. J. Sayagués, L. A. Pérez-Maqueda, *J. Alloys Compd.* **2017**, *711*, 541.
- [16] E. M. Choi, A. Kursumovic, O. J. Lee, J. E. Kleibecker, A. Chen, W. Zhang, H. Wang, J. L. Macmanus-Driscoll, *ACS Appl. Mater. Interfaces* **2014**, *6*, 14836.
- [17] E. M. Choi, J. E. Kleibecker, J. L. MacManus-Driscoll, *Sci. Rep.* **2017**, *7*, 43799.
- [18] S. Amoruso, C. Aruta, P. Aurino, R. Bruzzese, X. Wang, F. M. Granozio, U. S. di Uccio, *Appl. Surf. Sci.* **2012**, *258*, 9116.
- [19] H. Yang, H. Wang, H. M. Luo, D. M. Feldmann, P. C. Dowden, R. F. DePaula, Q. X. Jia, *Appl. Phys. Lett.* **2008**, *92*, 2.
- [20] D. Kan, C. J. Cheng, V. Nagarajan, I. Takeuchi, *J. Appl. Phys.* **2011**, *110*, 014106.
- [21] Z. Cheng, F. Hong, Y. Wang, K. Ozawa, H. Fujii, H. Kimura, Y. Du, X. Wang, S. Dou, *ACS Appl. Mater. Interfaces* **2014**, *6*, 7356.
- [22] H. Béa, M. Bibes, A. Barthélémy, K. Bouzouane, E. Jacquet, A. Khodan, J. P. Contour, S. Fusil, F. Wyczisk, A. Forget, D. Lebeugle, D. Colson, M. Viret, *Appl. Phys. Lett.* **2005**, *87*, 072508.
- [23] H. Yang, H. Wang, G. F. Zou, M. Jain, N. A. Suvorova, D. M. Feldmann, P. C. Dowden, R. F. DePaula, J. L. MacManus-Driscoll, A. J. Taylor, Q. X. Jia, *Appl. Phys. Lett.* **2008**, *93*, 142904.
- [24] E. N. Maslen, V. A. Streltsov, N. Ishizawa, *Acta Crystallogr., Sect. B* **1996**, *52*, 406.
- [25] K. S. Nalwa, A. Garg, *J. Appl. Phys.* **2008**, *103*, 044101.
- [26] S. Lee, A. Sangle, P. Lu, A. Chen, W. Zhang, J. S. Lee, H. Wang, Q. Jia, J. L. MacManus-Driscoll, *Adv. Mater.* **2014**, *26*, 6284.
- [27] A. Bhatnagar, A. Roy Chaudhuri, Y. Heon Kim, D. Hesse, M. Alexe, *Nat. Commun.* **2013**, *4*, 2835.
- [28] D. S. Knoche, Y. Yun, N. Ramakrishnegowda, L. Mühlhenbein, X. Li, A. Bhatnagar, *Sci. Rep.* **2019**, *9*, 13979.
- [29] C. S. Tu, C. S. Chen, P. Y. Chen, H. H. Wei, V. H. Schmidt, C. Y. Lin, J. Anthoniappen, J. M. Lee, *J. Eur. Ceram. Soc.* **2016**, *36*, 1149.
- [30] J. Seidel, P. Maksymovych, Y. Batra, A. Katan, S. Y. Yang, Q. He, A. P. Baddorf, S. V. Kalinin, C. H. Yang, J. C. Yang, Y. H. Chu, E. K. H. Salje, H. Wormeester, M. Salmeron, R. Ramesh, *Phys. Rev. Lett.* **2010**, *105*.
- [31] S. Farokhipoor, B. Noheda, *Phys. Rev. Lett.* **2011**, *107*, 127601.
- [32] H. Zheng, Q. Zhan, F. Zavaliche, M. Sherburne, F. Straub, M. P. Cruz, L. Q. Chen, U. Dahmen, R. Ramesh, *Nano Lett.* **2006**, *6*, 1401.
- [33] J. L. Macmanus-Driscoll, *Adv. Funct. Mater.* **2010**, *20*, 2035.
- [34] A. Chen, Z. Bi, Q. Jia, J. L. MacManus-Driscoll, H. Wang, *Acta Mater.* **2013**, *61*, 2783.
- [35] G. Koster, G. Rijnders, D. H. Blank, H. Rogalla, *Physica C* **2000**, *339*, 215.

Chapter 5

Part B - (Pb, Bi)(Ti, Nb)O₃:NiO system

This chapter presents the results of the work on the (Pb, Bi)(Ti, Nb)O₃:NiO nanocomposite system, as published in the following peer-reviewed articles:

[LM2] Mühlenbein, L., Singh, C. B., Lotnyk, A., Himcinschi, C., Yun, Y., Ramakrishnegowda, N., Knoche, D. S., Li, X., & Bhatnagar, A.: *Nanocomposites with Three-Dimensional Architecture and Impact on Photovoltaic Effect*. Reprinted with permission from **Nano Lett.** **2020**, **20**, **8789-8795**. Copyright 2020 American Chemical Society.

[LM3] Mühlenbein, L., Singh, C. B., Singh, A. K., Fina, I., Himcinschi, C., Lotnyk, A., & Bhatnagar, A.: *Control of Layering in Aurivillius Phase Nanocomposite Thin Films and Influence on Ferromagnetism and Optical Absorption*. Reprinted with permission from **ACS Appl. Electron. Mater.** **2022**, **4**, **1997-2004**. Copyright 2022 American Chemical Society.

[LM2] reports on the discovery of a (Pb, Bi)(Ti, Nb)O₃:NiO self-assembled nanocomposite thin film system, analyses its structure, reveals laterally resolved photoconduction, and demonstrates enhanced photovoltaic performance. [LM3] follows up on the previous report by demonstrating how the nanocomposite structure can be purposefully tuned by adjusting PLD process parameters and evaluates their respective influence on layering. This analysis sheds further light on the underlying reason for the formation of phase separation into a composite structure. In addition, it enables a comparison of differently structured nanocomposites with regard to functional properties, here ferromagnetism and optical absorption.

5.1 [LM2] Nanocomposites with Three-Dimensional Architecture and Impact on Photovoltaic Effect

Nanocomposites with Three-Dimensional Architecture and Impact on Photovoltaic Effect

Lutz Mühlenbein, Chandra Bhal Singh, Andriy Lotnyk, Cameliu Himcinschi, Yeseul Yun, Niranjana Ramakrishnegowda, David S. Knoche, Xinye Li, and Akash Bhatnagar*

Cite This: *Nano Lett.* 2020, 20, 8789–8795

Read Online

ACCESS |

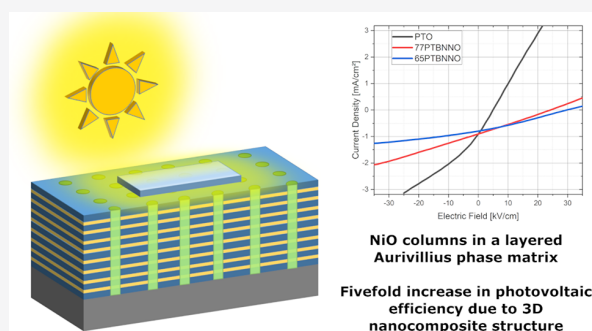
Metrics & More

Article Recommendations

Supporting Information

ABSTRACT: We demonstrate the synthesis of self-assembled three-dimensional nanocomposite thin films consisting of NiO nanocolumns in a layered Aurivillius phase matrix. The structures were grown on single-crystal SrTiO₃ substrates via pulsed laser deposition (PLD) with single ceramic (PbTiO₃)_x(BiNi_{2/3}Nb_{1/3}O₃)_{1-x} targets. The nanocolumns, which are about 10 nm in diameter each, extend over the entire film thickness of up to 225 nm. We reveal the difference in electrical conduction properties of the nanocolumns and the surrounding matrix on the nanoscale via conductive atomic force microscopy. The nanocomposite thin films exhibit improved photovoltaic performance compared to both pure PbTiO₃ and homogeneous Aurivillius phase thin films.

KEYWORDS: *Thin Film, Self-Assembly, Aurivillius Phase, Vertically Aligned Nanocomposite, Bulk Photovoltaic Effect*



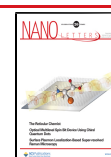
INTRODUCTION

Over the past decade, the ongoing research on self-assembled vertically aligned nanocomposites (VANs) has widened the scope of oxide thin film architecture by several new degrees of freedom, for example, the decoupling of out-of-plane strain from in-plane strain,^{1,2} the creation of large heterointerfacial areas inside the film,^{3,4} or the integration of the functional properties of two oxides into one film.^{5–7} In addition, the VAN architecture presents the lucrative opportunity to investigate the electrical properties of the heterointerfaces because of the easy access via the surface, which is not possible in the horizontal or lateral interfaces. Interestingly, the vertical interfaces have been found to be more conductive than the typical perovskite oxides (e.g., BiFeO₃, SrTiO₃),^{4,8} which are also the usual choice of the matrix. Hence the VAN architecture can be hypothesized as effective charge transport pathways in highly insulating matrices. One may therefore perceive scenarios which could greatly benefit from such an arrangement. In this regard, Aurivillius phases can be considered as a lucrative landscape. The phase is represented by a general formula Bi₂A_{m-1}B_mO_{3m+3} wherein the *m* (A_{m-1}B_mO_{3m+1})²⁻ perovskite blocks are placed intermittently with (Bi₂O₂)²⁺ bismuth oxide blocks.⁹ The Aurivillius phase has been demonstrated to be rather useful in enhancing the Curie temperature which is essential for higher-temperature operation of ferroelectric devices. The phase is remarkably tolerant to oxygen vacancies because of charge compensation character of the (Bi₂O₂)²⁺ layers and therefore has negligible fatigue-related issues.^{10,11} Consequently, the possibility of

substitutional doping has been also explored with an objective of altering the band gap and eventual application in photovoltaics.¹² However, it can be envisaged that the highly insulating character of the phase can potentially hinder the extraction of generated photocurrent. Therefore, the presence of conductive entities within the phase is highly desired to not compromise the overall insulating character while providing pathways for conduction. Similar objectives are also under extensive deliberations in perovskite-structured ferroelectrics wherein the domain walls are considered as a likely candidate for the conductive element.^{13,14} Hence, a VAN architecture comprising an Aurivillius phase with conductive columns can be proposed as a possible solution. The resultant structure will be a true three-dimensional nanocomposite. It is noteworthy to mention that previous attempts to integrate VAN with layered structures focused mostly on the combination of two distinct functional properties^{15,16} rather than using the interface as a path for conduction.

In this work, we demonstrate for the first time self-assembled growth of a VAN with a rock-salt oxide embedded in a matrix of Aurivillius phase. The choice of material is (PbTiO₃)_x(BiNi_{2/3}Nb_{1/3}O₃)_{1-x} (xPTBNNO) which was syn-

Received: September 9, 2020
Revised: November 20, 2020
Published: November 30, 2020



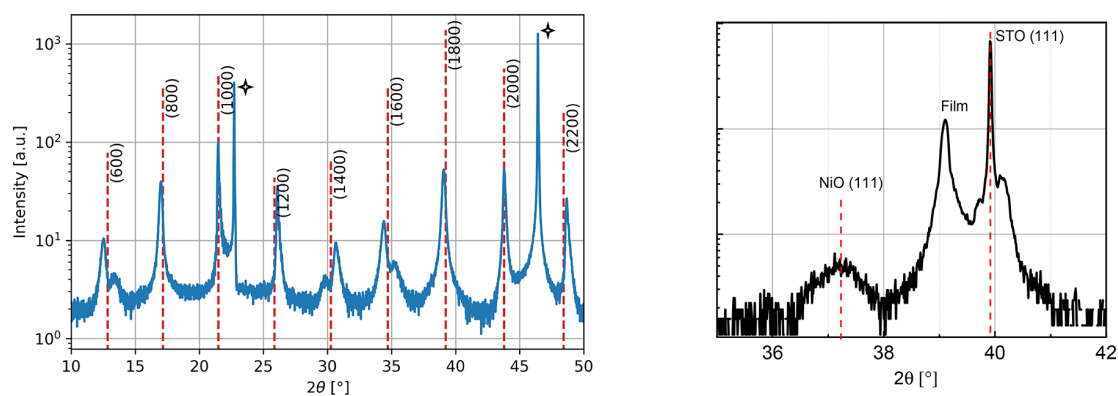


Figure 1. 2θ - ω XRD pattern of 6SPTBNNO thin film on STO (001) substrate. The annotated vertical red lines correspond to the reflections calculated for $\text{PbBi}_4\text{Ti}_4\text{O}_{15}$ along the (100) direction (normal to layering). Substrate peaks are denoted by a star symbol. Right: Asymmetric 2θ - ω XRD pattern of 6SPTBNNO thin film on STO (001) substrate around the (111) reflection of the substrate.

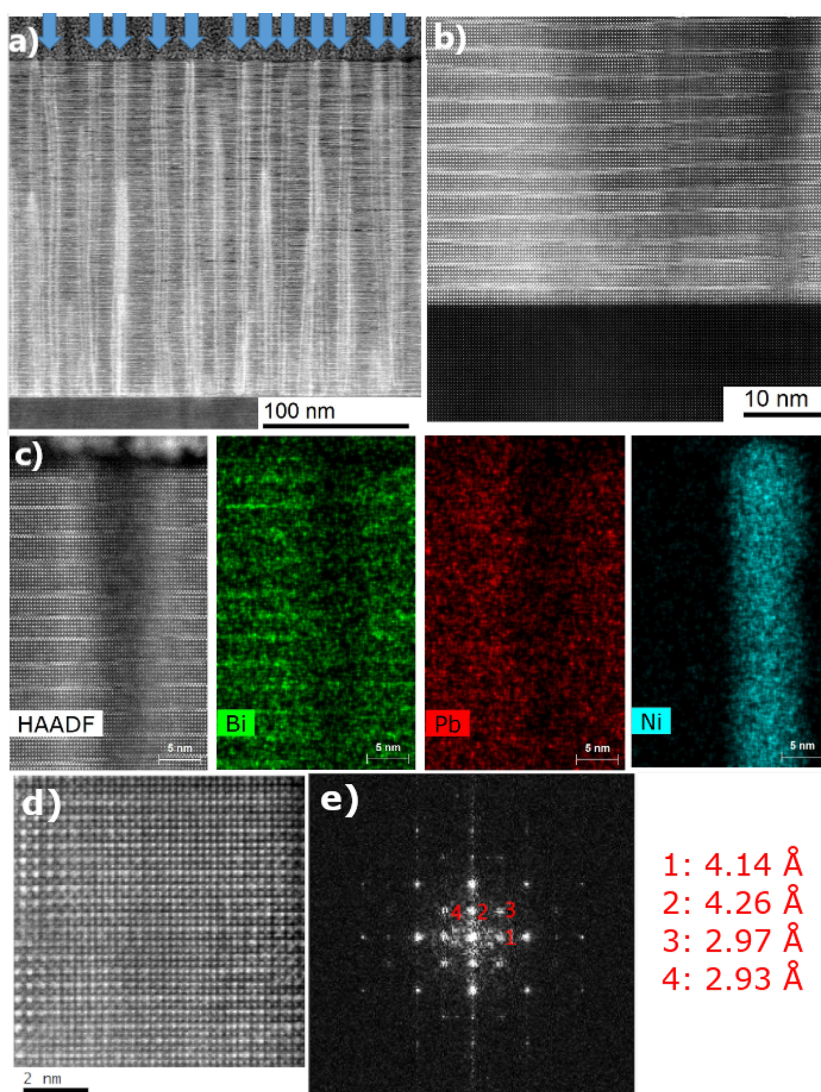


Figure 2. (a) Low-magnification ADF-STEM and (b) high-resolution HAADF-STEM images of 6SPTBNNO on STO. The micrograph in (a) shows columnar structure extending over whole film thickness (arrows), while the image in (b) represents a close-up of the substrate–film interface and layered structure. (c) EDX results of layered and columnar structure. (d) Close-up of a column. (e) FFT pattern of (d) that shows agreement with $Fm\bar{3}m$ space group under in-plane distortion.

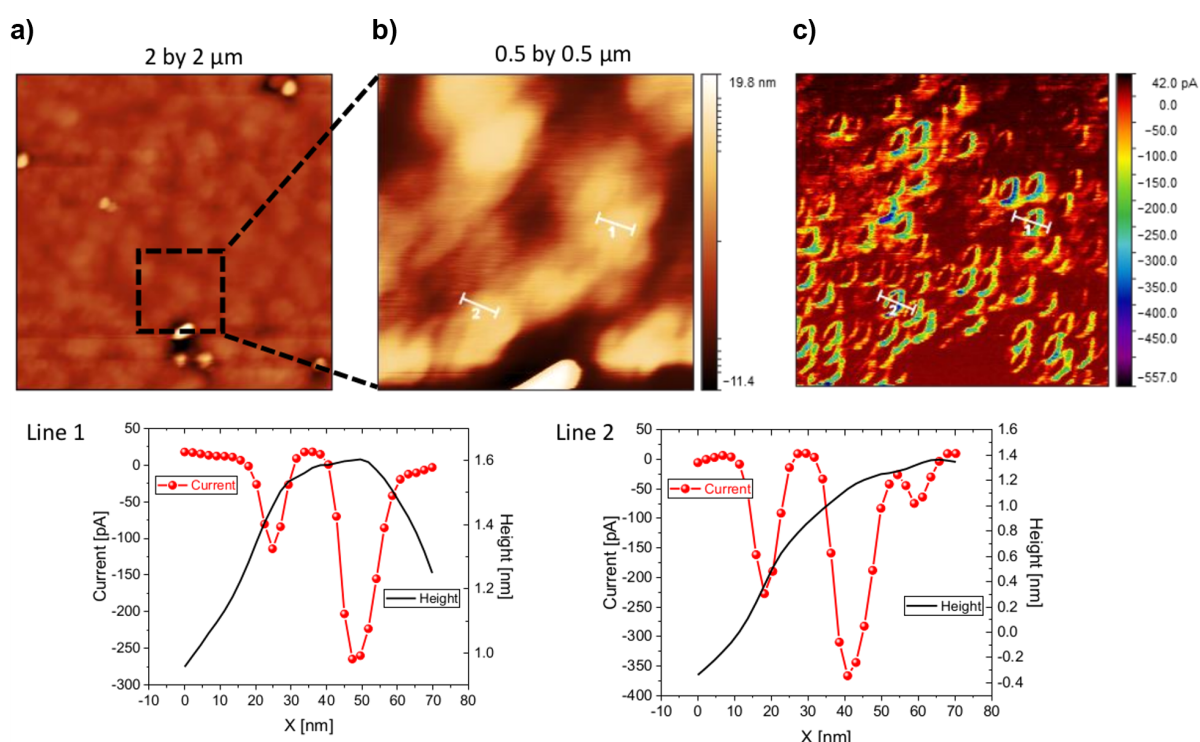


Figure 3. Photo-CFM scan of 65PTBNNO. (a) Topography, (b) extended topography and CFM. Line profile of current and height in (c) line 1 and (d) line 2.

thesized in the form of a ceramic and exhibited nonlayered perovskite phase. Thin films of different thickness were fabricated with pulsed laser deposition. Interestingly, the material crystallizes in layered Aurivillius phase with well-separated columns of NiO. The results are of great relevance considering the recently discovered applications of PTBNNO in energy conversion processes that encompass improved piezoelectric and photostriction response in conjunction with an anomalous photovoltaic effect.^{17–19} Although a strong coupling between Ni-ion and an oxygen vacancy within the perovskite unit cell is a prerequisite for a significant photovoltaic response,^{20,21} other material systems have been also proposed with similar strategies.^{12,21,22} The formation of NiO columns *a priori* rules out any substantial manifestation of such a coupling in the fabricated thin films. Nevertheless, the overall photovoltaic response in the structures was considerably enhanced (by five times) in comparison to the parent PbTiO_3 (PTO). This apparently highlights the significance of the intricate three-dimensional layered structures. The results showcase a proof-of-concept for a new subspecies of VANs that are photoelectrically active and provide the first insight into the single-crystalline thin film synthesis of such severely compounded material systems.

RESULTS AND DISCUSSIONS

Synthesis and Structural Analysis. Ceramic targets were synthesized following typical ball milling, pressing, and sintering processes. Targets with composition $(\text{PbTiO}_3)_{0.65}(\text{BiNi}_{2/3}\text{Nb}_{1/3}\text{O}_3)_{0.35}$ (65PTBNNO), $(\text{PbTiO}_3)_{0.77}(\text{BiNi}_{2/3}\text{Nb}_{1/3}\text{O}_3)_{0.23}$ (77PTBNNO), and PTO (commercial) were utilized for the fabrication of thin films with a pulsed laser deposition system. (001)-Oriented (Nb-doped) SrTiO_3 (STO) crystals were used as the substrates for

the deposition. Further details on synthesis of targets and thin film deposition are provided in the [Experimental Section](#).

Powder XRD was used for the structural analysis of ceramics whereas high-resolution diffraction in Bragg–Brentano geometry was utilized for thin films. The diffraction pattern from ceramic 65PTBNNO explicitly indicates the dominance of a homogeneous perovskite structure in close vicinity of a morphotropic boundary separating tetragonal and cubic phases (see Supporting Information, [Figure S1](#)). The pattern is largely in agreement with a previous report that focused on ceramic synthesis of identical composition.¹⁷

Surprisingly, the resultant thin films exhibit a series of peaks that are positioned symmetrically around the main perovskite peak suggesting a “superstructure” aligned along the surface normal ([Figure 1](#)). The diffraction pattern, in terms of peak positions and magnitude, is in agreement with theoretical predictions for an exemplary Aurivillius-phase material, namely $\text{PbBi}_4\text{Ti}_4\text{O}_{15}$, exhibiting a layered structure.²³ Additionally, the reflections from (600), (1400), and (1600) planes are evidently split by an equal extent (0.74° , 0.80° and 0.79° , respectively), which can be attributed to the formation of out-of-phase boundaries in the layered Aurivillius structure, originating at the atomic steps of the underlying substrate.²⁴ This signifies an epitaxial relation with the substrate and layer-by-layer growth.

However, as is shown in [Figure 1b](#), an additional peak is observed in the asymmetric 2θ – ω scan around the (111) reflection of the STO substrate, which cannot be attributed to the Aurivillius phase. Considering its position and the elements involved, the peak can be attributed to (111) NiO. In this scenario, a (002) reflection from NiO can be also perceived. However, no such peak is distinguishable in the scan presented

in Figure 1. A probable reason could be an overlap with the (2000) peak from the Aurivillius phase.

The thin film samples were investigated with TEM and EDX to gain an in-depth understanding of the structures, and the results are presented in Figure 2. The TEM micrographs explicitly showcase a matrix of layered structures with columns providing the VAN architecture. The perovskite layers sandwich the Bi-rich layers, while the columns are dominated by nickel and oxygen. The observation of columns can also explain the absence of (002)-NiO in Figure 1. The out-of-plane strain imposed by the VAN architecture can potentially align the lattice planes of the two phases which would result in identical lattice parameters. Indeed, a careful analysis of the micrographs reveals identical distances between the lattice planes of NiO columns and surrounding Aurivillius phase along [001]. The FFT image calculated from the corresponding high-resolution HAADF-STEM micrograph of the columns shown in Figure 2e is consistent with the $Fm\bar{3}m$ space group and is also in coherence with other studies detailing the structure of NiO. Further high-resolution EDX analysis (see Figure 2c) confirms that Pb is partially substituted at Bi-sites and a small amount of Nb is substituted at Ti-sites, whereas Ni is confined in the NiO columns. The lower-resolution EDX maps for all of the elements are presented in Figure S2 of the Supporting Information.

With this knowledge in hand, we are now in a position to draw some comparisons with comparable material systems. In analogy to the growth of $\text{Bi}_5\text{Ti}_3\text{FeO}_{15}$ (BTFO) on STO,¹⁵ the expected epitaxial relationship between Aurivillius phase matrix (where the axis normal to the layers is defined as [100]) and the substrate is the alignment of the [011] direction parallel to the [010] direction of STO(001). Taking the crystal structure for $\text{PbBi}_4\text{Ti}_4\text{O}_{15}$ ($a = 41.36 \text{ \AA}$, $b = 5.437 \text{ \AA}$, $c = 5.550 \text{ \AA}$), with a pseudocubic in-plane lattice parameter of $\frac{1}{2}\sqrt{b^2 + c^2} = 3.885 \text{ \AA}$, only a slight tensile strain of -0.52% is exerted in this configuration. For NiO with a lattice constant of 4.178 \AA for the fcc unit cell,²⁵ however, a large compressive strain of 7.0% must be accommodated. The feasibility of such a strain situation has been already demonstrated and analyzed in a VAN consisting of columns of MgO ($a = 4.21 \text{ \AA}$) in a $\text{La}_{0.7}\text{Sr}_{0.3}\text{MnO}_3$ ($a = 3.87 \text{ \AA}$) matrix on STO by Chen et al.² In the reported situation, however, a large lattice mismatch in the out-of-plane direction had to be additionally accommodated; in the present work, the out-of-plane lattice parameter of NiO is already close to the distance of lattice planes in the perovskite blocks of the Aurivillius phase. Therefore, it seems reasonable that effective lattice matching out-of-plane, that is, the realization of out-of-plane strain control, is realized. To further corroborate this scenario, a sample of 6SPTBNNO of similar thickness was grown on LaAlO_3 substrate which imposes a substantial compressive strain of around 2.5% along [100]. The resultant XRD from the sample (Figure S3 in the Supporting Information) is largely analogous to the one presented in Figure 1a), which evidently suggests that the growth proceeds under the influence of out-of-plane strain.

Surface Probe Measurements. The samples were further analyzed with atomic force microscopy (AFM). The surface of the 6SPTBNNO sample is rather smooth with root-mean-square roughness of 1.74 nm (Figure 3a,b). The topography does not suggest the presence of any columns which can be attributed to the low resolution of the scan as the tip diameter at 40 nm is much larger than the diameter of a column.

However, in conductive force microscopy (CFM) mode, that is, scanning with a conductive tip and reading the current while applying a constant voltage bias, concentric circular or oval-shaped conductive hot-spots appear (Figure 3c). Also, noteworthy to mention is that the CFM was conducted under laser illumination of wavelength 405 nm . As evident from the images, there is no apparent correlation between the topography (Figure 3b) and the current (Figure 3c). The current response remains minimal across the entire surface, except at the hot-spots. This also is in conformity with the highly insulating character of the Aurivillius phase which can certainly hinder carrier transport. However, keeping in perspective the observation of NiO columns in TEM, the conductive character of these columns can be considered as the underlying origin for the appearance of scattered hot-spots in CFM. The line profile (Figure 3d,e) across the hot-spots indicates extremely low currents within the concentric ring and outside, whereas currents in excess of 200 pA are along the border of the ring where the existence of columns can be envisaged. Consequently, the ratio between the currents acquired from the conductive and insulating regions can be estimated to be around 100 and in some instances even higher. Indeed, these numbers can be considered remarkable when compared with studies involving domain walls in ferroelectrics. In the case of PZT, much lower ratios were observed from artificially written *c*- and as grown *a*-domain walls under similar bias conditions.^{26,27} Ratios comparable to this study are only reported from systems with an ordered array of *a*-domain walls obtained via thermal treatment.²⁸ In BiFeO_3 films exhibiting an ordered array of 71° domain walls, ratios ranging from 1.5 to 2 were observed under light.²⁹

Although, it will be rather ambitious to comment on the intrinsic or extrinsic character of the conductivity of these columns. As a matter of fact, NiO is a Mott-Hubbard insulator and the inherent conduction has been found to be either thermally activated or mediated via polaron hopping.³⁰ Another possible explanation involves agglomeration of oxygen vacancies at the columns and has been demonstrated in the case of VAN system comprising Sm_2O_3 columns embedded in a matrix of insulating SrTiO_3 .⁸ Nevertheless, the columnar nanostructures could serve as efficient charge transport pathways, leading to improved charge separation. Therefore, an impact on the macroscopic measurements can be also perceived.

Macroscopic Photoelectrical Measurements. These measurements were conducted under 1.5 AM solar irradiation with indium tin oxide (ITO) and Nb:SrTiO₃ as the top and bottom electrode, respectively. The resultant current–voltage characteristics are presented in Figure 4 and the extracted photovoltaic characteristics from different heterostructures are listed in Table 1. In addition, the optical absorption was analyzed which revealed a slightly higher absorption in the layered structures in comparison to PTO (Figure S4 in the Supporting Information).

The results show a drastic enhancement in the photo-generated field in the composite samples, whereas the short circuit current density is only slightly reduced. Consequently, an overall 5-fold increment in the photogenerated power at the maximum power point is calculated in ITO/6SPTBNNO/Nb:STO upon comparison with ITO/PTO/Nb:STO. In the pioneering studies on the bulk photovoltaic effect by Fridkin et al.,³¹ it was shown that, unlike in comparable perovskite ferroelectrics like KNbO_3 or BaTiO_3 , high open circuit voltages

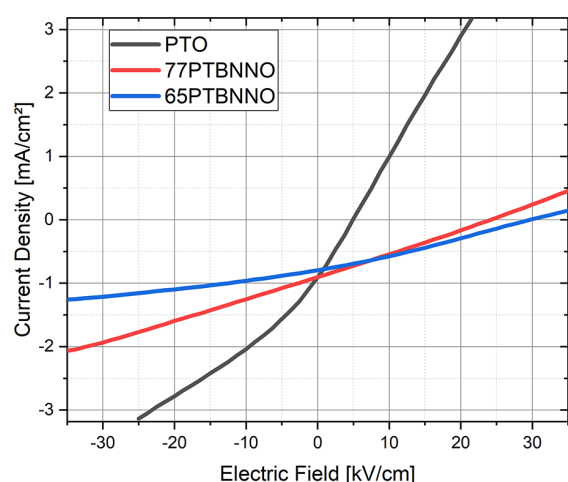


Figure 4. I – V characteristics of ITO/PT(BNN)O/Nb:STO heterostructures measured under 100 mW cm^{-2} solar simulator illumination.

Table 1. Short Circuit Current J_{SC} , Photogenerated Field E_{ph} , and Power Per Area at the Maximum Power Point P_m extracted from Measurement Shown in Figure 4

	J_{SC} (mA cm^{-2})	E_{ph} (kV cm^{-1})	P_m ($\mu\text{W cm}^{-2}$)
PTO	0.907	4.9	23
77PTBNNNO	0.904	24.2	113
65PTBNNNO	0.796	29.7	131

are unattainable in PTO due to the high intrinsic photoconductivity. In comparison, the layered structures are clearly much more (photo)resistive which evidently results in higher photogenerated fields. This interpretation is further bolstered by the results of ac dielectric measurements provided in the Supporting Information, Figure S5. The increase in the loss tangent under illumination is significantly higher for the PTO film than for the 65PTBNNNO film. Furthermore the open circuit voltages in the layered structure approach saturation as the intensity of light is gradually scaled up (see Supporting Information, Figure S6). Such dependency of the open circuit voltage on the photoconductivity and saturation with light intensity strongly suggests a symmetry-driven photovoltaic effect,^{32,33} often referred to as bulk photovoltaic effect.

In addition, the PTBNNNO nanocomposite thin films also outperform pure Aurivillius phase thin films (without VAN structure), like $\text{Bi}_4\text{Ti}_3\text{O}_{12}$ or $\text{Bi}_5\text{FeTi}_3\text{O}_{15}$ in both photocurrent and photogenerated field,^{34,35} which highlights the positive and dominant impact of the NiO VAN on the overall charge transport.

Measurements conducted in planar geometries highlight this aspect as well (Figure S7 in the Supporting Information). The films appeared to be much more resistive, despite larger electric fields, with no measurable photovoltaic effect. This is in stark contrast to the results from out-of-plane geometry and explicitly showcases the importance of the anisotropic VAN arrangement.

CONCLUSION AND OUTLOOK

In this work, we have successfully demonstrated the growth of a three-dimensional nanocomposite possessing an Aurivillius phase nanolayered structure with vertically aligned conductive columns. The nanocomposite can be considered self-

assembled because neither the layered structure, nor the binary oxide of the columns, were detected in the ceramic target of PTBNNNO. Although the XRD investigations suggest a similarity with the Aurivillius phase material $\text{PbBi}_4\text{Ti}_4\text{O}_{15}$, a more general composition can be tentatively proposed to take into account the presence of Nb and Ni ions: (Pb,Nb)-doped bismuth titanate with intergrowth of NiO columns. Bismuth titanate ($\text{Bi}_4\text{Ti}_3\text{O}_{12}$) itself is a well-known Aurivillius phase and has been demonstrated to accommodate Nb- and Pb-ions.³⁶ The columns were found to be much more conductive than the surrounding Aurivillius phase by around two orders of magnitude. The observation is reminiscent of the conductive domain walls in ferroelectric oxides. The photoelectrical characteristics of the composites were investigated under 1.5 AM. Upon comparison with parent PTO, higher photogenerated fields were observed in the composites without a significant drop in the photocurrent, which apparently translates into higher photogenerated power. Additionally, the photoperformance in the composites is also remarkably improved compared to any of the previously studied Aurivillius systems, highlighting the role of conductive columns in efficient charge transport.

The results are also of significance for the realization of free-standing layers. The composites were found to be under the influence of vertical strain imposed by the Aurivillius phase, rather than the typical substrate-induced horizontal strain. This attribute makes them an ideal candidate for exfoliation techniques and subsequent integration with other devices.

However, it must be acknowledged that the underlying mechanism for the crystallization of such intricately linked three-dimensional architecture needs further understanding and investigations. Nevertheless, few critical observations are worthy to be mentioned. The good agreement of the planar XRD result with the $\text{PbBi}_4\text{Ti}_4\text{O}_{15}$ theory prediction might suggest that the Pb/Bi ratio in the eventual structure is much different from that in the target. A probable reason could be the volatile character of both the elements during ablation with the laser.^{37,38} The prevalent deposition parameters may prefer deposition of Bi, leading to an Aurivillius phase. An insolubility of Ni with the resultant Aurivillius phase may drive the Ni to form a separate phase, possibly *via* spinodal decomposition.³⁹

Or, conversely, a comparably low interfacial energy with the substrate surface can lead to an aggregation of Ni ions and subsequent nucleation and growth of the NiO columnar structure,³⁹ while the rest of the material is left with too many A-site ions, consequently forming the Aurivillius phase matrix as the most stable possibility, re-evaporating Pb.

EXPERIMENTAL SECTION

Ceramic Target Preparation. Details on the preparation of the ceramic targets and powder X-ray diffraction analysis can be found in the Supporting Information.

Thin Film Synthesis. Single-crystals of SrTiO_3 (001) and Nb-doped SrTiO_3 (001) purchased from CrysTec GmbH were used as substrates. Prior to deposition, the substrates were prepared with a HF-based etching process and subsequent annealing step to ensure the TiO_2 -termination and atomically flat surface.⁴⁰

PLD with an KrF excimer laser was used to synthesize the thin films by ablating from the ceramic targets. The samples were deposited at a substrate temperature of 625°C in 0.4 mbar atmosphere consisting of O_2 and Ar at equal partial pressure with a laser fluence and repetition rate of 0.85 J cm^{-2}

and 10 Hz, respectively. Thereafter, the samples were cooled at a controlled rate of 20 K min^{-1} in a 200 mbar oxygen environment. A film thickness of around 225 nm was obtained for 5000 laser pulses at a substrate-to-target distance of 60 mm.

Sample Analysis. The crystal structure of the samples was analyzed with a Bruker D8 Discover X-ray diffractometer.

Details on TEM and EDX measurements can be found in the [Supporting Information](#).

The AFM and CFM investigations were conducted with a conductive NSC-15 tip from MikroMasch coated with platinum. The scans for CFM were performed with a constant bias of -9 V applied to the sample and under the light of wavelength 405 nm with the power of around 9 mW.

Transparent top electrodes of indium tin oxide (ITO) were deposited on the thin films with Nb:STO serving as the bottom electrode. Circular electrodes with a diameter of $100 \mu\text{m}$ were patterned with photolithography. ITO was deposited with PLD at room temperature in 0.08 mbar O_2 atmosphere from a target with weight percentages of 95 and 5 for In_2O_3 and SnO_2 , respectively. For the PV measurement, samples were illuminated with a xenon arc lamp solar simulator (Abet Technologies). Voltage application and current measurement were performed by a Keithley 6517B Electrometer.

■ ASSOCIATED CONTENT

SI Supporting Information

The Supporting Information is available free of charge at <https://pubs.acs.org/doi/10.1021/acs.nanolett.0c03654>.

Supporting figures (PDF)

■ AUTHOR INFORMATION

Corresponding Author

Akash Bhatnagar – Zentrum für Innovationskompetenz SiLi-nano and Institute of Physics, Martin Luther Universität Halle-Wittenberg, Halle (Saale) 06120, Germany;

orcid.org/0000-0001-6212-4576;

Email: akash.bhatnagar@physik.uni-halle.de

Authors

Lutz Mühlhain – Zentrum für Innovationskompetenz SiLi-nano and Institute of Physics, Martin Luther Universität Halle-Wittenberg, Halle (Saale) 06120, Germany

Chandra Bhal Singh – Indian Institute of Technology, Banaras Hindu University, Varanasi 221005, India

Andriy Lotnyk – Leibniz Institute of Surface Engineering, Leipzig 04318, Germany; Laboratory of Infrared Materials and Devices, The Research Institute of Advanced Technologies, Ningbo University, Ningbo 315211, China;

orcid.org/0000-0002-0000-9334

Cameliu Himcinschi – Institute of Theoretical Physics, TU Bergakademie Freiberg, Freiberg D-09596, Germany

Yeseul Yun – Zentrum für Innovationskompetenz SiLi-nano and Institute of Physics, Martin Luther Universität Halle-Wittenberg, Halle (Saale) 06120, Germany

Niranjan Ramakrishnegowda – Zentrum für Innovationskompetenz SiLi-nano and Institute of Physics, Martin Luther Universität Halle-Wittenberg, Halle (Saale) 06120, Germany

David S. Knoch – Zentrum für Innovationskompetenz SiLi-nano and Institute of Physics, Martin Luther Universität Halle-Wittenberg, Halle (Saale) 06120, Germany

Xinye Li – Zentrum für Innovationskompetenz SiLi-nano and Institute of Physics, Martin Luther Universität Halle-Wittenberg, Halle (Saale) 06120, Germany

Complete contact information is available at: <https://pubs.acs.org/10.1021/acs.nanolett.0c03654>

Notes

The authors declare no competing financial interest.

■ ACKNOWLEDGMENTS

The authors thank K. Dörr and D. Rata for the X-ray measurements, M. Lisca for the technical support, B. Fuhrmann and S. Schlenker for their support with the facilities at the Interdisziplinäre Zentrum für Materialwissenschaften (IZM). Financial support from Deutsche Forschungsgemeinschaft (DFG) via Sonderforschungsbereiche (SFB) 762 (project A12), Bundesministerium für Bildung und Forschung (BMBF) Project No. 03Z22HN12, and Europäischer Fonds für regionale Entwicklung (EFRE) Sachsen-Anhalt is gratefully acknowledged.

■ REFERENCES

- (1) MacManus-Driscoll, J. L.; Zerrer, P.; Wang, H.; Yang, H.; Yoon, J.; Fouchet, A.; Yu, R.; Blamire, M. G.; Jia, Q. Strain control and spontaneous phase ordering in vertical nanocomposite heteroepitaxial thin films. *Nat. Mater.* **2008**, *7*, 314–320.
- (2) Chen, A.; et al. Role of Scaffold Network in Controlling Strain and Functionalities of Nanocomposite Films. *Science Advances* **2016**, *2*, No. e1600245.
- (3) Hsieh, Y.-H.; Liou, J.-M.; Huang, B.-C.; Liang, C.-W.; He, Q.; Zhan, Q.; Chiu, Y.-P.; Chen, Y.-C.; Chu, Y.-H. Local Conduction at the BiFeO_3 - CoFe_2O_4 Tubular Oxide Interface. *Adv. Mater.* **2012**, *24*, 4564–4568.
- (4) Hsieh, Y.-H.; Strelcov, E.; Liou, J.-M.; Shen, C.-Y.; Chen, Y.-C.; Kalinin, S. V.; Chu, Y.-H. Electrical Modulation of the Local Conduction at Oxide Tubular Interfaces. *ACS Nano* **2013**, *7*, 8627–8633.
- (5) Zhang, W.; Chen, A.; Jian, J.; Zhu, Y.; Chen, L.; Lu, P.; Jia, Q.; MacManus-Driscoll, J. L.; Zhang, X.; Wang, H. Strong perpendicular exchange bias in epitaxial $\text{La}_{0.7}\text{Sr}_{0.3}\text{MnO}_3$: BiFeO_3 nanocomposite films through vertical interfacial coupling. *Nanoscale* **2015**, *7*, 13808–13815.
- (6) Huang, J.; MacManus-Driscoll, J. L.; Wang, H. New Epitaxy Paradigm in Epitaxial Self-Assembled Oxide Vertically Aligned Nanocomposite Thin Films. *J. Mater. Res.* **2017**, *32*, 4054–4066.
- (7) Gao, X.; Zhang, D.; Wang, X.; Jian, J.; He, Z.; Dou, H.; Wang, H. Vertically aligned nanocomposite $(\text{BaTiO}_3)_{0.8}:(\text{La}_{0.7}\text{Sr}_{0.3}\text{MnO}_3)_{0.2}$ thin films with anisotropic multifunctionalities. *Nanoscale Advances* **2020**, *2*, 3276–3283.
- (8) Lee, S.; Sangle, A.; Lu, P.; Chen, A.; Zhang, W.; Lee, J. S.; Wang, H.; Jia, Q.; MacManus-Driscoll, J. L. Novel Electroforming-Free Nanoscaffold Memristor with Very High Uniformity, Tunability, and Density. *Adv. Mater.* **2014**, *26*, 6284–6289.
- (9) Kendall, K. R.; Navas, C.; Thomas, J. K.; Zur Loye, H. C. Recent Developments in Oxide Ion Conductors: Aurivillius Phases. *Chem. Mater.* **1996**, *8*, 642–649.
- (10) Park, B. H.; Kang, B. S.; Bu, S. D.; Noh, T. W.; Lee, J.; Jo, W. Lanthanum-Substituted Bismuth Titanate for use in Non-Volatile Memories. *Nature* **1999**, *401*, 682–684.
- (11) Campanini, M.; Trassin, M.; Ederer, C.; Erni, R.; Rossell, M. D. Buried In-Plane Ferroelectric Domains in Fe-Doped Single-Crystalline Aurivillius Thin Films. *ACS Applied Electronic Materials* **2019**, *1*, 1019–1028.
- (12) Choi, W. S.; Chisholm, M. F.; Singh, D. J.; Choi, T.; Jellison, G. E.; Lee, H. N. Wide Bandgap Tunability in Complex Transition Metal Oxides by Site-Specific Substitution. *Nat. Commun.* **2012**, *3*, 689.

- (13) Guyonnet, J.; Gaponenko, I.; Gariglio, S.; Paruch, P. Conduction at Domain Walls in Insulating $\text{Pb}(\text{Zr}_{0.2}\text{Ti}_{0.8})\text{O}_3$ Thin Films. *Adv. Mater.* **2011**, *23*, 5377–5382.
- (14) Seidel, J.; et al. Conduction at Domain Walls in Oxide Multiferroics. *Nat. Mater.* **2009**, *8*, 229–234.
- (15) Imai, A.; Cheng, X.; Xin, H. L.; Eliseev, E. A.; Morozovska, A. N.; Kalinin, S. V.; Takahashi, R.; Lippmaa, M.; Matsumoto, Y.; Nagarajan, V. Epitaxial $\text{Bi}_3\text{Ti}_3\text{FeO}_{15}$ - CoFe_2O_4 Pillar-Matrix Multiferroic Nanostructures. *ACS Nano* **2013**, *7*, 11079–11086.
- (16) Wang, H.; Li, L.; Huang, J.; Gao, X.; Sun, X.; Wang, H. Multiferroic vertically aligned nanocomposite with CoFe_2O_4 nanorods embedded in layered Bi_2WO_6 matrix. *Mater. Res. Lett.* **2019**, *7*, 418–425.
- (17) Zhang, S.; Stringer, C.; Xia, R.; Choi, S. M.; Randall, C. A.; Shrout, T. R. Investigation of Bismuth-Based Perovskite System: $(1-x)\text{Bi}(\text{Ni}_{2/3}\text{Nb}_{1/3})\text{O}_3 - x\text{PbTiO}_3$. *J. Appl. Phys.* **2005**, *98*, 96–101.
- (18) Liu, H.; Chen, J.; Ren, Y.; Zhang, L.; Pan, Z.; Fan, L.; Xing, X. Large Photovoltage and Controllable Photovoltaic Effect in $\text{PbTiO}_3 - \text{Bi}(\text{Ni}_{2/3+x}\text{Nb}_{1/3-x})\text{O}_{3-d}$ Ferroelectrics. *Advanced Electronic Materials* **2015**, *1*, 1400051.
- (19) Li, X.; Chen, C.; Zhang, F.; Huang, X.; Yi, Z. Large Visible-Light-Driven Photostriction in $\text{Bi}(\text{Ni}_{2/3}\text{Nb}_{1/3})\text{O}_3 - \text{PbTiO}_3$ Ferroelectrics. *APL Mater.* **2020**, *8*, 061111.
- (20) Bennett, J. W.; Grinberg, I.; Rappe, A. M. New Highly Polar Semiconductor Ferroelectrics through d8 Cation-O Vacancy Substitution into PbTiO_3 : A Theoretical Study. *J. Am. Chem. Soc.* **2008**, *130*, 17409–17412.
- (21) Grinberg, I.; West, D. V.; Torres, M.; Gou, G.; Stein, D. M.; Wu, L.; Chen, G.; Gallo, E. M.; Akbashev, A. R.; Davies, P. K.; Spanier, J. E.; Rappe, A. M. Perovskite Oxides for Visible-Light-Absorbing Ferroelectric and Photovoltaic Materials. *Nature* **2013**, *503*, 509–512.
- (22) Park, J.; Won, S. S.; Ahn, C. W.; Kim, I. W. Ferroelectric Photocurrent Effect in Polycrystalline Lead-Free $(\text{K}_{0.5}\text{Na}_{0.5})-(\text{Mn}_{0.005}\text{Nb}_{0.995})\text{O}_3$ Thin Film. *J. Am. Ceram. Soc.* **2013**, *96*, 146–150.
- (23) Reznichenko, L.; Razumovskaya, O.; Shilkina, L.; Dergunova, N. Correlating the Curie Temperature of Mixed Bismuth Oxides to the Crystalchemical Parameters of Constituent Ions. *Inorg. Mater.* **1996**, *32*, 423–429.
- (24) Zurbuchen, M. A.; Tian, W.; Pan, X. Q.; Fong, D.; Streiffer, S. K.; Hawley, M. E.; Lettieri, J.; Jia, Y.; Asayama, G.; Fulk, S. J.; Comstock, D. J.; Knapp, S.; Carim, A. H.; Schlom, D. G. Morphology, Structure, and Nucleation of Out-Of-Phase Boundaries (OPBs) in Epitaxial Films of Layered Oxides. *J. Mater. Res.* **2007**, *22*, 1439–1471.
- (25) Sasaki, S.; Fujino, K.; Takeuchi, Y. X-Ray Determination of Electron-Density Distributions in Oxides, MgO, MnO, CoO, and NiO, and Atomic Scattering Factors of their Constituent Atoms. *Proc. Jpn. Acad., Ser. B* **1979**, *55*, 43–48.
- (26) Stolichnov, I.; Feigl, L.; McGilly, L. J.; Sluka, T.; Wei, X.-K.; Colla, E.; Crassous, A.; Shapovalov, K.; Yudin, P.; Tagantsev, A. K.; Setter, N. Bent Ferroelectric Domain Walls as Reconfigurable Metallic-Like Channels. *Nano Lett.* **2015**, *15*, 8049–8055.
- (27) Gaponenko, I.; Tückmantel, P.; Karthik, J.; Martin, L. W.; Paruch, P. Towards Reversible Control of Domain Wall Conduction in $\text{Pb}(\text{Zr}_{0.2}\text{Ti}_{0.8})\text{O}_3$ Thin Films. *Appl. Phys. Lett.* **2015**, *106*, 162902.
- (28) Feigl, L.; Yudin, P.; Stolichnov, I.; Sluka, T.; Shapovalov, K.; Mtebwa, M.; Sandu, C. S.; Wei, X.-K.; Tagantsev, A. K.; Setter, N. Controlled Stripes of Ultrafine Ferroelectric Domains. *Nat. Commun.* **2014**, *5*, 4677.
- (29) Yang, M.-M.; Bhatnagar, A.; Luo, Z.-D.; Alexe, M. Enhancement of Local Photovoltaic Current at Ferroelectric Domain Walls in BiFeO_3 . *Sci. Rep.* **2017**, *7*, 43070.
- (30) Lunkenheimer, P.; Loidl, A.; Ottermann, C. R.; Bange, K. Correlated Barrier Hopping in NiO Films. *Phys. Rev. B: Condens. Matter Mater. Phys.* **1991**, *44*, 5927–5930.
- (31) Fridkin, V. M.; Popov, B. N.; Kuznetsov, V. A.; Barsukova, M. L. The Photoconductivity and Photovoltaic Effect in PbTiO_3 . *Ferroelectrics* **1978**, *19*, 109–110.
- (32) Gunter, P. Photovoltages, Photocurrents and Photorefractive Effects in KNbO_3 :Fe. *Ferroelectrics* **1978**, *22*, 671–674.
- (33) Yang, M.-M.; Kim, D. J.; Alexe, M. Flexo-photovoltaic effect. *Science* **2018**, *360*, 904–907.
- (34) Zhang, Y.; Zheng, H.; Zhang, J.; Yuan, G.; Gao, W.; Gu, Y.; Diao, C.; Liu, Y.; Zhang, W. Photovoltaic Effects in $\text{Bi}_4\text{Ti}_3\text{O}_{12}$ Thin Film Prepared by a Sol-Gel Method. *Mater. Lett.* **2014**, *125*, 25–27.
- (35) Zhu, M.; Zheng, H.; Zhang, J.; Yuan, G.; Wang, K.; Yue, G.; Li, F.; Chen, Y.; Wu, M.; Zhang, W. Polarization Dependent Ferroelectric Photovoltaic Effects in BFTO/CuO Thin Films. *Appl. Phys. Lett.* **2017**, *111*, 032901.
- (36) Frit, B.; Mercurio, J. The crystal chemistry and dielectric properties of the Aurivillius family of complex bismuth oxides with perovskite-like layered structures. *J. Alloys Compd.* **1992**, *188*, 27–35.
- (37) Christen, H. M.; Eres, G. Recent Advances in Pulsed-Laser Deposition of Complex Oxides. *J. Phys.: Condens. Matter* **2008**, *20*, 264005.
- (38) Schou, J. Physical Aspects of the Pulsed Laser Deposition Technique: The Stoichiometric Transfer of Material from Target to Film. *Appl. Surf. Sci.* **2009**, *255*, 5191–5198.
- (39) MacManus-Driscoll, J. L. Self-Assembled Heteroepitaxial Oxide Nanocomposite Thin Film Structures: Designing Interface-Induced Functionality in Electronic Materials. *Adv. Funct. Mater.* **2010**, *20*, 2035–2045.
- (40) Koster, G.; Rijnders, G.; Blank, D. H.; Rogalla, H. Surface Morphology Determined by (001) Single-Crystal SrTiO_3 Termination. *Phys. C* **2000**, *339*, 215–230.

Supporting Information:

Nanocomposites with three-dimensional architecture and impact on photovoltaic effect

Lutz Mühlenbein,^{†,‡} Chandra Bhal Singh,[¶] Andriy Lotnyk,^{§,||} Cameliu Himcinschi,[⊥] Yeseul Yun,^{†,‡} Niranjan Ramakrishnegowda,^{†,‡} David S. Knoche,^{†,‡}
Xinye Li,^{†,‡} and Akash Bhatnagar^{*,†,‡}

[†]*Zentrum für Innovationskompetenz SiLi-nano, Martin Luther Universität*

Halle-Wittenberg, Halle (Saale), Germany

[‡]*Institute of Physics, Martin Luther Universität Halle-Wittenberg, Halle (Saale), Germany*

[¶]*Indian Institute of Technology (Banaras Hindu University), Varanasi, India*

[§]*Leibniz Institute of Surface Engineering, Leipzig, Germany*

^{||}*Laboratory of Infrared Materials and Devices, The Research Institute of Advanced Technologies, Ningbo University, Ningbo, China*

[⊥]*Institute of Theoretical Physics, TU Bergakademie Freiberg, Freiberg, Germany*

E-mail: akash.bhatnagar@physik.uni-halle.de

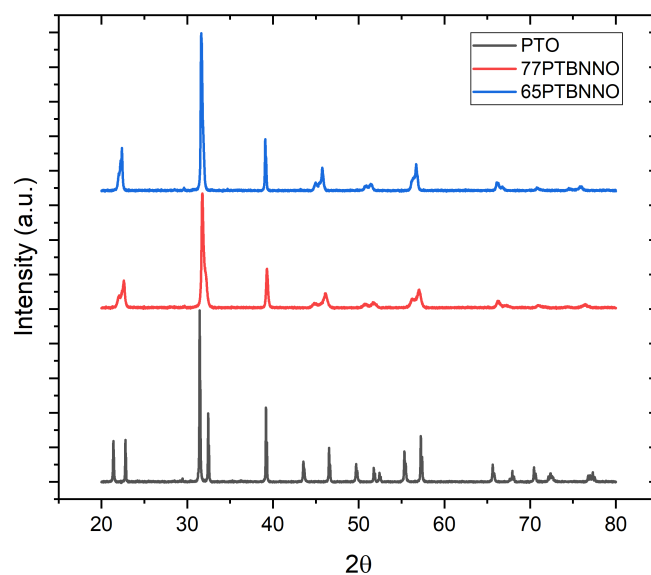


Figure S1: Powder XRD patterns of the targets. Result are in agreement with earlier studies: PTO exhibits the $P4_{mm}$ space group; with increased doping, the tetragonality reduces and the 65PTBNN0 structure is in vicinity of the morphotropic phase boundary with a cubic phase.

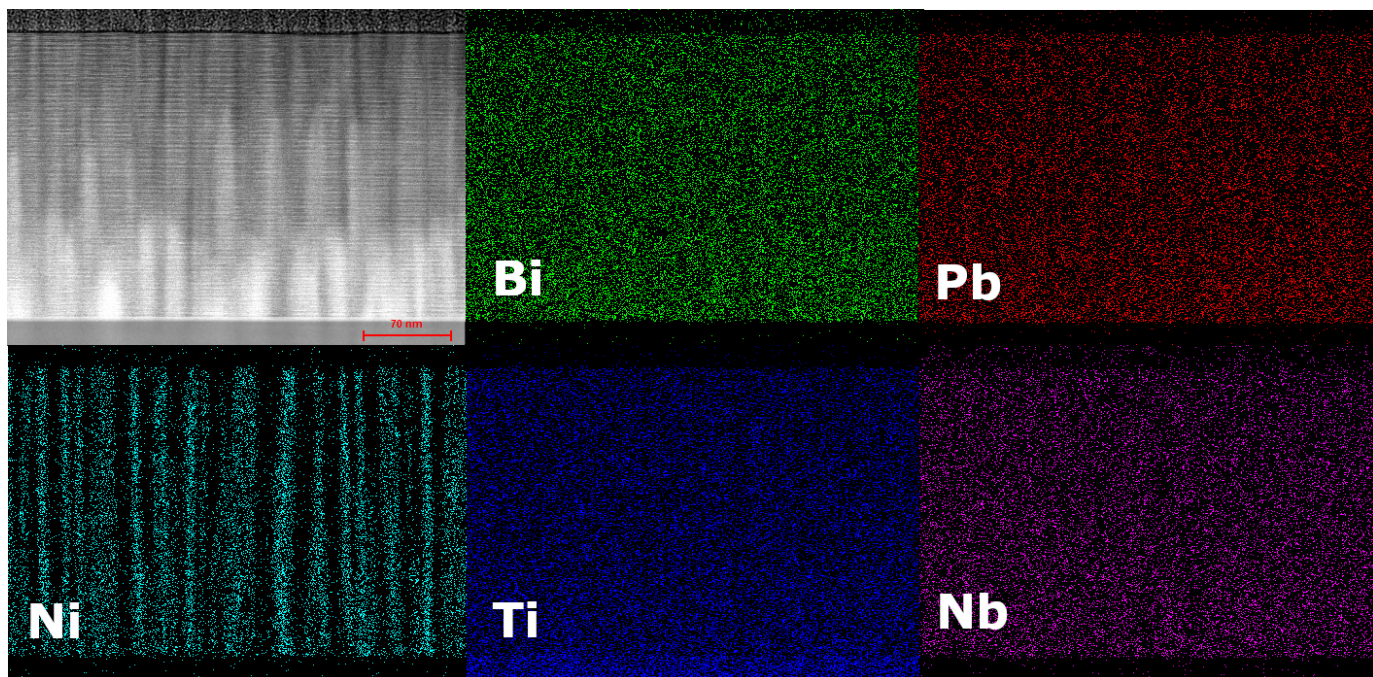


Figure S2: Complete EDX measurement of a 220 nm 65PTBNN0 film on STO

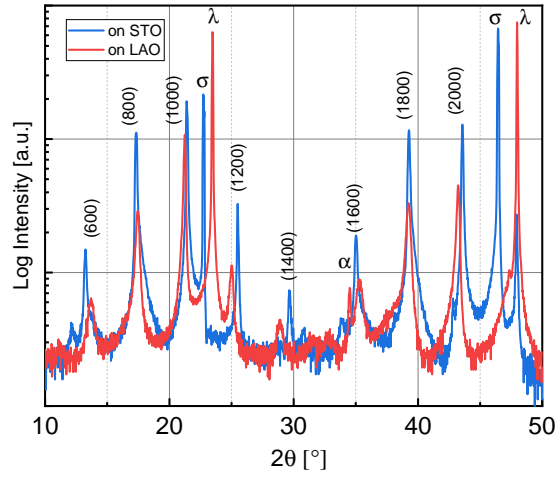


Figure S3: Comparison of XRD 2θ - ω -patterns for 100 nm thin 65PTBNNO films on STO and LaAlO_3 (001) substrates. While the (hkl) notation refers to the expected peaks of an Aurivillius phase, σ and λ denote STO and LAO peaks, respectively, and α denotes a minor secondary phase peak only detected in the sample on LAO, which, considering its position and the elements involved, could be tentatively assigned to PbNb_2O_6 .

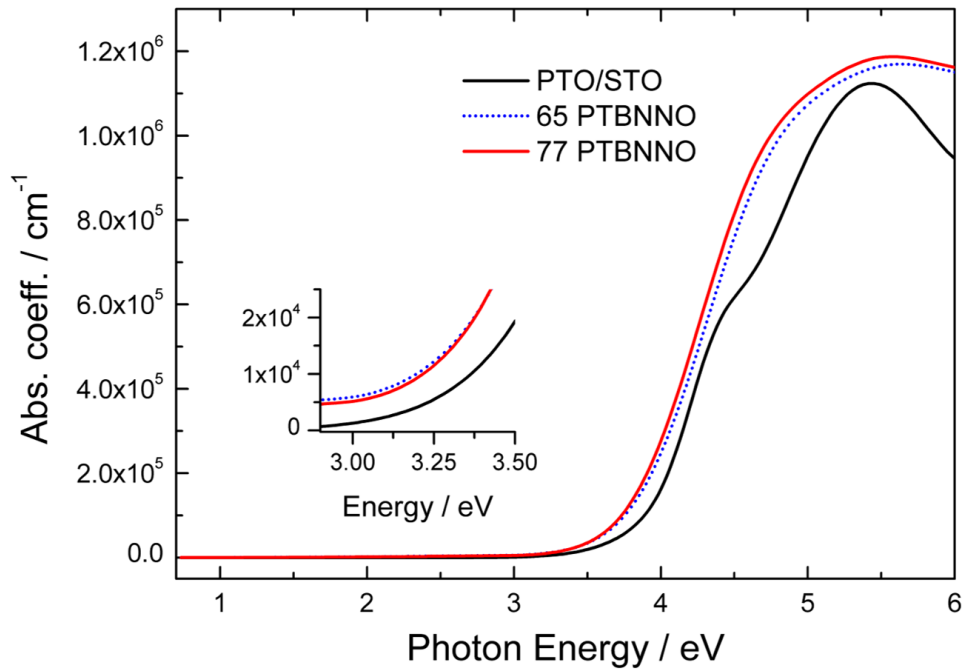


Figure S4: Photoabsorbance measurement of PTO, 77PTBNNO and 65PTBNNO thin films on STO.

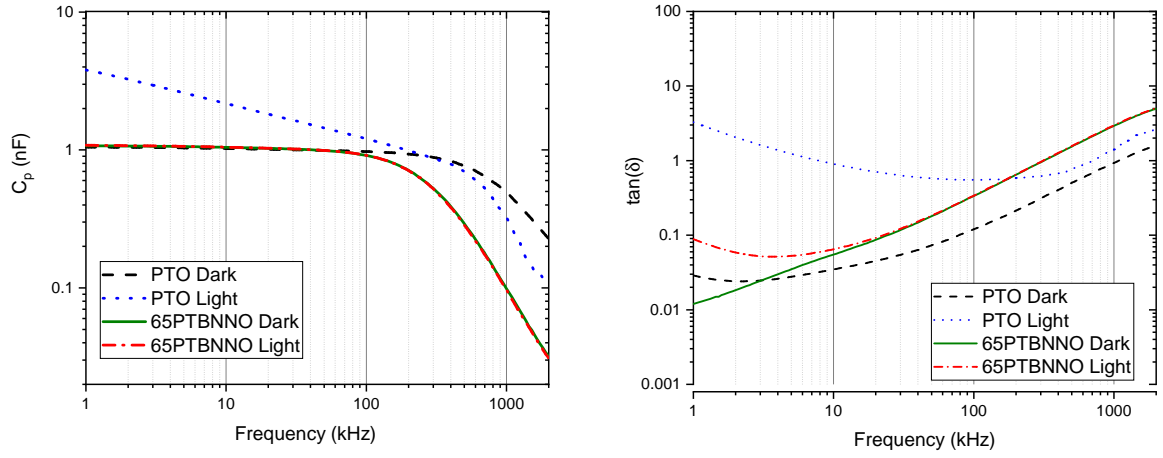


Figure S5: Left. Capacitance values measured for 100 nm thin films on Nb:STO with a 0.28 mm^2 large ITO top electrode, using the parallel equivalent circuit model. Right: Loss tangent (Dissipation factor). In the legend, "Light" refers to a 1 W cm^{-2} laser illumination with a wavelength of 405 nm.

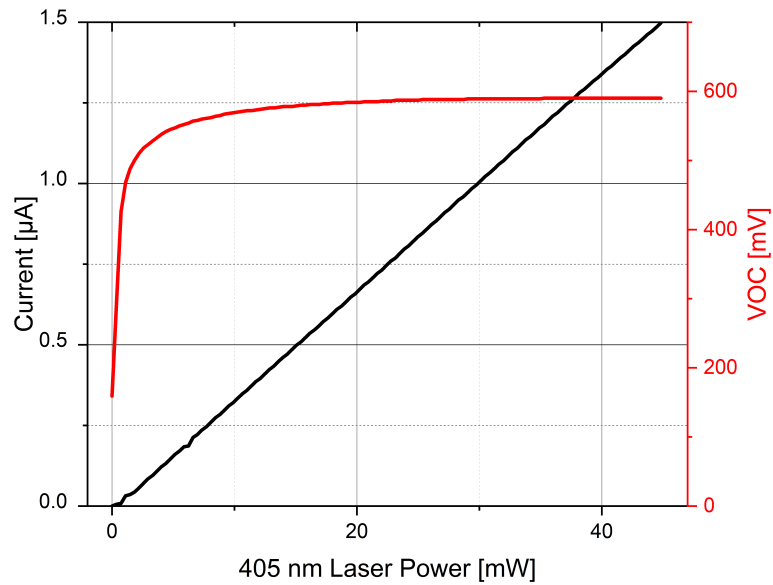


Figure S6: Dependency of Short Circuit Current (left axis, black) and Open Circuit Voltage (right axis, red) of a ITO/65PTBNNO/Nb:STO heterostructure on the light intensity (405 nm laser).

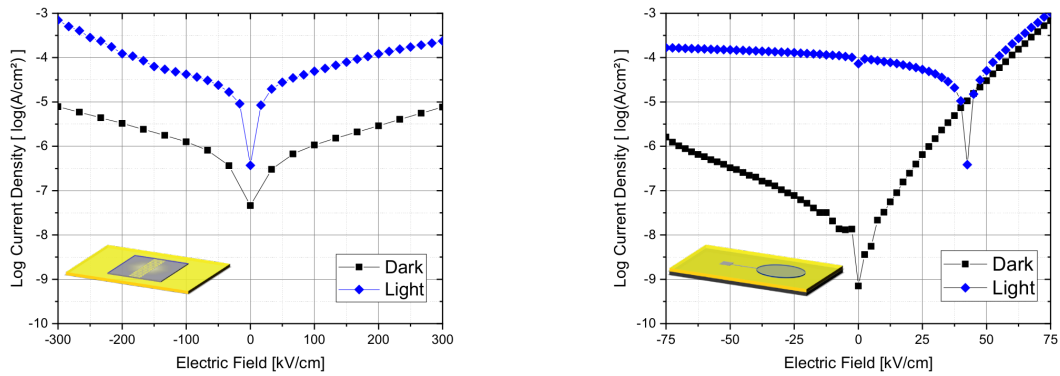


Figure S7: IV curves of 100 nm thin 65PTBNN0 films on (Nb:)STO (001) substrate in the dark and under 1 W cm^{-2} laser illumination with a wavelength of 405 nm for (a) in-plane and (b) out-of-plane electrode geometry. For in-plane measurement, the film was contacted by sputtered Pt/Pd (4:1) top electrodes that were patterned by maskless photolithography to an interdigital symmetrical arrangement with $3 \mu\text{m}$ gap width, depicted at the bottom left: 28 fingers with an area of $30 \times 3 \mu\text{m}^2$ each, resulting in an effective electrode edge length of roughly 1 mm. For out-of-plane measurement, the top and bottom were contacted by a 0.28 mm^2 ITO electrode and conductive Nb:STO substrate, respectively.

Details on the preparation of ceramic targets

A pure PbTiO_3 target was purchased from *PI-KEM Ltd.*. A $(\text{PbTiO}_3)_{0.77}(\text{BiNi}_{2/3}\text{Nb}_{1/3}\text{O}_3)_{0.23}$ (77PTBNNO) and a $(\text{PbTiO}_3)_{0.65}(\text{BiNi}_{2/3}\text{Nb}_{1/3}\text{O}_3)_{0.35}$ (65PTBNNO) target were synthesized by traditional solid-state chemistry using a stoichiometric mixture of Bi_2O_3 (Sigma-Aldrich 99%), PbO (Sigma-Aldrich 99%), NiO (Sigma-Aldrich 99%), Nb_2O_5 (Sigma-Aldrich 99.9%), and TiO_2 (Sigma-Aldrich 99%). Before weighing the reactants, all the powders were dried for 12 h at 200 °C. Raw materials were mixed properly using an agate mortar-pestle for 2 h with AR grade acetone as the mixing media. Further, mixed powders were ball milled in zirconia jars containing zirconia balls for 6 h using a planetary ball mill (*Retsch GmbH*, Germany) to get the homogeneous mixture. AR grade acetone was used as mixing media during the ball milling process. The ball-milled slurry was dried at room temperature, and then the powder was placed in an alumina crucible for heat treatment using muffle furnace. The mixture was calcined at an optimized temperature of 850 °C for 6 h under ambient air. The calcined sample was crushed and ground into fine powders using a mortar-pestle and was ball milled for 3 h. The multi-step calcination process was repeated to get phase pure solid solution of the compositions. Before target preparation, the calcined samples were crushed, ground and again ball milled for 3 h to improve the uniformity. An organic material polyvinyl alcohol (PVA) was used as a binder to prepare green pellets. A distilled water solution of 2% PVA was added to the calcined powder and thoroughly mixed using an agate mortar and pestle. The green pellets of a circular disc with a thickness of 4 mm were prepared using cylindrical steel die of 55 mm diameter. The pellets were made by keeping the powder in the stainless steel die and uniaxially pressed at an optimized load 70 kN using a hydraulic press. Before sintering, the green pellets were annealed at 500 °C for 12 h to completely burn-off the PVA binder. The sintering of green pellets was carried out in a bismuth and lead oxide atmosphere inside the sealed alumina crucible. A small amount of sacrificial powder of PbO and Bi_2O_3 was kept inside the alumina crucible to prevent the loss of bismuth and lead oxides during high-temperature sintering. An optimized sintering temperature of 1000 °C was used to get

highly dense pellets.

Experimental details: TEM and EDX measurement

The preparation of cross-sectional specimens for transmission electron microscopy (TEM) observations was done by a combination of focused gallium (30 keV, 15 keV and 5 keV) and focused argon (900 eV and 500 eV) ion beam milling. The internal structure of PTBNNNO thin films was investigated in a probe Cs-corrected Titan3 G2 60–300 microscope operating at 300 keV accelerating voltage. For scanning TEM (STEM), a probe forming annular aperture of 20 mrad was used. Z contrast images were recorded with a high-angle annular dark-field (HAADF) STEM detector using annular ranges of 80–200 mrad while annular-dark field (ADF) STEM covering annular ranges of 19–107 mrad was simultaneously used for acquisition of ADF-STEM images to take into account elastically Bragg scattered electrons. EDX maps were acquired with FEI Super-X EDX detector system, while beam currents were limited to about 180 pA during the EDX mapping.

5.2 [LM3] Control of Layering in Aurivillius Phase Nanocomposite Thin Films and Influence on Ferromagnetism and Optical Absorption

Control of Layering in Aurivillius Phase Nanocomposite Thin Films and Influence on Ferromagnetism and Optical Absorption

Lutz Mühlenbein, Chandra Bhal Singh, Akhilesh Kumar Singh, Ignasi Fina, Cameliu Himcinschi, Andriy Lotnyk, and Akash Bhatnagar*



Cite This: *ACS Appl. Electron. Mater.* 2022, 4, 1997–2004



Read Online

ACCESS |



Metrics & More

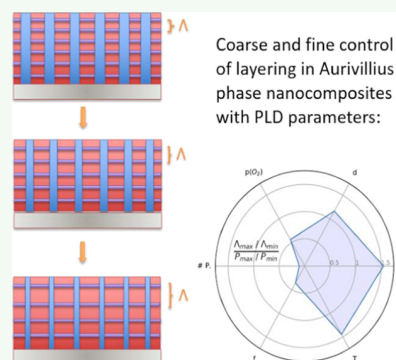


Article Recommendations



Supporting Information

ABSTRACT: Layered structures in complex oxide systems, reminiscent of superlattices, albeit naturally occurring, are often considered superior than their respective rudimentary forms. The enhanced functionalities related to the ferroic character have been known for a while now, and the enhanced photoelectrical properties have been only very recently demonstrated. Despite the improved performance, synthesis of such structures with precise control remains to be a bottleneck. In this work, this issue is addressed with a perovskite phase target of $(\text{PbTiO}_3)_{0.65}(\text{BiNi}_{2/3}\text{Nb}_{1/3}\text{O}_3)_{0.35}$. The deposition parameters are shown to have a deterministic control over the phase of the resultant thin film, that is, a layered Aurivillius phase or a perovskite phase. The resultant layered phase is demonstrated to have superior ferroic properties, in addition to an improved light absorption in the visible regime, thus making it an attractive photoferroic system.



Coarse and fine control of layering in Aurivillius phase nanocomposites with PLD parameters:

KEYWORDS: oxide thin film, layered perovskite, Aurivillius phase, vertically aligned nanocomposite, ferromagnetism, pulsed laser deposition

INTRODUCTION

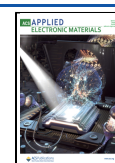
Aurivillius-phased layered structures in ferroelectric oxides are often considered as ideal candidates for practical applications. The phase has a general formula $(\text{Bi}_2\text{O}_2)(\text{A}_{m-1}\text{B}_m\text{O}_{3m+1})$ for a phase of order m , comprising m perovskite blocks sandwiched by Bi_2O_2 fluorite-like layers. The structure is known to be robust and tolerant against off-stoichiometry-induced electronic defects such as vacancies. While the Bi_2O_2 layers are known to compensate the oxygen vacancies,¹ the out-of-plane phase boundaries assist in maintaining charge neutrality arising from cation vacancies.² Owing to the robustness, the layered structures are also very conducive to doping with other ions. In the case of BiTi-based Aurivillius structures, Mn-doping was found to be instrumental in improving the ferromagnetic character,³ while the incorporation of Co manifested in a modified band gap.⁴ Robust ferroelectricity was recently proven to persist even in ultrathin Aurivillius phase thin films.^{5,6} Despite these apparent advantages of the structure, the synthesis in a device-relevant thin film form cannot be considered trivial. A similar issue was addressed in a recent work, wherein molecular beam epitaxy (MBE) was implemented to synthesize Ruddlesden–Popper structures, achieving an accurate control over the layer periodicity by adjusting the corresponding MBE shutter times.⁷ With the present work, we demonstrate the achievement of such a control with pulsed laser deposition (PLD) and identify suitable process parameters for both coarse and fine tuning of layering.

A perovskite-phased composite PLD target of $(\text{PbTiO}_3)_{0.65}(\text{BiNi}_{2/3}\text{Nb}_{1/3}\text{O}_3)_{0.35}$ (PTBNNNO) was used for the study, deposition from which results in a nanocomposite structure of NiO columns in an Aurivillius phase matrix, as previously reported.⁸ Variations in laser fluence, temperature, and oxygen pressure were used to elaborate on the conditions that support layering and thus the Aurivillius phase. While the coarse control of the deposition parameter allows a deterministic control over the resultant phase, that is, between Aurivillius and perovskite, the fine control allows to tune the layering within the Aurivillius phase. Furthermore, the impact of layering was assessed with magnetic and optical characterizations. An anomalous ferromagnetic response from the layered structures was recorded, which was absent in the nonlayered and perovskite samples. The layering also assisted in enhancing the absorption of the wavelengths falling in the visible part of the solar spectrum. An intricate ordering of Ni ions within the Aurivillius phase, validated with the images acquired with transmission electron microscopy (TEM), is

Received: February 3, 2022

Accepted: March 30, 2022

Published: April 12, 2022



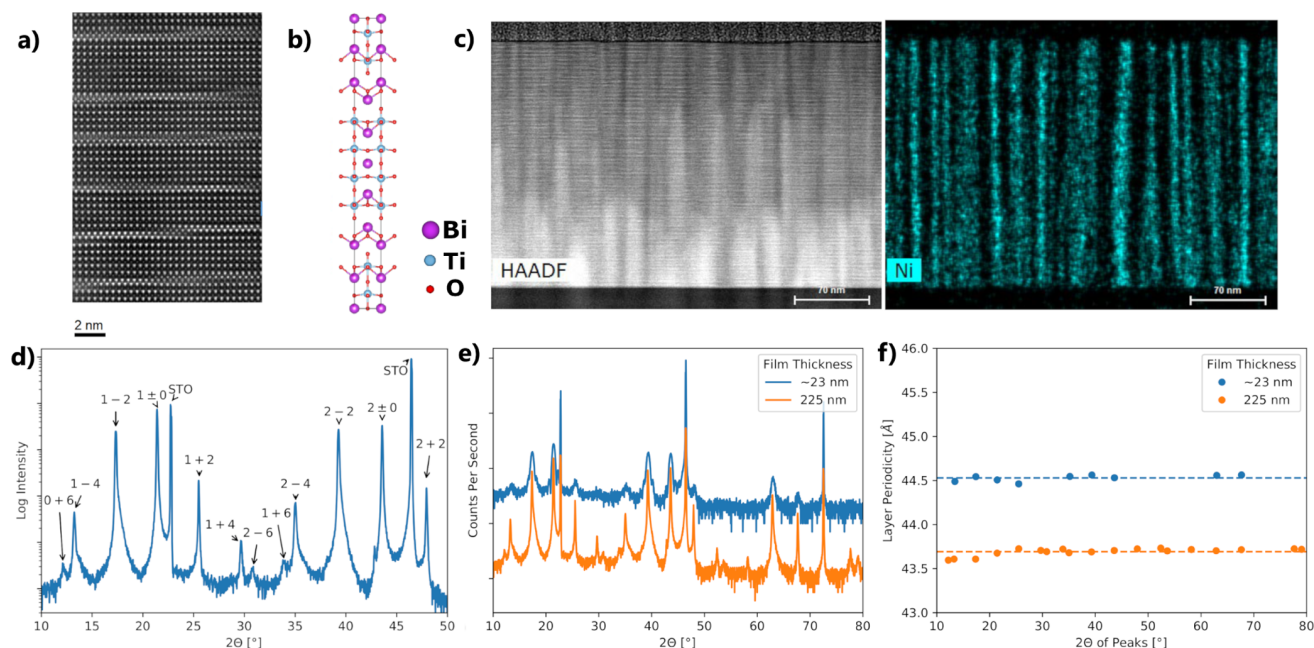


Figure 1. (a) High-resolution high-angle annular dark-field scanning TEM (HAADF-STEM) image of the Aurivillius phase in a PTBNNO thin film. Imperfections such as OPBs are apparent. (b) Unit cell of bismuth titanate along the [110] direction, an Aurivillius phase with $m = 4$. Graphics made with VESTA.⁹ (c) HAADF-STEM micrograph of the whole cross section of a PTBNNO film, together with EDX data showing phase-segregated NiO columns. (d) XRD pattern of a PTBNNO nanocomposite thin film with $m = 4$ and $c = 1.053$. For a perfect $m = 4$ structure, with $c = 1$, the $0 + 6$ and $1 - 4$ peaks would coincide, as well as $1 + 4$ and $2 - 6$, $1 + 6$ and $2 - 4$, and so on. (e) XRD patterns (log scale) and (f) extracted peak positions with the calculated layer periodicity according to eq 1 for $m \approx 4$ PTBNNO films on STO with a 10-fold difference in pulse number and the resulting thickness.

proposed as the underlying reason for the enhanced functional properties.

RESULTS AND DISCUSSION

Growth. Figure 1a,d shows a transmission electron micrograph and an X-ray diffraction (XRD) pattern of a PTBNNO thin film deposited on the SrTiO_3 (STO)(001) substrate, as was also discussed in our previous publication.⁸ Aurivillius phases, with the general formula $(\text{Bi}_2\text{O}_2)_{m-1}\text{B}_m\text{O}_{3m+1}$ for a phase of order m , are characterized by m perovskite blocks sandwiched within Bi_2O_2 fluorite-like layers. The XRD pattern for an Aurivillius phase is typically interpreted as reflections arising from the lattice planes inside the rather prolonged unit cell, as depicted in Figure 1b. Here, the cell is shown along the [110] direction, which corresponds to the alignment of the Aurivillius phase in the PTBNNO composite film grown on STO(001), as the comparison to Figure 1a shows.

Analogous to the thin-film superlattice systems or III–V semiconductor quantum wells, the pattern can be alternatively interpreted as consisting of several central zero-order peaks. The 2θ value separating them determines the average interlattice spacing of the whole unit cell, while the higher order “satellite” peaks, appearing symmetrically around them, arise from the layer periodicity (spacing after which the pattern is repeated).

Imperfections such as the vertical out-of-phase boundaries (OPBs) at the Bi_2O_2 layers lead to a rather thin-film-specific XRD pattern, unlike the bulk Aurivillius phase, that is, certain peaks seem to be “split”, as in Figure 1d.² The OPBs can result in a periodicity of the film that is lower or higher than the bulk equivalent, even though the stoichiometry is exactly the same.⁷

The lattice periodicity Λ can be extracted from the position of the film peak as⁷

$$\Lambda = \frac{\lambda(L_i + l_0c)}{2 \sin \theta_i} = \frac{\lambda(L_i + (2m + 2)\xi c)}{2 \sin \theta_i} \quad (1)$$

with the peak position angle θ_i of the satellite peak of order L_i around the central peak of order ξ , with $l_0 = (2m + 2)\xi$ —the conventional Miller index of the central peak ξ for the Aurivillius phase of order m , X-ray wavelength λ , and correction factor c , defined below. Central peaks ξ are exceptional among the reflections as their positions are not determined by the layer periodicity as such but by the average lattice spacing across one Aurivillius phase unit cell; thus, they occur at similar positions for different values of m and correspond to the reflections of a pure perovskite lattice. We chose to denote satellite peak orders with even numbers, L_i , to simplify conversion to the conventional Miller indices, which are all even; naturally this factor of two is arbitrary.

For instance, peaks in Figure 1d are labeled as “ $\xi + L_i$ ”. For $m = 4$, as in the case presented, this means $l_0 = 10$ for the first central order ($\xi = 1$) and $l_0 = 20$ for the second central order ($\xi = 2$). c , a unitless correction factor

$$c = \frac{\Lambda}{\Lambda_{\text{ideal}}} = \frac{\Lambda}{l_0 d_{00l}} \quad (2)$$

with d_{00l} denoting the Bragg spacing of peak $00l_0$, is a measure of imperfection for a certain member of the Aurivillius phase homologous series. In a self-consistent approach, the correction factor that yields the same Λ for all superstructure peaks should be selected.⁷ In conjunction to the layering, vertically aligned nanocolumns (VAN) running across the entire thickness of the samples were also observed (Figure 1c).

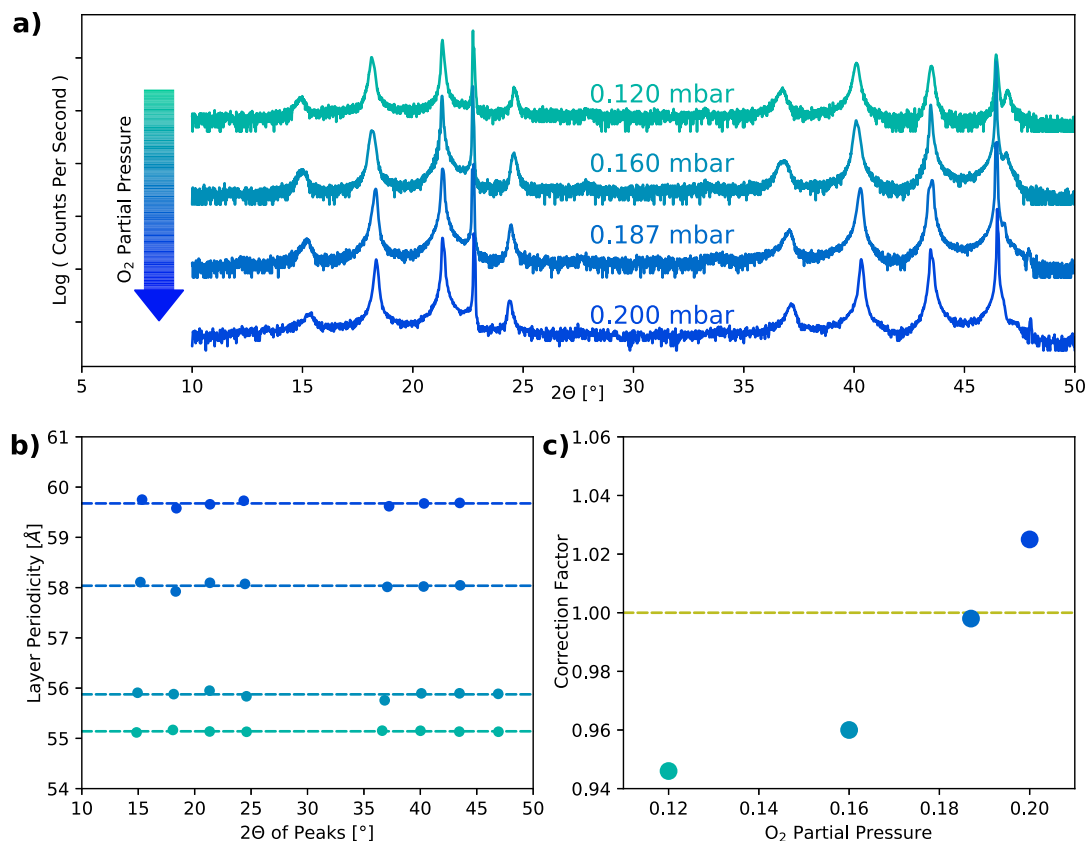


Figure 2. (a) XRD Patterns of PTBNNOs samples deposited on STO substrates. $d = 60$ mm, $J = 0.85$ J cm⁻², $P = 5000$, and $p = 0.4$ mbar, with varying O₂-to-Ar ratios (O₂ partial pressure as labels in the figure). (b) Extracted peaks for XRD patterns, with layer periodicity values calculated according to eq 1. (c) Corresponding correction factors calculated according to eq 2 in dependence of O₂ partial pressure.

Upon analysis with energy-dispersive X-rays (EDX), the columns were found to be accommodating rich proportions of NiO (Figure 1c). The inability of the Aurivillius phase to accommodate divalent elements, like nickel, on the octahedral sites of the perovskite blocks might be the underlying reason, which also explains the co-appearance of VAN only in the samples exhibiting an Aurivillius phase.

In the following sections, we will investigate the influence of different PLD process parameters on the layer periodicity of the Aurivillius phase in PTBNNOs nanocomposite thin films, namely, pulse number P , pulse frequency f , laser fluence J , background gas atmosphere p , substrate temperature T , and substrate-to-target distance d . We analyze their respective influence and identify those which can be considered as useful controls for tuning the layering. Subsequently, the influence of periodicity on the functionality of the samples pertaining to magnetism and light absorption will be presented.

Pulse Number. The pulse number largely determines the resultant film thickness and thus, already from a conceptual perspective, hardly qualifies as an optimization control, as thickness should remain a free parameter adjustable according to external demands. However, as variations in the other process parameters can influence the growth rate, it is nevertheless an interesting question whether the film thickness can also influence the layer periodicity. Therefore, a film analogous to the 225 nm thin PTBNNOs film presented in our previous work⁸ was grown, with the pulse number reduced to 1/10th of the previous value. The XRD patterns of both films are shown in Figure 1e. The extracted peak positions, together

with the periodicity value of each layer, were calculated according to eq 1 and are presented in Figure 1f. Due to the XRD signal-to-noise ratio, the number of extracted peaks for the thicker film is higher than that for the thinner film. Nevertheless, in both cases, the number of extracted peaks is high enough to calculate the periodicity with picometer precision. The result shows that for a 10-fold change in thickness, the layer periodicity varies only by 0.84 Å in absolute terms or by 1.9% in relative terms.

Background Gas Atmosphere. Figure 2 shows the results for the dependence of layer periodicity on the changes in the composition of background atmosphere during growth. The four samples were deposited on STO substrates at 625 °C and 2 Hz, $d = 60$ mm, $J = 0.85$ J cm⁻², $P = 5000$, and $p = 0.4$ mbar with varying ratios of O₂ and Ar. The XRD patterns seem similar at first glance, yet detailed analysis of the peak positions according to eq 1 results in a clear trend of proportional increase of layer periodicity with O₂ partial pressure. The Aurivillius phase in all films is of the order $m = 6$ but with different correction factors; a correction factor close to 1, $c = 0.998$, is found for the film deposited under 0.187 mbar O₂ partial pressure.

Substrate Temperature and Pulse Frequency. Figure 3 shows the results for the dependence of layer periodicity on the substrate temperature and pulse frequency. Samples were deposited on STO substrates at 600, 625, and 650 °C and 2, 4, 7 and 10 Hz in all combinations. The remaining parameters were set to $d = 50$ mm, $J = 1.0$ J cm⁻², $P = 3000$, and $p = 0.4$ mbar with 1:1 O₂-to-Ar ratio. A clear dependency of the layer

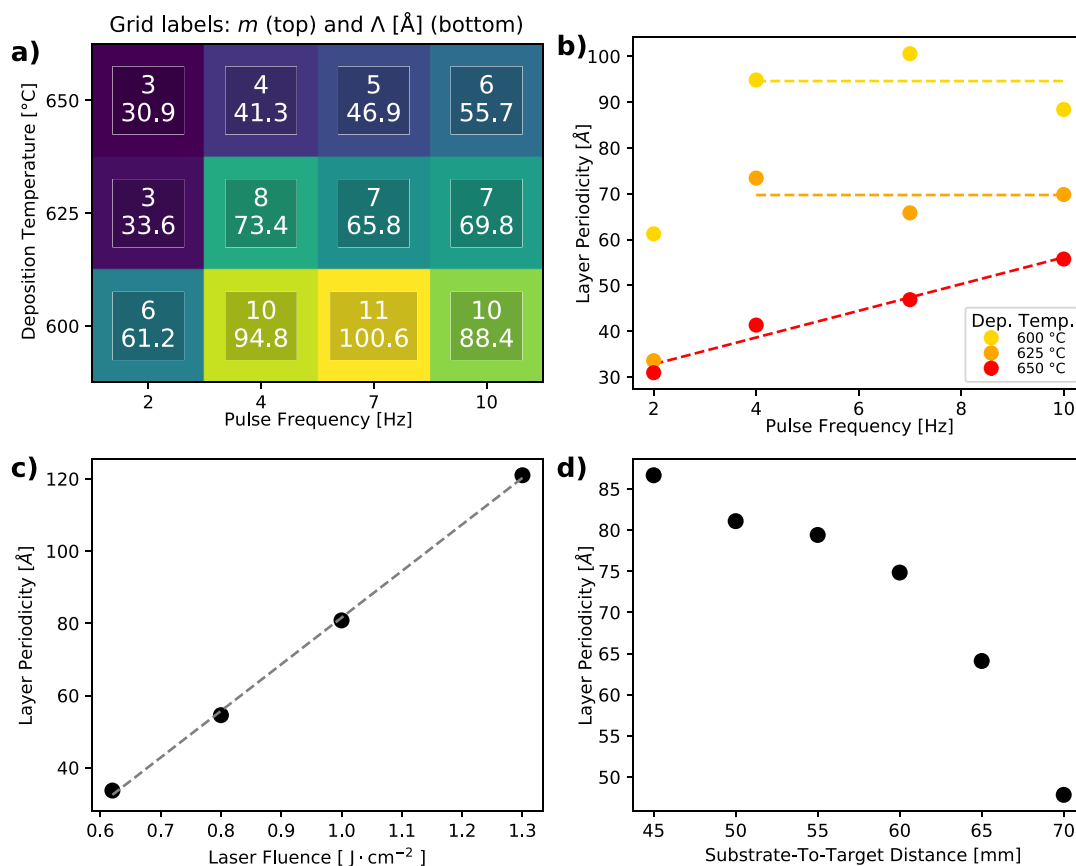


Figure 3. (a) Dependence of Aurivillius phase index m (top grid labels) and layer periodicity Λ (in Å—bottom grid labels) on substrate temperature and laser pulse frequency. (b) Best-fit m and Λ values according to eqs 1 and 2 extracted from XRD measurements. (c) Dependence of layer periodicity on the laser fluence J . (d) Dependence of layer periodicity on the substrate-to-target distance d .

periodicity on the temperature is apparent: at a constant frequency, in all cases, a higher temperature results in a lower layer periodicity. On the contrary, the dependency on the frequency is rather ambiguous. For instance, at a given temperature, the variation in frequency causes an evident change in the periodicity that tends to saturate at 10 Hz, and thus the frequency appears to be rendered redundant.

Laser Fluence and Substrate-to-Target Distance. The dependence of the layer periodicity on the laser fluence is displayed in Figure 3c. Four samples were deposited on STO films at 625 °C, $f = 10$ Hz, $d = 60$ mm, $P = 5000$, $p = 0.4$ mbar with 1:1 O₂-to-Ar ratio, and varying laser fluence. The periodicity appears to be very sensitive to the laser fluence setting and rises linearly with the laser fluence, following a slope of roughly 130 Å cm J⁻¹.

The dependence of the layer periodicity on the substrate-to-target distance is presented in Figure 3d. Six samples were deposited on STO substrates at 625 °C, 10 Hz, $J = 0.8$ J cm⁻², $P = 2500$, $p = 0.4$ mbar with 1:1 O₂-to-Ar ratio, and distance was varied in steps of 5 mm. The periodicity monotonously tends to drop with the distance; however, unlike laser fluence, the changes are not linear.

Magnetic Characterization. A set of samples with different orders of the homologous series was measured by SQUID magnetometry alongside a PbTiO₃ reference film grown in the same chamber. The results of hysteresis measurements at 4.2 K are shown in Figure 4a, and the zero-field-cool/field-cool curves are shown in Figure 4b. A

ferromagnetic response is evident in the low-end member of the Aurivillius series, which disappears in the perovskite-like structure.

The magnetic measurements revealed a large discrepancy in the magnetic properties of the PTBNNNO composite structure with different layer periodicities. The dense-layered structure proved to be strongly ferromagnetic, whereas the almost perovskite-like structure hardly is. However, it seems unlikely that the Aurivillius phase itself can be the origin of the ferromagnetic response, as it does not contain any cations that are magnetic or would qualify for double-exchange interaction, unlike Fe- or (Fe, Mn)-doped bismuth titanate thin films for which ferromagnetism has been reported.^{10,11} To explain this, we have to take a closer look on the other member of this nanocomposite system, the NiO nanocolumnar structures.

While NiO is an antiferromagnetic material,¹² ferromagnetism has been reported in NiO nanoparticles due to the uncompensated spins from the surfaces dominating over the bulk effects at these small scales.^{13,14} Alternatively, in another study, involving bulk crystals of NiO, the chemical non-stoichiometry at the lattice defects (dislocations) was sufficient to extract local ferromagnetic response from an otherwise antiferromagnetic matrix.¹⁵ Both of these scenarios are probable and could be at the origin of the ferromagnetic behavior at the NiO columns in the densely layered composite film. Ferromagnetism originating at NiO columns in thin-film VANs has been recently reported by Rutherford et al.¹⁶

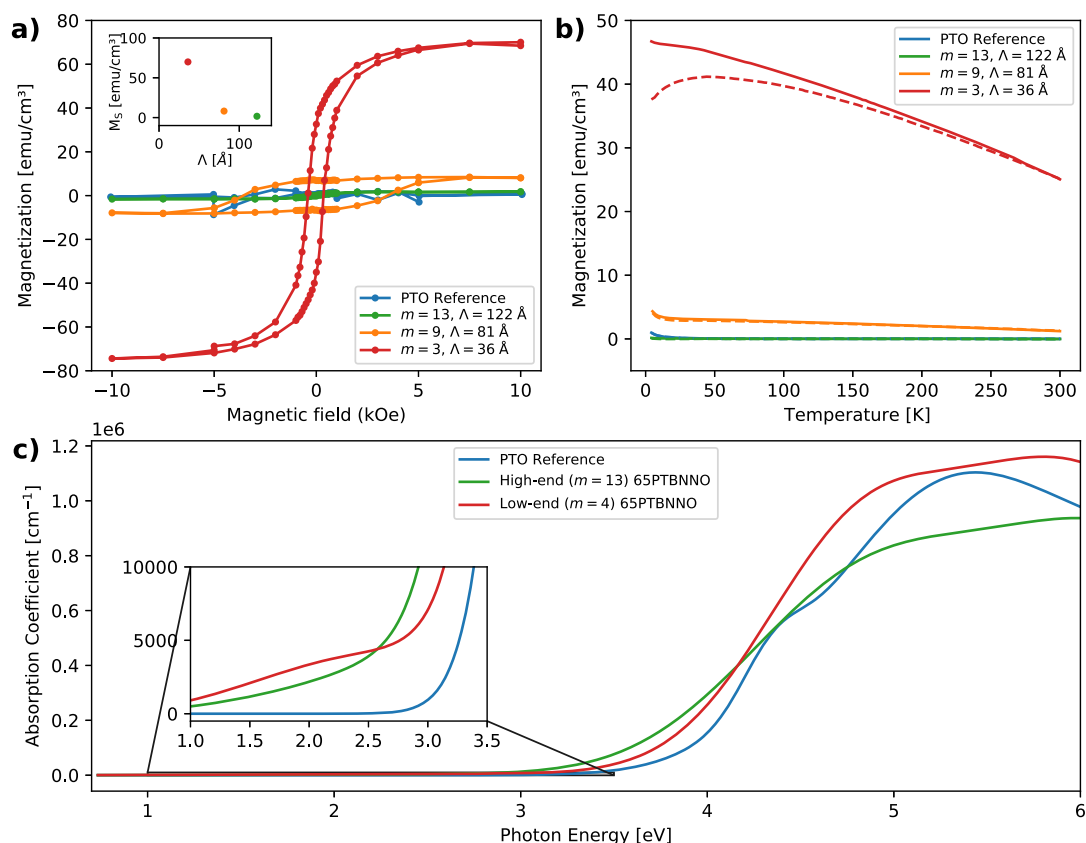


Figure 4. (a) Magnetic hysteresis measurement at $T = 4.2$ K. The inset shows the dependence of saturation magnetization M_S on layer periodicity Λ . (b) Zero-field-cool (dashed) and field-cool (solid) curves for a PTBNN0 film comprising a low-end ($m = 3$), a mid-range ($m = 9$), and a high-end, almost perovskite-like ($m \approx 13$), member of the Aurivillius phase homologous series, in addition to a PbTiO_3 sample grown in the same chamber. (c) Optical absorption spectra acquired from PbTiO_3 , and PTBNN0 samples from low-end ($m = 4$) and high-end ($m \approx 13$), almost perovskite-like, member of the Aurivillius phase homologous series.

The decrease of ferromagnetism with decreasing density of layering is explained by the following argument: the formation of NiO columns is interdependent with the Aurivillius phase due to nonmiscibility; the Aurivillius phase commonly does not accommodate divalent cations at the B-sites of the perovskite lattice.¹⁷ However, with the increase in the layer periodicity, the film structure more and more mimics the original PLD target phase, the PbTiO_3 perovskite phase, with Bi substituting at A-sites and Ni and Nb substituting at B-sites. This means that in the near-perovskite film, the formation of NiO columns is unlikely and Ni is rather dispersed among the structure.

Absorption Measurements. The layered Aurivillius structure also has an evident impact on the optical absorption of the samples. In Figure 4c, the absorption characteristics acquired from the layered and perovskite-like structures, along with that of PTO, are presented. The absorption in the case of PbTiO_3 remains rather minimal till about 3.15 eV, after which a rise in absorption is observed, with the maximum appearing at energies that are well above the reported values of band gap. A similar scenario seems to be relevant also for the composite systems (layered and perovskite). However, a closer look within the visible range of the energies (inset of Figure 4c) suggests substantial optical transitions occurring in the composite systems. The PTBNN0 samples absorb nearly 100 to 10000 times more in comparison to PbTiO_3 , till about 3 eV, after which the respective responses tend to converge. The

larger absorption in the PTBNN0 samples might be attributed to the coupling between the Ni ion and oxygen vacancy which has been theoretically predicted to lower the bottom of the conduction band, thereby reducing the band gap.¹⁸ Furthermore, the slight differences between the absorption characteristics of $m = 4$ and $m = 13$ samples probably arise from the positioning of nickel ions, that is, segregated within the columns and uniformly dispersed, respectively.

DISCUSSION

The results displayed in the previous section regarding the influence of PLD parameters on the layer periodicity are summarized in Figure 5. Here, a unitless estimate of sensitivity, S , of periodicity Λ on the specific parameter P was calculated by dividing the ratios of minimum and maximum values:

$$S = \frac{\Lambda_{\max}/\Lambda_{\min}}{P_{\max}/P_{\min}} \quad (3)$$

Due to nonlinearity in the dependence of Λ on parameters in certain ranges, the factor S certainly lacks the accuracy to conduct a precise quantitative assessment for sensitivity for complete parameter ranges and should be considered as a qualitative estimate for comparing the overall impact among parameters.

As was argued in the very beginning of the result section, the influence of pulse number and resulting thickness now seems negligible in comparison to the sensitivity on other parameters,

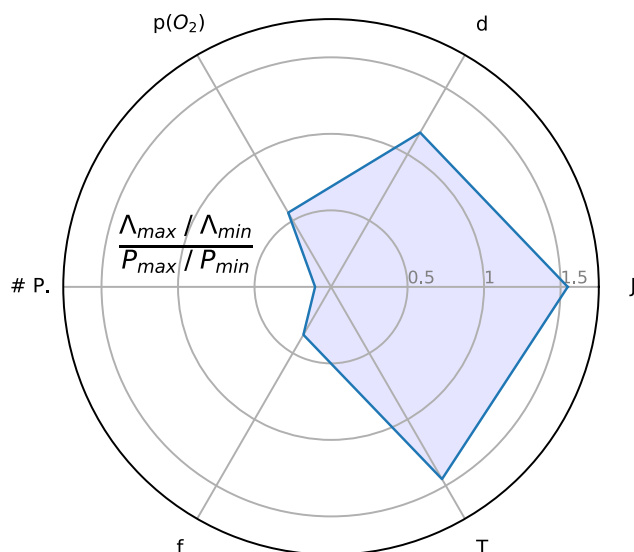


Figure 5. Overview of estimates for the sensitivity of the layer periodicity on PLD parameters, calculated by dividing the relative change in periodicity by the relative change in the parameter setting for the marginal values shown in the Results section. #P: number of pulses, $p(\text{O}_2)$: oxygen partial pressure, d : substrate-to-target distance, J : laser fluence, T : substrate temperature, and f : pulse frequency.

which makes a direct influence of overall film thickness unlikely. The periodicity seems to be especially sensitive to laser fluence and substrate temperature; therefore, we may propose here that both of these parameters qualify as coarse control for layering, and with small changes in these parameters, the index of the Aurivillius phase homologous series can be easily shifted. However, due to the high sensitivity toward these parameters, minute optimizations of the structure can be considered largely impractical. Here, the other parameters come into play that show a low sensitivity, namely the oxygen partial pressure and frequency. However, for frequency, the dependence was not strictly monotonous, and the variations in the periodicity beyond 4 Hz appear to be more subtle. Thus, especially the oxygen partial pressure can be identified here as a fine control of layering, with which the periodicity can be tuned precisely and almost continuously, analogous to the MBE shutter times in the work of Barone et al.⁷ Also, the change in gas composition is likely to influence the plume kinetics to an extent that has a minute, but still decisive, influence on the formation of layering at the substrate. Furthermore, from a practical point of view, common pressure sensors and gas flow controls are sensitive and precise enough to ensure almost continuous fine-tuning of Λ and c . In agreement with our findings, Gradauskaite et al. recently reported on stabilizing layer-by-layer growth modes in PLD for $\text{Bi}_{m+1}\text{Fe}_{m-3}\text{Ti}_3\text{O}_{3m+3}$ Aurivillius phase thin films and were able to adjust m from 4 up to 8 by increasing the laser fluence and background pressure.¹⁹

Keeping in perspective the aforementioned analysis, we are now in a position to address the underlying reasons for the observed dependencies, that is, which physical processes are adjusted when tuning these process parameters? It is known that the formation of oxide nanostructures can be governed by diffusion-limited processes during the growth.^{20,21} If this was the case here, the layer periodicity should scale inversely with the pulse frequency and increase with the deposition temperature following an Arrhenius equation.^{20,21} However,

our experimental results in Figure 3 suggest a rather contrary scenario for both the parameters: for all frequencies, the layer periodicity increases with decreasing temperature. Furthermore, for $T = 650$ K, the layer periodicity increases with increasing frequency. For the lower temperatures, a similar dependency can be identified for low frequencies, with a saturation setting in at higher frequencies. It can thus be implied that diffusion limitation is not the driving mechanism determining layer formation in these samples. Alternatively, from these experimental results, it can be surmised that the flux of ionic species, the competition between Pb and Bi, and re-evaporation processes play a governing role: both Pb and Bi are known to be volatile elements during PLD,²² meaning that during the growth, a loss of these elements due to re-evaporation often leads to Pb- or Bi-deficient films, an effect which becomes more prominent at higher temperatures. This provides an explanation for both the observed temperature and pulse frequency dependencies, assuming that the volatility of Pb is larger than the volatility of Bi. Such an observation was already made in PLD-deposited thin films from a target of composition $(\text{PbTiO}_3)_{0.65}(\text{BiTi}_{1/2}\text{Mg}_{1/2}\text{O}_3)_{0.35}$, a very similar composition to ours, where the resulting films were profoundly more Pb-deficient than being Bi-deficient, even when adding excess Pb to the target.²² Thus, in our case, at higher substrate temperatures, a lower relative Pb content leads to a low-layer periodicity, meaning films that resemble more the Aurivillius archetype $\text{Bi}_4\text{O}_3\text{Ti}_{12}$ ($m = 3$), while at lower temperatures, a higher relative Pb content leads to high-layer periodicity, that is, films resembling the perovskite archetype PbTiO_3 ($m \rightarrow \infty$). A similar argument can be made for the increase of layer periodicity with pulse frequency, as per unit time a large amount of ionic species arrives, while, for a constant temperature, the same amount re-evaporates. This is also supported by the dependencies of the layer periodicity on the laser fluence (proportional) and substrate-to-target distance (antiproportional). More material per time leads to the formation of a film with larger layer periodicity, that is, more resembling the perovskite phase, which seems to be energetically favored if the available Pb is sufficient for its formation.

We can now also briefly address the observed enhancements in the functional properties. The incompatibility of divalent Ni within the layered Aurivillius phase forces a major proportion of Ni ions to segregate in the form of columns and, owing to the presence of the surrounding oxygen content, to eventually settle in the form of NiO. On the other hand, in the perovskite-like composite samples, with larger values of m , no such traces of segregation were detected. The enhancement in functional properties, both ferromagnetism and optical absorption, appear to be interlinked with the ordering of Ni within the material matrix. The integral role of nanocolumns in improving the magnetic response is highlighted upon comparison with the perovskite-phased samples, wherein, despite the presence of Ni, albeit dispersed, the response remains minuscule and comparable to the reference PbTiO_3 .

However, the improved absorption at lower photon energies in the composites, overall, still needs further understanding. NiO by itself is one of the rare p-type oxide semiconductor with a wide band gap of above 3.4 eV²³ and serves as a hole-transport layer for different photovoltaic applications.¹² Therefore, the enhanced absorption cannot be attributed to NiO and should be rather driven by the distribution of Ni within the composite matrix. As a result, the absorption from both layered and nonlayered composites exhibits largely similar

characteristics. Interestingly, a similar scenario was also proposed as a strategy to modulate the band gap energy of PbTiO_3 while maintaining the polar character.²⁴ It was shown that doping with group 10 metals, such as nickel, essentially leads to considerable changes in the position of B-site cation and thus the band gap. A prerequisite for maintaining the charge neutrality of the structure is the presence of oxygen vacancies, and their presence is also perceivable in our samples. Nevertheless, additional experiments will be needed to validate these arguments.

CONCLUSIONS

We investigated the influence of PLD process parameters on the structure of PTBNNNO nanocomposite thin films, especially with respect to the layer periodicity of the Aurivillius phase matrix. We especially identify temperature and laser fluence as coarse controls for periodicity, with which the order of the homologous series can be selected. As a subsequent fine control for tuning the growth of a certain member, we identified the oxygen partial pressure in the background gas composition with argon. Keeping the overall pressure constant, a shift in the background gas composition effects only a minute change in plume kinetics, facilitating a precise control of the layer periodicity with a resolution of 1 Å.

Regarding coarse control, we demonstrated that with the same target, a $m = 3$ Aurivillius phase composite film and an almost perovskite-like film are feasible. The $m = 3$ film is ferromagnetic at room temperature, while the perovskite-like film, likewise the reference PbTiO_3 , can be considered nonmagnetic. The optical characterization revealed an overall superior response from the composite samples, layered and nonlayered, with substantially larger absorption in the visible range of light spectrum.

EXPERIMENTAL SECTION

Synthesis and Structural Characterization. PTO and PTBNNNO thin films were synthesized by the PLD system on STO substrates. Deposition parameters (pulse number P , pulse frequency f , laser fluence J , background pressure p , substrate temperature T , and substrate-to-target distance d) vary in this study, and the information is given in the main text accordingly. In addition to oxygen, argon was used as a background gas to disentangle control over plume kinetics and thermal re-evaporation on one side and oxidation process on the other.^{25,26} The structure of the thin films was analyzed with ex situ high-resolution X-ray diffractometry in a Bruker DISCOVER D8 diffractometer.

Transmission Electron Microscopy. Specimens for cross-sectional TEM observations were prepared by focused Ga ion beam milling (Zeiss Auriga Dual-beam FIB). A probe Cs-corrected Titan3 G2 60-300 microscope was used for TEM studies. The microscope was operated at 300 kV accelerating voltage. A probe-forming aperture of 20 mrad was applied during scanning TEM measurements. STEM images were recorded with an annular dark-field detector (Fischione) using annular ranges of 80–200 mrad, which correspond to HAADF or Z contrast imaging well. Electron beam current of 130 pA was applied for HAADF-STEM imaging and EDX mapping. The high-resolution HAADF-STEM micrograph shown in this work was postprocessed by a Wiener difference filter for the reduction of scanning noise and for the enhancement of the image intensity of individual atomic columns.

Magnetic Characterization. The magnetic properties of the PT(BNN)O thin films were probed by a MPMS3 SQUID magnetometer from Quantum Design. In-plane magnetic hysteresis loops $M(H)$ at 4.2 K were explored. ZFCFC experiments were performed after zero-field-cooling the sample to 4.2 K and measuring

while subsequently increasing the temperature to 300 K (ZFC) and decreasing to 4.2 K at 1000 Oe.

Optical Characterization. Spectroscopic ellipsometry measurements were performed in the 0.7–6 eV energy range and for incident angles of 60, 65, and 70° using an M-2000 Ellipsometer from J.A. Woollam. In order to obtain the complex refractive index (n, k) of the films, a four-phase model, substrate/film/roughness layer/ambient, was employed.²⁷ The optical response of the films was described using an oscillator model, while the roughness layer was considered to be a mixture of 50% film material and 50% voids by using Bruggeman effective medium approximation.²⁸ The optical constants of the substrate were obtained from previous measurements on a bare SrTiO_3 substrate. Having the extinction coefficient k of the films determined from ellipsometry, the absorption coefficient α was calculated as: $\alpha = 4\pi k/\lambda$. The absorption coefficient of the PTO reference and of the PTBNNNO samples (with $m = 4$ and $m = 13$) are plotted in Figure 4c.

ASSOCIATED CONTENT

Supporting Information

The Supporting Information is available free of charge at <https://pubs.acs.org/doi/10.1021/acsaelm.2c00160>.

Comparison of TEM-HAADF images of layered and “nonlayered” PTBNNNO films (PDF)

AUTHOR INFORMATION

Corresponding Author

Akash Bhatnagar – Zentrum für Innovationskompetenz SiLi-nano, Martin Luther Universität Halle-Wittenberg, Halle (Saale) 06120, Germany; Institute of Physics, Martin Luther Universität Halle-Wittenberg, Halle (Saale) 06120, Germany; orcid.org/0000-0001-6212-4576; Email: akash.bhatnagar@physik.uni-halle.de

Authors

Lutz Mühlenbein – Zentrum für Innovationskompetenz SiLi-nano, Martin Luther Universität Halle-Wittenberg, Halle (Saale) 06120, Germany; Institute of Physics, Martin Luther Universität Halle-Wittenberg, Halle (Saale) 06120, Germany

Chandra Bhal Singh – School of Materials Science and Technology, Indian Institute of Technology (Banaras Hindu University), Varanasi 221005, India

Akhilesh Kumar Singh – School of Materials Science and Technology, Indian Institute of Technology (Banaras Hindu University), Varanasi 221005, India; orcid.org/0000-0001-8729-7318

Ignasi Fina – Institut de Ciència de Materials de Barcelona-CSIC, Barcelona 08193, Spain; orcid.org/0000-0003-4182-6194

Cameliu Hincinschi – Institute of Theoretical Physics, TU Bergakademie Freiberg, Freiberg D-09596, Germany

Andriy Lotnyk – Leibniz Institute of Surface Engineering, Leipzig 04318, Germany; Laboratory of Infrared Materials and Devices, The Research Institute of Advanced Technologies, Ningbo University, Ningbo 315211, China; orcid.org/0000-0002-0000-9334

Complete contact information is available at: <https://pubs.acs.org/doi/10.1021/acsaelm.2c00160>

Notes

The authors declare no competing financial interest.

ACKNOWLEDGMENTS

The authors thank K. Dörr and D. Rata for the X-ray measurements, M. Lisca for the technical support, and B. Fuhrmann and S. Schlenker for their support with the facilities at the Interdisziplinäre Zentrum für Materialwissenschaften (IZM). Financial support from Deutsche Forschungsgemeinschaft (DFG) via Sonderforschungsbereiche (SFB) 762 (project A12), Bundesministerium für Bildung und Forschung (BMBF) project no. 03Z22HN12, and Europäischer Fonds für regionale Entwicklung (EFRE) Sachsen-Anhalt is gratefully acknowledged.

REFERENCES

- (1) Scott, J. F.; de Araujo, C. A. P. Ferroelectric Memories. *Science* **1989**, *246*, 1400–1405.
- (2) Zurbuchen, M. A.; Tian, W.; Pan, X. Q.; Fong, D.; Streiffer, S. K.; Hawley, M. E.; Lettieri, J.; Jia, Y.; Asayama, G.; Fulk, S. J.; Comstock, D. J.; Knapp, S.; Carim, A. H.; Schlom, D. G. Morphology, structure, and nucleation of out-of-phase boundaries (OPBs) in epitaxial films of layered oxides. *J. Mater. Res.* **2007**, *22*, 1439–1471.
- (3) Zurbuchen, M. A.; Freitas, R. S.; Wilson, M. J.; Schiffer, P.; Roeckerath, M.; Schubert, J.; Biegalski, M. D.; Mehta, G. H.; Comstock, D. J.; Lee, J. H.; Jia, Y.; Schlom, D. G. Synthesis and characterization of an $n=6$ Aurivillius phase incorporating magnetically active manganese, $\text{Bi}_7(\text{Mn,Ti})_6\text{O}_{21}$. *Appl. Phys. Lett.* **2007**, *91*, 033113.
- (4) Choi, W. S.; Chisholm, M. F.; Singh, D. J.; Choi, T.; Jellison, G. E.; Lee, H. N. Wide bandgap tunability in complex transition metal oxides by site-specific substitution. *Nat. Commun.* **2012**, *3*, 689.
- (5) Keeney, L.; Saghi, Z.; O'Sullivan, M.; Alaria, J.; Schmidt, M.; Colfer, L. Persistence of Ferroelectricity Close to Unit-Cell Thickness in Structurally Disordered Aurivillius Phases. *Chem. Mater.* **2020**, *32*, 10511–10523.
- (6) Gradauskaite, E.; Campanini, M.; Biswas, B.; Schneider, C. W.; Fiebig, M.; Rossell, M. D.; Trassin, M. Robust In-Plane Ferroelectricity in Ultrathin Epitaxial Aurivillius Films. *Adv. Mater. Interfaces* **2020**, *7*, 2000202.
- (7) Barone, M. R.; Dawley, N. M.; Nair, H. P.; Goodge, B. H.; Holtz, M. E.; Soukiassian, A.; Fleck, E. E.; Lee, K.; Jia, Y.; Heeg, T.; Gatt, R.; Nie, Y.; Muller, D. A.; Kourkoutis, L. F.; Schlom, D. G. Improved control of atomic layering in perovskite-related homologous series. *APL Mater.* **2021**, *9*, 021118.
- (8) Mühlhain, L.; Singh, C. B.; Lotnyk, A.; Himcinschi, C.; Yun, Y.; Ramakrishnegowda, N.; Knoche, D. S.; Li, X.; Bhatnagar, A. Nanocomposites with Three-Dimensional Architecture and Impact on Photovoltaic Effect. *Nano Lett.* **2020**, *20*, 8789–8795.
- (9) Momma, K.; Izumi, F. VESTA 3 for three-dimensional visualization of crystal, volumetric and morphology data. *J. Appl. Crystallogr.* **2011**, *44*, 1272–1276.
- (10) Zhao, H.; Kimura, H.; Cheng, Z.; Osada, M.; Wang, J.; Wang, X.; Dou, S.; Liu, Y.; Yu, J.; Matsumoto, T.; Tohei, T.; Shibata, N.; Ikuhara, Y. Large magnetoelectric coupling in magnetically short-range ordered $\text{Bi}_5\text{Ti}_3\text{FeO}_{15}$ film. *Sci. Rep.* **2014**, *4*, 5255.
- (11) Keeney, L.; Downing, C.; Schmidt, M.; Pemble, M. E.; Nicolosi, V.; Whatmore, R. W. Direct atomic scale determination of magnetic ion partition in a room temperature multiferroic material. *Sci. Rep.* **2017**, *7*, 1737.
- (12) Napari, M.; Huq, T. N.; Hoye, R. L. Z.; MacManus-Driscoll, J. L. Nickel oxide thin films grown by chemical deposition techniques: Potential and challenges in next-generation rigid and flexible device applications. *InfoMat* **2021**, *3*, 536–576.
- (13) Bi, H.; Li, S.; Zhang, Y.; Du, Y. Ferromagnetic-like behavior of ultrafine NiO nanocrystallites. *J. Magn. Magn. Mater.* **2004**, *277*, 363–367.
- (14) Madhu, G.; Maniammal, K.; Biju, V. Defect induced ferromagnetic interaction in nanostructured nickel oxide with core-shell magnetic structure: the role of Ni^{2+} and O^{2-} vacancies. *Phys. Chem. Chem. Phys.* **2016**, *18*, 12135–12148.
- (15) Sugiyama, I.; Shibata, N.; Wang, Z.; Kobayashi, S.; Yamamoto, T.; Ikuhara, Y. Ferromagnetic dislocations in antiferromagnetic NiO. *Nat. Nanotechnol.* **2013**, *8*, 266–270.
- (16) Rutherford, B. X.; Zhang, B.; Wang, X.; Sun, X.; Qi, Z.; Wang, H.; Wang, H. Strain Effects on the Growth of $\text{La}_{0.7}\text{Sr}_{0.3}\text{MnO}_3$ (LSMO)-NiO Nanocomposite Thin Films via Substrate Control. *ACS Omega* **2020**, *5*, 23793–23798.
- (17) Isupov, V. A. Systematization of Aurivillius-type layered oxides. *Inorg. Mater.* **2006**, *42*, 1094–1098.
- (18) Wang, F.; Young, S. M.; Zheng, F.; Grinberg, I.; Rappe, A. M. Substantial bulk photovoltaic effect enhancement via nanolayering. *Nat. Commun.* **2016**, *7*, 10419.
- (19) Gradauskaite, E.; Gray, N.; Campanini, M.; Rossell, M. D.; Trassin, M. Nanoscale Design of High-Quality Epitaxial Aurivillius Thin Films. *Chem. Mater.* **2021**, *33*, 9439–9446.
- (20) Zheng, H.; Straub, F.; Zhan, Q.; Yang, P.-L.; Hsieh, W.-K.; Zavaliche, F.; Chu, Y.-H.; Dahmen, U.; Ramesh, R. Self-Assembled Growth of BiFeO_3 - CoFe_2O_4 Nanostructures. *Adv. Mater.* **2006**, *18*, 2747–2752.
- (21) Takahashi, R.; Valset, K.; Folven, E.; Eberg, E.; Grepstad, J. K.; Tybell, T. Long-range spontaneous structural ordering in barium stannate thin films. *Appl. Phys. Lett.* **2010**, *97*, 081906.
- (22) Morandi, C.; Gray, J. L.; Auken, W.; Trolier-McKinstry, S. Pulsed-Laser Deposited 35 $\text{Bi}(\text{Mg}_{1/2}\text{Ti}_{1/2})\text{O}_3$ -65 PbTiO_3 Thin Films-Part I: Influence of Processing on Composition, Microstructure, and Ferroelectric Hysteresis. *IEEE Trans. Ultrason. Ferroelectrics Freq. Control* **2018**, *65*, 1525–1533.
- (23) Lunkenheimer, P.; Loidl, A.; Ottermann, C. R.; Bange, K. Correlated barrier hopping in NiO films. *Phys. Rev. B: Condens. Matter Phys.* **1991**, *44*, 5927–5930.
- (24) Bennett, J. W.; Grinberg, I.; Rappe, A. M. New Highly Polar Semiconductor Ferroelectrics through d8 Cation-O Vacancy Substitution into PbTiO_3 : A Theoretical Study. *J. Am. Chem. Soc.* **2008**, *130*, 17409–17412.
- (25) Yun, Y.; Ramakrishnegowda, N.; Park, D.-S.; Bhatnagar, A. Long range ordering of 71° domain walls in epitaxial BiFeO_3 thin films. *Appl. Phys. Lett.* **2018**, *113*, 042901.
- (26) Ma, C. S.; Hau, S. K.; Wong, K. H.; Chan, P. W.; Choy, C. L. The role of ambient gas scattering effect and lead oxide formation in pulsed laser deposition of lead-zirconate-titanate thin films. *Appl. Phys. Lett.* **1996**, *69*, 2030–2032.
- (27) Himcinschi, C.; Vrejoiu, I.; Friedrich, M.; Ding, L.; Cobet, C.; Esser, N.; Alexe, M.; Zahn, D. R. T. Optical characterisation of BiFeO_3 epitaxial thin films grown by pulsed-laser deposition. *Phys. Status Solidi C* **2010**, *7*, 296–299.
- (28) Bruggeman, D. A. G. Berechnung verschiedener physikalischer Konstanten von heterogenen Substanzen. I. Dielektrizitätskonstanten und Leitfähigkeiten der Mischkörper aus isotropen Substanzen. *Ann. Phys.* **1935**, *416*, 636–664.

Supporting Information: Control of layering in Aurivillius phase nanocomposite thin films and influence on ferromagnetism and optical absorption

Lutz Mühlenbein,^{†,‡} Chandra Bhal Singh,[¶] Akhilesh Kumar Singh,[¶] Ignasi Fina,[§]
Cameliu Himcinschi,^{||} Andriy Lotnyk,^{⊥,#} and Akash Bhatnagar^{*,†,‡}

[†]*Zentrum für Innovationskompetenz SiLi-nano, Martin Luther Universität
Halle-Wittenberg, Halle (Saale), Germany*

[‡]*Institute of Physics, Martin Luther Universität Halle-Wittenberg, Halle (Saale), Germany*

[¶]*School of Materials Science and Technology, Indian Institute of Technology (Banaras
Hindu University), Varanasi 221005, India*

[§]*Institut de Ciència de Materials de Barcelona-CSIC, Campus de la UAB, 08193,
Bellaterra, Barcelona, Spain*

^{||}*Institute of Theoretical Physics, TU Bergakademie Freiberg, Freiberg, Germany*

[⊥]*Leibniz Institute of Surface Engineering, Leipzig, Germany*

[#]*Laboratory of Infrared Materials and Devices, The Research Institute of Advanced
Technologies, Ningbo University, Ningbo, China*

E-mail: akash.bhatnagar@physik.uni-halle.de

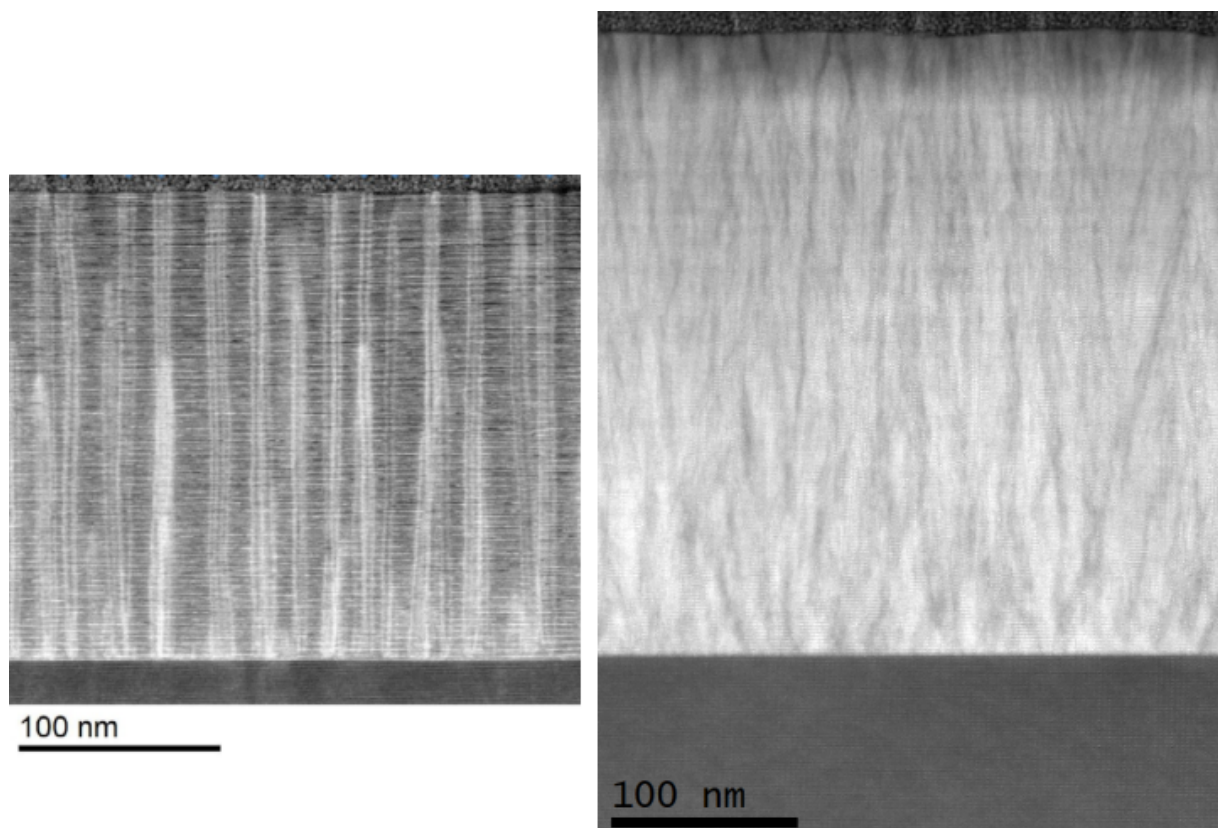


Figure S1: Cross-sectional TEM-HAADF images of 220nm thick layered PTBNNO film ($m \approx 4$) exhibiting ordered vertically aligned NiO nanocolumns (left) versus 320nm thick “non-layered” PTBNNO film not exhibiting vertically aligned nanocolumns (right).

Chapter 6

Summary and Outlook

The present work was dedicated to exploring the interplay between structure and photoelectronic effects in self-assembled vertically aligned nanocomposite oxide thin films. Special attention was paid to photoconduction and the bulk photovoltaic effect. Two nanocomposite systems were studied: The considerably well-known $\text{BiFeO}_3\text{:Sm}_2\text{O}_3$ system and the hitherto unknown $(\text{Pb, Bi})(\text{Ti, Nb})\text{O}_3\text{:NiO}$ system.

In the case of the $\text{BiFeO}_3\text{:Sm}_2\text{O}_3$ VAN, the result of this thesis led to a reconsideration of the previously reported results on the growth and functionalities of this nanocomposite system. The ability of BFO to accommodate Sm on the A-site has considerable effect on the formation of a phase-separated nanocomposite. The orthorhombic symmetry of low-concentration doping that was previously reported up to 20% appears to persist up to 50% doping concentration. Instead of an element-phase-separated nanocomposite, a structural nanocomposite is formed, consisting of clusters with either one of the two possible orientations of the orthorhombic unit cell. It was further shown that both structural and functional properties, specifically the out-of-plane lattice parameter and the electrical response, which had been previously attributed to the nanocomposite nature of the BFO:SmO system, are reproduced by the present nanocomposite without the formation of elementally segregated nanocolumns. While the actual presence of phase separation in the BFO-SmO system is evident in previous reports, the results of this thesis serve as motivation to revisit previous growth parameters to determine what drives phase separation in a system with high intermiscibility of the constituents. A similar situation was recently reported in the phase-separated $\text{BaTiO}_3\text{-SrRuO}_3$ system, where both phases generally assume the same unit cell geometry and are known to intermix as $(\text{Ba, Sr})\text{TiO}_3$ or SrTiO_3 [35]. The understanding of what drives phase separation in oxide systems with high intermiscibility has so far been poor and deserves attention in future work in this field. Although spinodal decomposition has been proposed for such a scenario, it has not been studied in detail, and process parameters on how to induce and control the decomposition process have not been reported.

The $(\text{Pb, Bi})(\text{Ti, Nb})\text{O}_3:\text{NiO}$ nanocomposite thin film system was first discovered in the preparation of this thesis. It is a rare case of self-assembled 3D or "scaffold" nanocomposite, with thin NiO columns that extend normal to the substrate surface and embedded in an Aurivillius phase, a layered perovskite structure, in which perovskite blocks are intermitted with fluorite-like Bi_2O_2 layers. The structure is synthesized via PLD with simple continuous ablation from a single phase perovskite ceramic target onto single crystal SrTiO_3 or LaAlO_3 substrates, rendering both horizontal and vertical phase separation and ordering to be self-assembled. It was demonstrated that the PLD process parameters provide easy tunability with coarse and fine control over the structural properties of the nanocomposite. Non-stoichiometric transfer was identified as the underlying reason for the formation of the nanocomposite. The nanocomposite structure exhibited photoconductive hot spots at the column or column-matrix interface, boosting the photovoltaic efficiency by a factor of five compared to a reference PbTiO_3 thin film. Furthermore, ferromagnetism was detected in the 3D nanocomposite structure. A strong signal was detected in the densely layered structure, and weak to no signal was detected in samples close to the perovskite archetype.

Both materials systems reveal interesting photoconductive properties because of the special structure of the nanocomposite character. Especially the self-assembled 3D nanocomposite $(\text{Pb, Bi})(\text{Ti, Nb})\text{O}_3:\text{NiO}$ is intriguing and deserves future attention. First, transfer of the charge-separation concept proven here to other VAN systems may be considered worthwhile, and future work may focus on further pushing the limits of enhancement of photovoltaic efficiency due to the demonstrated device architecture. Second, a possible multiferroic application can be envisioned. Aurivillius phases are robust ferroelectrics - in combination with the ferromagnetism demonstrated here and presumed to originate at the matrix-column interfaces, the feasibility of magnetoelectric coupling via magnetostriction is plausible. Thus, a unique combination of in-plane ferroelectricity with out-of-plane ferromagnetism might be realized. Therefore, investigation of magnetoelectric coupling can be envisioned as a separate focus of future work on this VAN thin film system.

Bibliography

- [1] D. R. Askeland and W. J. Wright. Science and engineering of materials. *Cengage Learning*, 7th edition, 2015.
- [2] R. E. Newnham, D. P. Skinner, and L. E. Cross. Connectivity and piezoelectric-pyroelectric composites. *Materials Research Bulletin*, 13(5):525–536, 1978.
- [3] N. A. Hill. Why are there so few magnetic ferroelectrics? *Journal of Physical Chemistry B*, 2000.
- [4] H. Zheng, J. Wang, L. Mohaddes-Ardabili, M. Wuttig, L. Salamanca-Riba, D. G. Schlom, and R. Ramesh. Three-dimensional heteroepitaxy in self-assembled BaTiO₃-CoFe₂O₄ nanostructures. *Applied Physics Letters*, 85(11):2035–2037, 2004.
- [5] S. Lee, A. Sangle, P. Lu, A. Chen, W. Zhang, J. S. Lee, H. Wang, Q. Jia, and J. L. Macmanus-Driscoll. Novel electroforming-free nanoscaffold memristor with very high uniformity, tunability, and density. *Advanced Materials*, 26(36):6284–6289, 2014.
- [6] D. M. Cunha, C. M. Vos, T. A. Hendriks, D. P. Singh, and M. Huijben. Morphology evolution during lithium-based vertically aligned nanocomposite growth. *ACS Applied Materials & Interfaces*, 11(47):44444–44450, 2019.
- [7] A. J. Lovett, A. Kursumovic, S. Dutton, Z. Qi, Z. He, H. Wang, and J. L. MacManus-Driscoll. Lithium-based vertically aligned nanocomposite films incorporating Li_xLa_{0.32}(Nb_{0.7}Ti_{0.32})O₃ electrolyte with high Li₊ ion conductivity. *APL Materials*, 10:051102, 2022.
- [8] S. Lee and J. L. Macmanus-Driscoll. Research update: Fast and tunable nanoionics in vertically aligned nanostructured films. *APL Materials*, 5(4):042304, 2017.
- [9] A. J. Lovett, M. P. Wells, Z. He, J. Lu, H. Wang, and J. L. MacManus-Driscoll. High ionic conductivity in fluorite δ -bismuth oxide-based vertically aligned nanocomposite thin films. *Journal of Materials Chemistry A*, 10:3478–3484, 2022.
- [10] L. T. Quynh, C. N. Van, Y. Bitla, J.-W. Chen, T. H. Do, W.-Y. Tzeng, S.-C. Liao, K.-A. Tsai, Y.-C. Chen, C.-L. Wu, and et al. Self-assembled BiFeO₃- ϵ Fe₂O₃ vertical heteroepitaxy for visible light photoelectrochemistry. *Advanced Energy Materials*, 6(18):1600686, 2016.
- [11] T. H. Do, C. Nguyen Van, K. A. Tsai, L. T. Quynh, J. W. Chen, Y. C. Lin, Y. C. Chen, W. C. Chou, C. L. Wu, Y. J. Hsu, and Y. H. Chu. Superior photoelectrochemical activity of self-assembled NiWO₄-WO₃ heteroepitaxy. *Nano Energy*, 23:153–160, 2016.

- [12] M. J. Chen, X. K. Ning, S. F. Wang, and G. S. Fu. Significant enhancement of energy storage density and polarization in self-assembled PbZrO₃:NiO nano-columnar composite films. *Nanoscale*, 11(4):1914–1920, 2019.
- [13] O. I. Lebedev, J. Verbeeck, G. Van Tendeloo, O. Shapoval, A. Belenchuk, V. Moshnyaga, B. Damaschke, and K. Samwer. Structural phase transitions and stress accommodation in (La_{0.67}Ca_{0.33}MnO₃)_{1-x}:(MgO)_x composite films. *Physical Review B*, 66(10):104421, 2002.
- [14] V. Moshnyaga, B. Damaschke, O. Shapoval, A. Belenchuk, J. Faupel, O. I. Lebedev, J. Verbeeck, G. Van Tendeloo, M. Mücksch, V. Tsurkan, R. Tidecks, and K. Samwer. Structural phase transition at the percolation threshold in epitaxial (La_{0.7}Ca_{0.3}MnO₃)_{1-x}:(MgO)_x nanocomposite films. *Nature Materials*, 2(4):247–252, 2003.
- [15] H. Zheng, J. Wang, S.E. Lofland, Z. Ma, L. Mohaddes-Ardabili, T. Zhao, L. Salamanca-Riba, S.R. Shinde, S. B. Ogale, F. Bai, D. Viehland, Y. Jia, D. G. Schlom, M. Wuttig, A. Roytburd, and R. Ramesh. Multiferroic BaTiO₃-CoFe₂O₄ Nanostructures. *Science*, 303:661–663, 2004.
- [16] J. Li, I. Levin, J. Slutsker, V. Provenzano, P. K. Schenck, R. Ramesh, J. Ouyang, and A. L. Roytburd. Self-assembled multiferroic nanostructures in the CoFe₂O₄-PbTiO₃ system. *Applied Physics Letters*, 87(7):85–88, 2005.
- [17] I. Levin, J. Li, J. Slutsker, and A. L. Roytburd. Design of self-assembled multiferroic nanostructures in epitaxial films. *Advanced Materials*, 18(15):2044–2047, 2006.
- [18] F. Zavaliche, H. Zheng, L. Mohaddes-Ardabili, S. Y. Yang, Q. Zhan, P. Shafer, E. Reilly, R. Chopdekar, Y. Jia, P. Wright, D. G. Schlom, Y. Suzuki, and R. Ramesh. Electric field-induced magnetization switching in epitaxial columnar nanostructures. *Nano Letters*, 5(9):1793–1796, 2005.
- [19] H. Zheng, F. Straub, Q. Zhan, P.-L. Yang, W.-K. Hsieh, F. Zavaliche, Y.-H. Chu, U. Dahmen, and R. Ramesh. Self-assembled growth of BiFeO₃-CoFe₂O₄ Nanostructures. *Advanced Materials*, 18(20):2747–2752, 2006.
- [20] Q. Zhan, R. Yu, S. P. Crane, H. Zheng, C. Kisielowski, and R. Ramesh. Structure and interface chemistry of perovskite-spinel nanocomposite thin films. *Applied Physics Letters*, 89(17):1–4, 2006.
- [21] J. L. MacManus-Driscoll, P. Zerrer, H. Wang, H. Yang, J. Yoon, A. Fouchet, R. Yu, M. G. Blamire, and Q. Jia. Strain control and spontaneous phase ordering in vertical nanocomposite heteroepitaxial thin films. *Nature Materials*, 7(4):314–320, 2008.
- [22] S. A. Harrington, J. Zhai, S. Denev, V. Gopalan, H. Wang, Z. Bi, S. A.T. Redfern, S. H. Baek, C. W. Bark, C. B. Eom, Q. Jia, M. E. Vickers, and J. L. MacManus-Driscoll. Thick lead-free ferroelectric films with high Curie temperatures through nanocomposite-induced strain. *Nature Nanotechnology*, 6(8):491–495, 2011.
- [23] Z. Bi, E. Weal, H. Luo, A. Chen, J. L. MacManus-Driscoll, Q. Jia, and H. Wang. Microstructural and magnetic properties of (La_{0.7}Sr_{0.3}MnO₃)_{0.7}:(Mn₃O₄)_{0.3} nanocomposite thin films. *Journal of Applied Physics*, 109(5):1–7, 2011.
- [24] A. Chen, Z. Bi, H. Hazariwala, X. Zhang, Q. Su, L. Chen, Q. Jia, J. L. MacManus-Driscoll, and H. Wang. Microstructure, magnetic, and low-field magnetotransport properties of self-assembled (La_{0.7}Sr_{0.3}MnO₃)_{0.5}:(CeO₂)_{0.5} vertically aligned nanocomposite thin films. *Nanotechnology*, 22(31):1–8, 2011.

- [25] A. Chen, J. M. Hu, P. Lu, T. Yang, W. Zhang, L. Li, T. Ahmed, E. Enriquez, M. Weigand, Q. Su, H. Wang, J. X. Zhu, J. L. MacManus-Driscoll, L.-Q. Chen, D. Yarotski, and Q. Jia. Role of scaffold network in controlling strain and functionalities of nanocomposite films. *Science Advances*, 2(6):1–10, 2016.
- [26] J. Huang, A. Gellatly, A. Kauffmann, X. Sun, and H. Wang. Exchange bias effect along vertical interfaces in $\text{La}_{0.7}\text{Sr}_{0.3}\text{MnO}_3\text{:NiO}$ vertically aligned nanocomposite thin films integrated on silicon substrates. *Crystal Growth and Design*, 18(8):4388–4394, 2018.
- [27] B. X. Rutherford, B. Zhang, X. Wang, X. Sun, Z. Qi, H. Wang, and H. Wang. Strain effects on the growth of $\text{La}_{0.7}\text{Sr}_{0.3}\text{MnO}_3(\text{lsmo})\text{-NiO}$ nanocomposite thin films via substrate control. *ACS Omega*, 5(37):23793–23798, 2020.
- [28] M. Fan, H. Wang, S. Misra, B. Zhang, Z. Qi, X. Sun, J. Huang, and H. Wang. Microstructure, magnetic, and magnetoresistance properties of $(\text{La}_{0.7}\text{Sr}_{0.3}\text{MnO}_3)\text{:CuO}$ nanocomposite thin films. *ACS Applied Materials and Interfaces*, 10(6):5779–5784, 2018.
- [29] X. Gao, Leigang Li, J. Jian, H. Wang, M. Fan, J. Huang, X. Wang, and H. Wang. Vertically aligned nanocomposite $\text{BaTiO}_3\text{:YMnO}_3$ thin films with room temperature multiferroic properties toward nanoscale memory devices. *ACS Applied Nano Materials*, 1(6):2509–2514, 2018.
- [30] T. Fix, E. M. Choi, J. W.A. Robinson, S. B. Lee, A. Chen, B. Prasad, H. Wang, M. G. Blamire, and J. L. Macmanus-Driscoll. Electric-field control of ferromagnetism in a nanocomposite via a ZnO phase. *Nano Letters*, 13(12):5886–5890, 2013.
- [31] J. MacManus-Driscoll, A. Suwardi, A. Kursumovic, Z. Bi, C. F. Tsai, H. Wang, Q. Jia, and O. J. Lee. New strain states and radical property tuning of metal oxides using a nanocomposite thin film approach. *APL Materials*, 3(6), 2015.
- [32] W. Zhang, A. Chen, J. Jian, Y. Zhu, L. Chen, P. Lu, Q. Jia, J. L. MacManus-Driscoll, X. Zhang, and H. Wang. Strong perpendicular exchange bias in epitaxial $\text{La}_{0.7}\text{Sr}_{0.3}\text{MnO}_3\text{:BiFeO}_3$ nanocomposite films through vertical interfacial coupling. *Nanoscale*, 7(33):13808–13815, 2015.
- [33] G. Panchal, R. J. Choudhary, M. Kumar, and D. M. Phase. Interfacial spin glass mediated spontaneous exchange bias effect in self-assembled $(\text{La}_{0.7}\text{Sr}_{0.3}\text{MnO}_3)\text{:NiO}$ nanocomposite thin films. *Journal of Alloys and Compounds*, 796:196–202, 2019.
- [34] G. Panchal, A. Panchwane, M. Kumar, K. Fritsch, R. J. Choudhary, and D. M. Phase. Synthesis and characterization of vertically aligned $(\text{La}_{0.7}\text{Sr}_{0.3}\text{MnO}_3)\text{:NiO}$ nanocomposite thin films for spintronic applications. *ACS Applied Nano Materials*, 4(1):102–112, 2021.
- [35] F. Wang, C. Jiang, and J. Huang. Multiferroic thin film via $\text{SrRuO}_3\text{-BaTiO}_3$ vertically aligned nanocomposite design. *Applied Physics Letters*, 117(16), 2020.
- [36] R. Wu and J. L. MacManus-Driscoll. Recent developments and the future perspectives in magnetoelectric nanocomposites for memory applications. *APL Materials*, 10(1):010901, 2022.
- [37] S. Kang, A. Goyal, J. Li, A. A. Gapud, P. M. Martin, L. Heatherly, J. R. Thompson, D. K. Christen, F. A. List, M. Paranthaman, and D. F. Lee. High-performance high-Tc superconducting wires. *Science*, 311(5769):1911–1914, 2006.

- [38] D. M. Cunha and M. Huijben. Lithium-based vertically aligned nanocomposites for three-dimensional solid-state batteries. *MRS Bulletin*, 46(2):152–158, 2021.
- [39] Y. Ha, J. L. MacManus-Driscoll, and S. Lee. Vertically aligned nanocomposite films by self-assembled epitaxial nucleation for super-broadband transparent conductors. *InfoMat*, 5(4), 2022.
- [40] D. G. Schlom, L.-Q. Chen, C.-B. Eom, K. M. Rabe, S. K. Streiffer, and J.-M. Triscone. Strain tuning of ferroelectric thin films. *Annual Review of Materials Research*, 37(1):589–626, 2007.
- [41] T. Takenaka and H. Nagata. Current status and prospects of lead-free piezoelectric ceramics. *Journal of the European Ceramic Society*, 25(12):2693–2700, 2005.
- [42] K. J. Choi, M. Biegalski, Y. L. Li, A. Sharan, J. Schubert, R. Uecker, P. Reiche, Y. B. Chen, X. Q. Pan, V. Gopalan, L. Q. Che, D. C. Schlom, and C. B. Eom. Enhancement of ferroelectricity in strained BaTiO₃ thin films. *Science*, 306(5698):1005–1009, 2004.
- [43] J.W. Matthews and A.E. Blakeslee. Defects in epitaxial multilayers. *Journal of Crystal Growth*, 27:118–125, 1974.
- [44] Z. Bi, J. H. Lee, H. Yang, Q. Jia, J. L. MacManus-Driscoll, and H. Wang. Tunable lattice strain in vertically aligned nanocomposite (BiFeO₃)_x:(Sm₂O₃)_{1-x} thin films. *Journal of Applied Physics*, 106(9), 2009.
- [45] J. Huang, W. Li, H. Yang, and J. L. MacManus-Driscoll. Tailoring physical functionalities of complex oxides by vertically aligned nanocomposite thin-film design. *MRS Bulletin*, 46(2):159–167, 2021.
- [46] A Ohtomo and H Y Hwang. A high-mobility electron gas at the LaAlO₃-SrTiO₃ heterointerface. *Nature*, 427:423–427, 2004.
- [47] H. Y. Hwang, Y. Iwasa, M. Kawasaki, B. Keimer, N. Nagaosa, and Y. Tokura. Emergent phenomena at oxide interfaces. *Nature Materials*, 11(2):103–113, 2012.
- [48] Z. Huang, A., X. Renshaw Wang, A. Rusydi, J. Chen, H. Yang, and T. Venkatesan. Interface engineering and emergent phenomena in oxide heterostructures. *Advanced Materials*, 30(47), 2018.
- [49] A. Brinkman, M. Huijben, M. van Zalk, J. Huijben, U. Zeitler, J. C. Maan, W. G. van der Wiel, G. Rijnders, D. H. A. Blank, and H. Hilgenkamp. Magnetic effects at the interface between non-magnetic oxides. *Nature Materials*, 6(7):493–496, 2007.
- [50] J. A. Bert, B. Kalisky, C. Bell, M. Kim, Y. Hikita, H. Y. Hwang, and K. A. Moler. Direct imaging of the coexistence of ferromagnetism and superconductivity at the LaAlO₃/SrTiO₃ interface. *Nature Physics*, 7(10):767–771, 2011.
- [51] S. Stemmer and S. James Allen. Two-dimensional electron gases at complex oxide interfaces. *Annual Review of Materials Research*, 44:151–171, 2014.
- [52] A. M. Kaiser, A. X. Gray, G. Conti, J. Son, A. Greer, A. Perona, A. Rattanachata, A. Y. Saw, A. Bostwick, S. Yang, S. H. Yang, E. M. Gullikson, J. B. Kortright, S. Stemmer, and C. S. Fadley. Suppression of near-Fermi level electronic states at the interface in a LaNiO₃/SrTiO₃ superlattice. *Physical Review Letters*, 107(11):1–4, 2011.

- [53] A. J. Grutter, H. Yang, B. J. Kirby, M. R. Fitzsimmons, J. A. Aguiar, N. D. Browning, C. A. Jenkins, E. Arenholz, V. V. Mehta, U. S. Alaan, and Y. Suzuki. Interfacial ferromagnetism in $\text{LaNiO}_3/\text{CaMnO}_3$ superlattices. *Physical Review Letters*, 111(8):1–5, 2013.
- [54] R. B. Comes, S. R. Spurgeon, S. M. Heald, D. M. Kepaptsoglou, L. Jones, P. V. Ong, M. E. Bowden, Q. M. Ramasse, P. V. Sushko, and S. A. Chambers. Interface-induced polarization in $\text{SrTiO}_3\text{-LaCrO}_3$ superlattices. *Advanced Materials Interfaces*, 3(10):1–8, 2016.
- [55] H. Kroemer. Quasi-electric fields and band offsets: Teaching electrons new tricks. *International Journal of Modern Physics B*, 16(5):677–697, 2002.
- [56] N. M. Aimon, D. H. Kim, X. Sun, and C. A. Ross. Multiferroic behavior of templated $\text{BiFeO}_3\text{-CoFe}_2\text{O}_4$ self-assembled nanocomposites. *ACS Applied Materials and Interfaces*, 7(4):2263–2268, 2015.
- [57] M. Gao, Y. Yang, W. F. Rao, and D. Viehland. Magnetoelectricity in vertically aligned nanocomposites: Past, present, and future. *MRS Bulletin*, 46(2):123–130, 2021.
- [58] Y. H. Hsieh, E. Strelcov, J.-M. Liou, C.-Y. Shen, Y.-C. Chen, S. V. Kalinin, and Y.-H. Chu. Electrical modulation of the local conduction at oxide tubular interfaces. *ACS Nano*, 7(10):8627–8633, 2013.
- [59] Y. H. Hsieh, J. M. Liou, B. C. Huang, C. W. Liang, Q. He, Q. Zhan, Y. P. Chiu, Y. C. Chen, and Y. H. Chu. Local conduction at the $\text{BiFeO}_3\text{-CoFe}_2\text{O}_4$ tubular oxide interface. *Advanced Materials*, 24(33):4564–4568, 2012.
- [60] E. Strelcov, A. Belianinov, Y. H. Hsieh, S. Jesse, A. P. Baddorf, Y. H. Chu, and S. V. Kalinin. Deep data analysis of conductive phenomena on complex oxide interfaces: Physics from data mining. *ACS Nano*, 8(6):6449–6457, 2014.
- [61] C. Dharanya and G. Dharmalingam. Oxygen vacancies in nanostructured hetero-interfacial oxides: a review. *Springer Netherlands*, 2022.
- [62] W. Li, R. Zhao, R. Tang, A. Chen, W. Zhang, X. Lu, H. Wang, and H. Yang. Vertical-interface-manipulated conduction behavior in nanocomposite oxide thin films. *ACS Applied Materials and Interfaces*, 6(8):5356–5361, 2014.
- [63] W. Li, W. Zhang, L. Wang, J. Gu, A. Chen, R. Zhao, Y. Liang, H. Guo, R. Tang, C. Wang, K. Jin, and H. Wang, H. and Yang. Vertical interface induced dielectric relaxation in nanocomposite $(\text{BaTiO}_3)_{1-x}:(\text{Sm}_2\text{O}_3)_x$ thin films. *Scientific Reports*, 5:1–8, 2015.
- [64] X. Sun, Q. Li, J. Huang, J. Jian, P. Lu, X. Zhang, J. L. Macmanus-Driscoll, and H. Wang. Strain and property tuning of the 3D framed epitaxial nanocomposite thin films via interlayer thickness variation. *Journal of Applied Physics*, 125(8), 2019.
- [65] A. Chen and Q. Jia. A pathway to desired functionalities in vertically aligned nanocomposites and related architectures. *MRS Bulletin*, 46(2):115–122, 2021.
- [66] A. Artemev, J. Slutsker, and A. L. Roytburd. Phase field modeling of self-assembling nanostructures in constrained films. *Acta Materialia*, 53(12):3425–3432, 2005.

- [67] J. L. Macmanus-Driscoll. Self-assembled heteroepitaxial oxide nanocomposite thin film structures: Designing interface-induced functionality in electronic materials. *Advanced Functional Materials*, 20(13):2035–2045, 2010.
- [68] H. Zheng, Q. Zhan, F. Zavaliche, M. Sherburne, F. Straub, M. P. Cruz, L.-Q. Chen, U. Dahmen, and R. Ramesh. Controlling self-assembled perovskite-spinel nanostructures. *Nano Letters*, 6(7):1401–1407, 2006.
- [69] Y. H. Hsieh, H. H. Kuo, S. C. Liao, H. J. Liu, Y. J. Chen, H. J. Lin, C. T. Chen, C. H. Lai, Q. Zhan, Y. L. Chueh, and Y. H. Chu. Tuning the formation and functionalities of ultrafine CoFe_2O_4 nanocrystals via interfacial coherent strain. *Nanoscale*, 5(14):6219–6223, 2013.
- [70] X. B. Liao, Y. Ni, H. Yang, and L. H. He. Role of modulus mismatch in vertically aligned nanocomposite formation during spinodal decomposition in constrained films. *Applied Physics Letters*, 103(14), 2013.
- [71] H. J. Liu, W. I. Liang, Y. H. Chu, H. Zheng, and R. Ramesh. Self-assembled vertical heteroepitaxial nanostructures: From growth to functionalities. *MRS Communications*, 4(2):31–44, 2014.
- [72] A. Chen, Z. Harrell, P. Lu, E. Enriquez, L. Li, B. Zhang, P. Dowden, C. Chen, H. Wang, J. L. MacManus-Driscoll, and Q. Jia. Strain enhanced functionality in a bottom-up approach enabled 3D super-nanocomposites. *Advanced Functional Materials*, 29(26), 2019.
- [73] L. Mühlenbein, C. B. Singh, A. Lotnyk, C. Himcinschi, Y. Yun, N. Ramakrishnegowda, D. S. Knoche, X. Li, and A. Bhatnagar. Nanocomposites with three-dimensional architecture and impact on photovoltaic effect. *Nano Letters*, 2020.
- [74] L. Mühlenbein, C. B. Singh, A. K. Singh, I. Fina, C. Himcinschi, A. Lotnyk, and A. Bhatnagar. Control of layering in aurivillius phase nanocomposite thin films and influence on ferromagnetism and optical absorption. *ACS Applied Electronic Materials*, 2022.
- [75] T. C. Kim, S. Ojha, G. Tian, S. H. Lee, H. K. Jung, J. W. Choi, L. Kornblum, F. J. Walker, C. H. Ahn, C. A. Ross, and D. H. Kim. Self-assembled multiferroic epitaxial BiFeO_3 - CoFe_2O_4 nanocomposite thin films grown by RF magnetron sputtering. *Journal of Materials Chemistry C*, 6(20):5552–5561, 2018.
- [76] D. Zhang, M. Kalaswad, and H. Wang. Self-assembled vertically aligned nanocomposite systems integrated on silicon substrate: Progress and future perspectives. *Journal of Vacuum Science & Technology A*, 40(1):010802, 2022.
- [77] S. Misra and H. Wang. Review on the growth, properties and applications of self-assembled oxide-metal vertically aligned nanocomposite thin films-current and future perspectives. *Materials Horizons*, 8(3):869–884, 2021.
- [78] S. Pal, N. V. Sarath, K. S. Priya, and P. Murugavel. A review on ferroelectric systems for next generation photovoltaic applications. *Journal of Physics D: Applied Physics*, 55(28):283001, 2022.
- [79] V. M. Fridkin and B. N. Popov. Anomalous photovoltaic effect in ferroelectrics. *Uspekhi Fizicheskikh Nauk*, 21(12):981–991, 1978.
- [80] V. M. Fridkin. Photoferroelectrics. *Springer Science & Business Media*, 1978.

- [81] W. Ji, K. Yao, and Y. C. Liang. Bulk photovoltaic effect at visible wavelength in epitaxial ferroelectric BiFeO₃ thin films. *Advanced Materials*, 22(15):1763–1766, 2010.
- [82] T. Choi, S. Lee, Y. J. Choi, V. Kiryukhin, and S. W. Cheong. Switchable ferroelectric diode and photovoltaic effect in BiFeO₃. *Science*, 324(5923):63–66, 2009.
- [83] S. Y. Yang, J. Seidel, S. J. Byrnes, P. Shafer, C. H. Yang, M. D. Rossell, P. Yu, Y. H. Chu, J. F. Scott, J. W. Ager, L. W. Martin, and R. Ramesh. Above-bandgap voltages from ferroelectric photovoltaic devices. *Nature Nanotechnology*, 5(2):143–147, 2010.
- [84] H. T. Yi, T. Choi, S. G. Choi, Y. S. Oh, and S. W. Cheong. Mechanism of the switchable photovoltaic effect in ferroelectric BiFeO₃. *Advanced Materials*, 23(30):3403–3407, 2011.
- [85] A. Bhatnagar, A. Roy Chaudhuri, Y. Heon Kim, D. Hesse, and M. Alexe. Role of domain walls in the abnormal photovoltaic effect in BiFeO₃. *Nature Communications*, 4, 2013.
- [86] D. S. Knoche, M. Steimecke, Y. Yun, L. Mühlenbein, and A. Bhatnagar. Anomalous circular bulk photovoltaic effect in BiFeO₃ thin films with stripe-domain pattern. *Nature Communications*, 12(1):1–8, 2021.
- [87] R. Guo, L. You, Y. Zhou, Z. Shih Lim, X. Zou, L. Chen, R. Ramesh, and J. Wang. Non-volatile memory based on the ferroelectric photovoltaic effect. *Nature Communications*, 4(1):1990, 2013.
- [88] X. Han, Y. Ji, and Y. Yang. Ferroelectric photovoltaic materials and devices. *Advanced Functional Materials*, 32(14), 2022.
- [89] I. Grinberg, D. V. West, M. Torres, G. Gou, D. M. Stein, L. Wu, G. Chen, E. M. Gallo, A. R. Akbashev, P. K. Davies, J. E. Spanier, and A. M. Rappe. Perovskite oxides for visible-light-absorbing ferroelectric and photovoltaic materials. *Nature*, 503(7477):509–512, 2013.
- [90] R. Nechache, C. Harnagea, S. Li, L. Cardenas, W. Huang, J. Chakrabartty, and F. Rosei. Bandgap tuning of multiferroic oxide solar cells. *Nature Photonics*, 9(1):61–67, 2014.
- [91] S. Cho, J. W. Jang, L. Li, J. Jian, H. Wang, and J. L. Macmanus-Driscoll. Self-assembled heteroepitaxial oxide nanocomposite for photoelectrochemical solar water oxidation. *Chemistry of Materials*, 28(9):3017–3023, 2016.
- [92] F. Wang, S. M. Young, F. Zheng, I. Grinberg, and A. M. Rappe. Substantial bulk photovoltaic effect enhancement via nanolayering. *Nature Communications*, 7:1–7, 2016.
- [93] M. Kawasaki, T. Maeda, R. Tsuchiya, and H. Koinuma. Atomic control of the SrTiO₃ crystal surface. *Science*, 266(5190):1540–1542, 1994.
- [94] G. Koster, B. L. Kropman, G. J. H. M. Rijnders, D. H. A. Blank, and H. Rogalla. Quasi-ideal strontium titanate crystal surfaces through formation of strontium hydroxide. *Applied Physics Letters*, 73(20):2920–2922, 1998.

- [95] A. M. Miller, M. Lemon, M. A. Choffel, S. R. Rich, F. Harvel, and D. C. Johnson. Extracting information from X-ray diffraction patterns containing Laue oscillations. *Zeitschrift für Naturforschung B*, 77(4-5):313–322, 2022.
- [96] H. Kim, J. S. Horwitz, A. Piqué, C. M. Gilmore, and D. B. Chrisey. Electrical and optical properties of indium tin oxide thin films grown by pulsed laser deposition. *Applied Physics A: Materials Science and Processing*, 69(7):447–450, 1999.
- [97] H. Kim, C. M. Gilmore, A. Piqué, J. S. Horwitz, H. Mattoussi, H. Murata, Z. H. Kafafi, and D. B. Chrisey. Electrical, optical, and structural properties of indium-tin-oxide thin films for organic light-emitting devices. *Journal of Applied Physics*, 86(11):6451–6461, 1999.
- [98] H. Yang, H. Wang, G. F. Zou, M. Jain, N. A. Suvorova, D. M. Feldmann, P. C. Dowden, R. F. DePaula, J. L. MacManus-Driscoll, A. J. Taylor, and Q. X. Jia. Leakage mechanisms of self-assembled $(\text{BiFeO}_3)_{0.5}:(\text{Sm}_2\text{O}_3)_{0.5}$ nanocomposite films. *Applied Physics Letters*, 93(14):2006–2009, 2008.
- [99] C. J. Cheng, D. Kan, V. Anbusathaiah, I. Takeuchi, and V. Nagarajan. Microstructure-electromechanical property correlations in rare-earth-substituted BiFeO_3 epitaxial thin films at morphotropic phase boundaries. *Applied Physics Letters*, 97(21):10–13, 2010.
- [100] D. Kan, C. J. Cheng, V. Nagarajan, and I. Takeuchi. Composition and temperature-induced structural evolution in La, Sm, and Dy substituted BiFeO_3 epitaxial thin films at morphotropic phase boundaries. *Journal of Applied Physics*, 110(1), 2011.

Acknowledgements

First and foremost, I would like to extend my sincere thanks to Prof. Dr. Jörg Schilling for his guidance in scientific and administrative matters, as well as for brilliantly performing his role as director to the ZIK SiLi-nano, which was a pleasant workplace at all times and an outstanding place to conduct science.

I would further like to express my deepest appreciation to Dr. Akash Bhatnagar who expertly led the Light-for-High-Voltage-Photovoltaics group and provided day-to-day academic guidance with passion, efficiency, and empathy. I rarely met a better teacher of experimental skill or a sharper mind in discussion.

Special thanks to both the aforementioned for leading the institute and our group through the distressing times of the pandemic with compassion and composure.

I am extremely grateful to fellow PhD students Yeseul Yun, Niranjan Ramakrishnegowda, David S. Walch, and Xinye Li for their guidance, advice, friendship, and solidarity in all matters professional and private. I thank our laboratory assistant Sadé Campbell for reliable operation of the equipment and exemplary scientific diligence. Likewise, I thank Sandra Gesemann for her excellent administrative support, as well as Marian Lisca for the installation and upkeep of our experimental equipment.

I would like to acknowledge the contributions from scientific collaborators Dr. Angelika Hähnel, Dr. Christian Hagendorf, Dr. Cameliu Himcinschi, Dr. Andriy Lotnyk and Dr. Ignasi Fina. Special thanks to Prof. Dr. Kathrin Dörr and Dr. Diana Rata for allowing extensive use of the X-ray diffractometer, which was essential to the study. Similarly, I would be remiss in not mentioning Prof. Dr. Georg Schmidt, Dr. Hartmut Leipner, Dr. Bodo Fuhrmann, Dr. Frank Heyroth, and Sven Schlenker for their salient efforts in maintaining the cleanroom and microfabrication facilities at IZM.

I thank Prof. Lane W. Martin for expressing sincere interest in my work and welcoming me to his and Prof. Ramesh's laboratories at UC Berkeley for six months. I owe them and their students, especially Dr. Abel Fernandez, Dr. Han Gyeol Lee and Dr. Eric Parsonnet, a great deal in advancing the understanding of the $(\text{Pb}, \text{Bi})(\text{Ni}, \text{Nb})\text{O}_3:\text{NiO}$

nanocomposite. The intuitive grasp of intricate concepts they effortlessly combine with unrelenting scientific rigor left me deeply impressed.

And yet, despite the help of all these splendid ladies and gentlemen, I could not have undertaken this journey without the continued support of my family and close friends. It is to them that I owe the success of this endeavour. In particular, I am deeply indebted to my parents for laying the secure foundation for a life in which I was at liberty to choose my path, all the while they never wavered in their trust. Similarly, words cannot express my gratitude to my wife and our daughter. Their unconditional love, support, and understanding will forever be the cornerstone of my achievements.

Curriculum Vitae

<i>PhD</i> in Physics Martin-Luther-Universität Halle-Wittenberg Zentrum für Innovationskompetenz SiLi- nano	May 2018 –
<i>Visiting Research Scholar</i> University of California, Berkeley	November 2021 – May 2022
<i>Master of Science</i> in Renewable Energies Martin-Luther-Universität Halle-Wittenberg	October 2015 – April 2018
<i>Bachelor of Science</i> in Physics Humboldt-Universität zu Berlin	October 2010 – July 2014

List of scientific publications

Mühlenbein, L., Singh, C., Singh, A., Fina, I., Himcinschi, C., Lotnyk, A., & Bhatnagar, A. (2022). Control of Layering in Aurivillius Phase Nanocomposite Thin Films and Influence on Ferromagnetism and Optical Absorption. *ACS Applied Electronic Materials*, 4(4), 1997–2004.

Walch, D., Yun, Y., Ramakrishnegowda, N., Mühlenbein, L., Lotnyk, A., Himcinschi, C., & Bhatnagar, A. (2022). Resistive Switching in Ferroelectric Bi₂FeCrO₆ Thin Films and Impact on the Photovoltaic Effect. *Advanced Electronic Materials*, 8(10), 2200276.

Knoche, D., Steimecke, M., Yun, Y., Mühlenbein, L., & Bhatnagar, A. (2021). Anomalous circular bulk photovoltaic effect in BiFeO₃ thin films with stripe-domain pattern. *Nature Communications*, 12(1), 1–8.

Yun, Y., Mühlenbein, L., Knoche, D., Lotnyk, A., & Bhatnagar, A. (2021). Strongly enhanced and tunable photovoltaic effect in ferroelectric-paraelectric superlattices. *Science Advances*, 7(23), eabe4206.

Mühlenbein, L., Singh, C., Lotnyk, A., Himcinschi, C., Yun, Y., Ramakrishnegowda, N., Knoche, D., Li, X., & Bhatnagar, A. (2020). Nanocomposites with Three-Dimensional Architecture and Impact on Photovoltaic Effect. *Nano Letters*, 20(12), 8789–8795

Ramakrishnegowda, N., Yun, Y., Knoche, D., Mühlenbein, L., Li, X., & Bhatnagar, A. (2020). Activity of Sub-Band Gap States in Ferroelectric Pb (Zr_{0.2}Ti_{0.8}) O₃ Thin Films. *Advanced Electronic Materials*, 1900966.

Mühlenbein, L., Bhal Singh, C., Hähnel, A., Campbell, S., Hagendorf, C., & Bhatnagar, A. (2020). Impact of Samarium on the Growth of Epitaxial Bismuth Ferrite Thin Films. *physica status solidi (b)*.

Ramakrishnegowda, N., Knoche, D., Mühlenbein, L., Lotnyk, A., & Bhatnagar, A. (2020). Bulk-Controlled Photovoltaic Effect in Nanometer-Thick Ferroelectric Pb (Zr_{0.2}Ti_{0.8})O₃ Thin Films and the Role of Domain Walls. *ACS Applied Nano Materials*, 3(12), 11881–11888.

Knoche, D., Yun, Y., Ramakrishnegowda, N., Mühlenbein, L., Li, X., & Bhatnagar, A. (2019). Domain and switching control of the bulk photovoltaic effect in epitaxial BiFeO₃ thin films. *Scientific Reports*, 9(1), 13979.

Piechulla, P., Muehlenbein, L., Wehrspohn, R., Nanz, S., Abass, A., Rockstuhl, C., & Sprafke, A. (2018). Fabrication of Nearly-Hyperuniform Substrates by Tailored Disorder for Photonic Applications. *Advanced Optical Materials*, 6(7), 1701272.

Piechulla, P., Muhlenbein, L., Nanz, S., Abass, A., Sprafke, A., Rockstuhl, C., & Wehrspohn, R. (2017). Tailored Substrate Topographies by Self-Organized Colloidal Particles. In *Optical Nanostructures and Advanced Materials for Photovoltaics* (pp. PM4A–3).

Eidesstattliche Erklärung

Hiermit erkläre ich, Lutz Mühlenbein, dass ich die vorliegende Arbeit mit dem Titel: *Photoelectronic effects in self-assembled vertically aligned nanocomposite oxide thin films* in allen Teilen selbständig verfasst und keine anderen als die angegebenen Quellen und Hilfsmittel benutzt habe. Alle wörtlich oder sinngemäß übernommenen Textstellen habe ich als solche kenntlich gemacht.

Ferner liegen gegen mich weder gerichtliche Vorstrafen vor, noch sind staatsanwaltliche Ermittlungen oder Disziplinarverfahren eingeleitet worden.

Des Weiteren erkläre ich hiermit, dass ich bisher keine andere Arbeit zur Promotion eingereicht noch mit einer anderen Arbeit den Versuch zur Promotion unternommen habe.

Leuven, 17.06.2023
Lutz Mühlenbein